Numerical Modelling, Simulations and Experimental Analysis of Quantum Well, Quantum Dot and Quantum Dash Mode-Locked Lasers

Jaskiran Kaur

Thesis submitted to the University of Ottawa

in partial fulfillment of the requirement for the degree of

Master of Applied Science in Electrical and Computer Engineering

Department of Electrical and Computer Science Engineering

Faculty of Engineering

University of Ottawa

CONTENTS

LIST OF TABLES

LIST OF FIGURES

ABSTRACT

Mode-locked lasers are essential light sources for generating ultrashort pulses, widely used in high-speed optical communication systems such as Time-division multiplexing and Dense Wavelength Division Multiplexing (DWDM). These lasers are preferred over other light sources for their broad bandwidth, high-peak power and highly coherent light pulses. This work investigates the mode-locking phenomenon in various quantum-sized structures, including multi-quantum wells, quantum dot and quantum dash-based lasers. The primary objective of conducting this research is to gain a deeper understanding of the complex dynamics occurring within the laser cavity. The study employs various numerical modelling, simulations, and experimental analyses to achieve the objective.

Numerical modelling is based on two key approaches: the Time Delay Oscillator (TDO) model and the Delay Differential Equation (DDE) model. Both models use the time-domain lumped element approach to understand the physical processes within the laser cavity. Specifically, the DDE model is developed using the Time Domain Travelling Wave (TDTW) approach to analyze the passive mode-locking phenomenon in lasers. Both models were implemented in the Simulink platform.

The simulation section focuses on the quantum well laser designs due to the current limitation of the Photon Design Tools, Harold and PICWave to support only quantum well-based structures. The parameter values for the quantum well-based simulations from PICWave were extracted to be used in Simulink as PICWave uses a TDTW engine, thus providing a basis for the parameter extraction.

The experimental analysis focuses on quantum dash lasers, examining various aspects of the laser device parameters such as the repetition rate, pulse width, and threshold currents. Additionally, the study investigates the impact of factors such as temperature and injection currents on key parameters like L-I curves, optical spectra, dispersion, and mode-locking behaviour of the laser device.

STATEMENT OF ORIGINALITY

I, Jaskiran Kaur, hereby declare that the work presented in this thesis, titled *"Numerical Modelling, Simulations and Experimental Analysis of Quantum Well, Quantum Dot, and Quantum Dash Mode-Locked Lasers,"* is my original work and has not been submitted to any other organization or institution to obtain another degree. This research was conducted under the supervision of Prof. Trevor Hall.

The Simulink models presented in this thesis were created by Dr. Trevor Hall, while the authors of other models and theories are appropriately acknowledged in the introduction and other relevant sections of each chapter. The experimental measurements presented in this work were performed at the National Research Council of Canada (NRC) campus in Ottawa, jointly by me and Narmada Rajaram, with Dr. Chun-ying Song under the guidance of Jiaren Liu, and Zhenguo Lu. Their respective contributions are detailed in the introduction section of the relevant chapter.

Jaskiran Kaur

January 10, 2025, Ottawa

ACKNOWLEDGEMENTS

I would like to begin by expressing my heartfelt gratitude to my supervisor, Prof. Trevor Hall, for his unwavering support, guidance, and mentorship throughout my master's journey. Thank you for believing in me and patiently addressing my questions at any time of the day. I am also deeply grateful to my co-supervisor Prof. Karin Hinzer for her invaluable support and for graciously presenting me with opportunities to contribute to some exciting collaborations.

My heartfelt gratitude extends to many wonderful people at SUNLAB: John Cook, Paige Wilson, and Gazi Mahamud Hassan, for their support, insightful discussions, and valuable feedback throughout my work. I am thankful to Sebastian Schaefer and Ras-Jeevan Obhi for helping me grasp the fundamentals of lasers and guiding me through Crosslight during the initial stages of my thesis. A special thanks to Christine Couture, the "mini-Google" of SUNLAB, for always being there with answers.

I am also thankful to my collaborators at the National Research Council of Canada (NRC): Jiaren Liu, Zhenguo Lu, Philip Poole, Yang Qi, Xiaoran Xie, and especially Dr. Chun-ying Song. Working with all of you has been a truly enriching experience. Dr. Song, your enthusiasm and curiosity have inspired me, and I will always cherish the joy of sharing experimental excitement with you. My special thanks to my lab mate, Narmada Rajaram, for her patience and teamwork, which made everything come together at NRC by the end of the day.

I would also like to extend my gratitude to my roommates: Rachel Sharp, Alice Wu, Min Tang, and Kimia Hashemi, for their kind words and for creating a positive and supportive environment at home whenever I felt overwhelmed.

A heartfelt thanks to my mother for her constant encouragement, endless prayers, and unconditional love which kept me going. I am equally grateful to my father and uncles for their pride in me and their encouragement to pursue higher education in Canada. To my family and dear friend, Sanjay Prakash Pathak, thank you for listening to my stories and sharing the excitement about my progress.

Finally, I would like to thank myself for staying resilient and patient throughout this journey. Thank you, Waheguru, for making this work possible. A heartfelt thanks to everyone who has been a part of this journey!

ABBREVIATIONS

QWell – Quantum Well

QDot – Quantum Dot

QDash – Quantum Dash

3D – Three-dimensional

DWELL – Dot-in-a-Well

OFDM – Orthogonal Frequency Division Multiplexing

MBE - Molecular Beam Epitaxy

CBE - Chemical Beam Epitaxy

MOCVD - Metal Organic Chemical Vapor Deposition

QWire – Quantum Wire

ES – Excited State

GS – Ground State

VB – Valence Band

CB – Conduction Band

OEO – Optoelectronic Oscillator

TDO – Time Delay Oscillator

TDTW – Time Domain Travelling Wave

DDE – Delay Differential Equation

BPF – Band Pass Filter

LPF – Low Pass Filter

RF – Radio Frequency

WL – Wetting Layer

SRH – Shockley Reed Hall

CW – Continuous Wave

DFB – Distributed-Feedback

L-I – Light- Intensity

OSA – Optical Spectrum Analyzer

TEC – Thermal-Electric Cooler

EDFA – Erbium Doped Fiber Amplifier

LITERATURE REVIEW

Quantum Dot Mode-Locked Lasers

A) Introduction

Mode-locking is a technique used to generate ultrashort pulses with durations in the range of picoseconds ($10^{-12}s$) or femtoseconds($10^{-15}s$) [1]. Typically, a laser device consists of an optical cavity containing the gain and absorber medium, bounded by two reflective mirrors. The photons generated inside the cavity bounce back and forth between the two reflective mirrors (in a Fabry Perot laser) causing constructive and destructive interference between the light waves. This leads to the formation of standing waves, or modes. The standing waves form a discrete set of frequencies known as the **longitudinal modes** (Figure 1) of the laser cavity[1]. These modes are specific frequencies of light waves that oscillate within the laser cavity. Some simple formulations can be used to obtain the number of modes allowed to oscillate inside the cavity as discussed in the book section [2]. In a typical laser, the phase of each mode does not have a fixed relationship with other modes; in a mode-locked laser, each mode has a fixed phase relationship with other modes. Hence, mode-locked lasers are also referred to as 'phase-locked lasers'.

Self-assembled quantum dot structures have attracted wide attention for their application in mode-locked lasers due to their various advantages, such as ultrafast carrier dynamics, high repetition rates, low threshold currents, reduced sensitivity to temperature, 3D carrier confinement, and their ability to generate high power and low-noise optical pulses [3],[4],[5],[6]. Quantum dot structures are the nano-scale semiconductor material in which the carriers like electrons, holes or excitons (electron-hole pair) are confined in all three spatial dimensions [3]. This confinement of charge carriers in a volume on the scale of 1 to 10 nm in size modifies the density of states in the conduction and valence band, thus creating discrete, quantized energy levels [7]. This has a strong influence on the material's electronic and optical properties [3],[4]. Additionally, the shape, size

and distribution of quantum dots over the wetting layer play a crucial role in determining the emission wavelength. These characteristics make quantum dot mode-locked lasers useful applications such as ultra-fast signal processing [8], high-speed optoelectronics, biophotonics, meteorology, frequency comb generation, chirped pulse amplification, OFDM [1],[3],[4],[6].

There have been several instances [9], [10] in which mode-locking was observed in quantum well-based passive mode-locked lasers. However, the quality of mode-locked optical pulses depends strongly on the material, intensity of absorption and temperature variations in the saturable absorber medium [9]. As a result, the mode-locking conditions in saturable absorbers within quantum well lasers are hard to meet due to the strong stability being achieved only in a limited region of bias parameters[10]. This poses limitations for the manufacturing and wide applicability of quantum-well mode-locked lasers. As a result, there is a need for a larger tolerance to variations in operational parameters, which is fulfilled by quantum dot and dash structures. Therefore, these structures have gained widespread attention for their use in mode-locked lasers. They can be grown using Molecular Beam Epitaxy (MBE), Chemical Beam Epitaxy (CBE) and Metal Organic Chemical Vapor Deposition (MOCVD) fabrication techniques [11]. The dimensional size of these quantum structures is comparable to the de-Broglie wavelength of the electrons and holes confined in the semiconductor material. This gives rise to some new quantum mechanical effects that have a significant influence on the optical and electrical properties of the material [7].

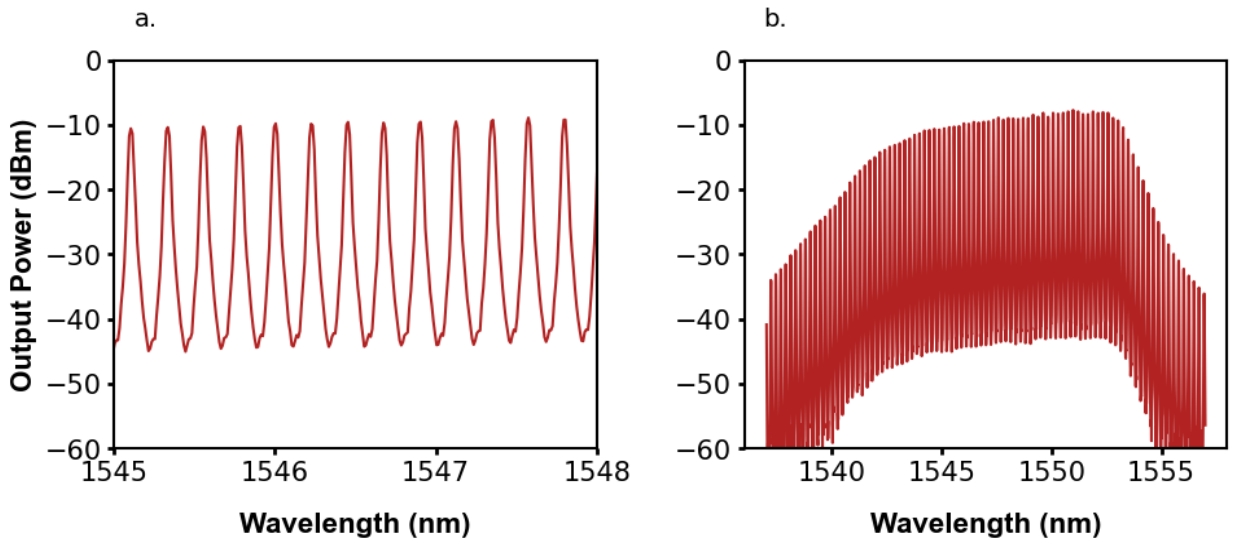

Figure 1: a) Longitudinal modes i.e. the discrete set of frequencies inside the laser cavity. b) The graph shows the output spectrum of a 5-layer Quantum Dash laser.

Let the two mirrors $M_1$and M_2 with reflectivities R_1 and R_2 are separated by the distance l. The cavity length L is denoted as $L = 2l$. In the case of a passive laser device, the attenuation or absorber coefficient inside the optical cavity is denoted by a factor α and the gain coefficient for the active medium is denoted as g. Light waves are electromagnetic waves hence the waves can

be denoted by electric field component $E(t,x)$ as a function of time t and spatial variation x. The electric field at $t = 0$ & $x = 0$ is described as:

$$E(t,0) = R_1 R_2 A e^{[(g-\alpha)l]} e^{j(\omega t - 2\beta l)}$$

To obtain steady-state oscillation, the gain of the light waves reflecting back and forth between the two mirrors must be saturated. Therefore, to consider the gain saturation mechanism the following conditions must be satisfied:

1) The gain saturation according to which the magnitude must be equal to the amplitude A.

$$R_1 R_2 A e^{[(g-\alpha)l]} = A$$

2) The phase condition which says:

$$e^{-j2\beta l} = 1$$

The phase condition is satisfied only if

$$2\beta l = 2\pi m$$

Where $\beta = 2\pi n/\lambda$ with n depicting refractive index, λ is wavelength or modes allowed to oscillate inside the laser cavity.

Substituting the value of β in above equation yields the expression:

$$2\left(\frac{2\pi n}{\lambda}\right) l = 2\pi m$$

$$\boxed{\boldsymbol{\lambda = \left(\frac{2nl}{m}\right)}}$$

where λ denotes the resonant wavelengths or modes of the Fabry-Perot laser.

B) Background

In the 1980s, semiconductor lasers gained widespread attention for high-frequency optical pulse generation due to their compact size, low cost, high mechanical stability and ease of integration with other optical components[10]. Traditionally, these lasers were based on InP material for 1550 nm wavelength applications, with quantum well structures as the active gain medium. Researchers recorded several improvements by using quantum dots as an active medium compared to their quantum well counterparts[3]. Quantum dots offer various advantages, such as low threshold current, increased material gain, high-temperature stability, and high differential gains[8],[11],[12], which led to their widespread attention as light sources in frequency comb generation and many other applications. Apart from the quantum wells, which provide one-dimension carrier confinement, and quantum dots with three-dimensional carrier confinement, there are structures known as quantum wires that display two-dimensional carrier confinement. The lasers developed with quantum wires as the active medium have a lower threshold current than similar structures with quantum wells. Additionally, these structures can be grown on a ridge waveguide. However, quantum wires did not gain widespread acceptance due to the complex, expensive, and precise fabrication techniques required to create uniform structures[3],[13]. Any variations in the quantum wire structure can significantly impact the optical performance of the device. In contrast, the zero-dimension quantum dots can be grown using a self-assembly growth technique, which leads to the random distribution of dots over the top-continuous layer known as wetting layer (WL). This self-assembly growth technique uses the Stranski-Krastanov epitaxial growth process, allowing the nanostructures to synthesize spontaneously. In this process, the thin layers of intended materials are stacked on a semiconductor substrate until a certain critical thickness is reached. Beyond this critical thickness, the planar growth of the film stops, and the island-shaped three-dimensional structures are formed spontaneously due to the relaxation of the accumulated strain developed due to the lattice-mismatched layers. The dots are thus, self-assembled[14]. These three-dimensional islands become self-organized QDots which are formed over a thin continuous film, called a wetting layer, of the same semiconductor material[12],[13],[14]. The thickness of the wetting layer is comparable to that of the QWell and has similar properties[3]. The height of 3-D islands determines the emission wavelength; its size can be adjusted by varying the amount of deposited dot material. However, the substrate temperature as well as the lattice mismatch between the substrate and the material to be deposited are the two most important conditions to adjust the size of the QDots growth by this process[13]. The lattice constant of the deposited material must be higher than the substrate so that the build-up of the strain with each monolayer deposition leads to the formation of these islands [3]. The growth of QDots in the wetting layer is random with sparse density. Hence, a single QDot layer with sparse distribution is not sufficient to deliver the modal gain required for the optimum performance of the laser device. Therefore, multiple stacks of the QDot layers are grown to provide

high modal gain. It is also proven that the multiple stacks do not increase the optical loss, therefore, contributing to an increase in modal gain[3],[8].

The semiconductor materials that grow QDot structures usually belong to groups III-V and II-VI. These materials provide photon emission in the wavelength ranging from 300-1900nm[4]. The group III-V alloy materials can be grown epitaxially Stranski-Krastanov growth method on GaAs and InP substrates using MOCVD or MBE fabrication techniques. This condition is satisfied with the growth of InAs (lattice constant of 6.06A^o) QDots on GaAs (lattice constant of 5.64A^o) and InP (lattice constant of 5.87A^o) substrates[3]. The InAs/InGaAs QDots developed on GaAs substrate have photon emission in the 1100 to 1300 nm wavelength range. In contrast, the InAs/InGaAs QDot lasers developed on InP substrate give emission in the 1400 to 1900 nm wavelength range[8],[4]. Under standard growth conditions, the uneven strain distribution across the InP substrate causes the QDots structures to extend along the transverse length leading to the formation of quantum dash structures. The Quantum dash structures are elongated structures like Quantum wires, that provide 2-dimensional carrier confinement. However, unlike QWires, QDashes have irregular shapes with strong variations in their transverse length and composition leading to a partial 3-dimensional carrier confinement[3],[8]. This offers several advantages such as a smaller linewidth enhancement factor, lower threshold current density for longer cavity lengths and better noise performance over QWell active medium-based devices [8],[11].

A similar but distinct structure, known as the dots-in-a-well (DWELL), consists of layers of QDots are embedded in a strained QWell. This arrangement has been shown to improve threshold current density and increase the emission wavelength of such devices. In this structure, the QWell's thickness is larger than the height of the QDots [15]. As reported in [15], the growth temperature and growth rate of QDots play a vital role in determining the key parameters like threshold current density and emission wavelength of the device. It was reported that the higher growth rate and temperatures in the DWELL design lower the threshold current density of the device.

C) Carrier Dynamics in Quantum Dots

The carrier dynamics of any structure are crucial for understanding its properties and exploiting its potential. The quantization of material to a size comparable to the de-Broglie wavelength of the carriers gives rise to new quantum effects, modifying the density of states from a continuous distribution, in bulk semiconductor materials to discrete sets of delta functions in QDots. This change in the density of states due to the carrier confinement has a profound impact on the optical and electronic properties of the structure.

The bandgap of a material plays a vital role in determining the optical properties, such as the emission wavelength of a semiconductor device. The geometrical constraints introduced in

quantum structures, modify the bandgap (a phenomenon known as bandgap tailoring), which affects the optical properties of the material. In structures like QWells, QDashes and QWires, the quasi-continuous bands still exist, with a change in the sub-band density of states. However, in QDot structures, the continuous energy bands observed in bulk semiconductors and the quasi-continuous energy levels in quantum structures break down to form discrete energy levels due to charge carriers being confined in all three dimensions[3]. The energy level structure of InAs/ GaAs based Stranski-Krastanov self-assembled Quantum Dots is extensively studied theoretically and experimentally to understand the properties of various structures and take optimal advantage of these materials[16].

Figure 2 depicts the energy level diagram in the case of QDots. In this representation, the lowest energy state is referred to as the ground state (GS), with the electron energy considered in the upward direction and hole energy in the downward direction from the edge of the valence band and conduction band respectively. The other states, known as the excited states (ES), represent the discrete energy levels for QDots. According to the author in [17], under the application of injection current or thermal excitation, electrons from the ground state of the valence band jump into the ground state or edge energy level of the conduction band. The free electrons in the conduction band 'relax' into the energy level of the wetting layer. This is shown as R_{pump} in the Figure 2. The carriers are then 'captured' into the quantum dots. The capture process could occur either at the ground or excited state of the dot structure.

Radiative recombination in bulk semiconductors occurs predominantly from the ground state of the conduction band due to the higher probability of electron occupation in these energy states. However, in QDot structures, the emission from both the first excited state and the ground state contributes to the radiative recombination due to the higher probability of electron occupancy at these energy levels. This makes the study of the non-radiative relaxation mechanism between energy levels important. It is reported in [16] and [17], that the relaxation transitions from the wetting layer into the excited or ground state of QDot structures can occur due to two mechanisms: the Auger process or phonon-assisted relaxation process[16]. These transitions occur on sub-picosecond to picosecond time scales [3] depending on the carrier density present in the barrier and wetting layers. When the carrier density is low, the relaxation of carriers occurs primarily due to the phonon-assisted relaxation mechanism, as observed for InAs self-organized QDots grown on the GaAs wetting layer [16]. However, the relaxation process predominantly occurs through Auger processes for higher carrier densities. When electron capture and relaxation to the ground state takes place via phonon emission, the characteristic time for the 'capture' process is usually $1ps$ and for the 'relaxation' process is around $10\ ps$. The longer relaxation time from the top-most excited state to the lower excited or ground state (in case of electrons) slows down the carrier capture mechanism by few nanoseconds (ns) for the next excited state or ground state, a

phenomenon known as **phonon bottleneck** [12]**.** However, when relaxation occurs through Auger process, the relaxation time shortens to approximately $100\ fs$ (femtosecond), making it shorter than the capture time, which is around $1\ ps$. These transition times influence the properties of QDots, resulting in their characteristic ultrafast carrier dynamics[3].

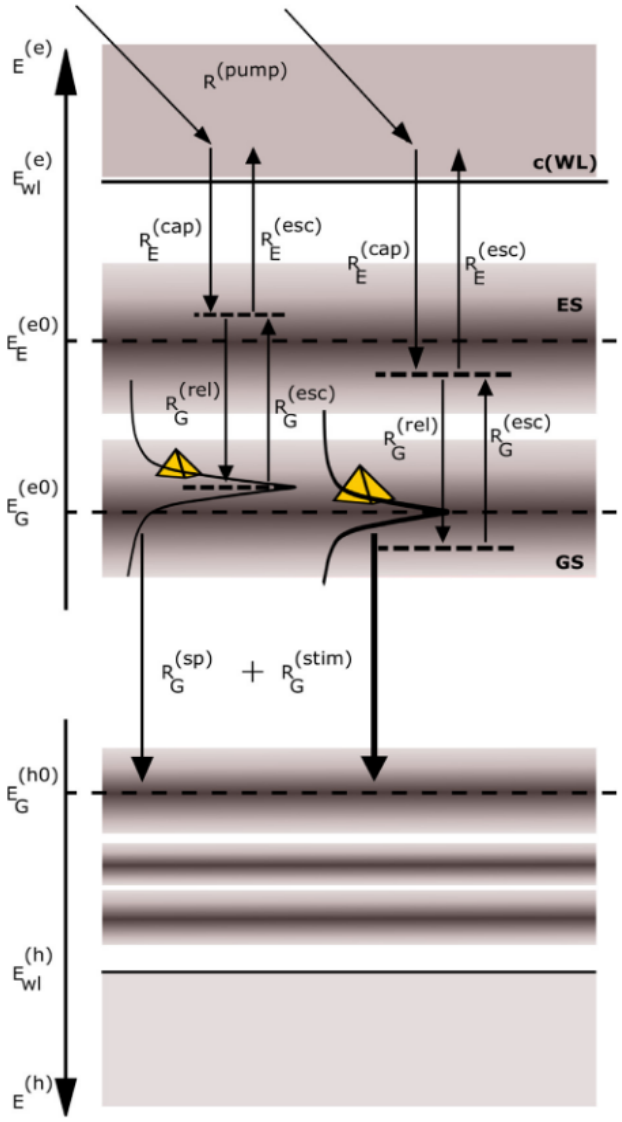

Figure 2: Image depicts the energy level diagram for Quantum dot structures.
Source: Reproduced with the author's permission[3].

CHAPTER 1
Introduction to Thesis

1.1 Introduction

In recent years, the demand for higher bandwidth has increased tremendously, driven by the need for faster and more efficient data transfer. High bit-rate optical networks have emerged as a critical solution to meet these demands, where the generation of pulses with high repetition rates plays a crucial role. Semiconductor laser diodes are well-suited for this purpose due to their ability to generate high-intensity, ultrashort light pulses with compact cavity lengths, allowing the laser to achieve high repetition rates. These pulsed light sources have gathered widespread attention due to their versatility and effectiveness in a wide range of applications including microwave sources, frequency comb generation, and high-speed telecommunication applications [1],[4],[18].

The optical gain, emission wavelength and other parameters are influenced by the type of material and structures used in the active region of the device. These can be Quantum Dashes, Quantum Dots and Quantum Wells. Each of these structures exhibits unique properties, with specific advantages over others. These differences are discussed in detail in Section B) of the literature review.

The mode-locking in semiconductor lasers can be obtained primarily through two techniques- active and passive mode-locking. The active mode-locking technique uses a modulator, such as an electro-optic modulator to modulate the resonator losses and produce a regular pulse train with high repetition rates [19],[20]. In contrast, passive mode-locking uses a saturable absorber to produce ultrashort pulses with shorter pulse durations, but lower repetition rates as compared to active mode-locking [1],[21]. This thesis focuses on passive mode-locked lasers.

The work presented in this thesis examines three types of quantum structures, with each chapter dedicated to exploring the mode locking aspects in QWell, QDot, and QDash laser devices. The Delay Differential Equation (DDE) model describes the dynamics of QWell structures, highlighting the passive mode-locking regime[22]. This model is further extended to QDot structures as described in [5] by Viktorov to explain the mode-locking phenomenon in the device cavity.

A significant portion of this thesis is dedicated to time-domain based numerical modelling, providing an in-depth analysis of the Time Domain Travelling Wave (TDTW) and DDE frameworks. The motivation to discuss these models in detail came from the fact that the commercial simulation platform, PICWave utilizes the TDTW model for time-domain analysis of QWell structures. These time domain models, along with the Optoelectronic Oscillator model, were implemented in Simulink with the primary objective of developing a deeper understanding of the underlying physics causing the laser to operate in mode-locking regime.

This thesis aims to provide a comprehensive understanding of the mode-locking mechanism in semiconductor lasers through a combination of numerical modelling, simulations, and experimental studies.

To achieve this objective, the thesis is structures into three major sections. The first section, comprises of Chapter 2 and 3, provides a detailed mathematical analysis of different time domain models, TDO, TDTW and DDE models. The resulting mathematical expressions from these models were implemented in Simulink.

The second section of the thesis discusses the commercially available simulation platforms: Harold and PICWave in Chapter 4. It highlights the capabilities and presents the simulation of multi-Quantum well laser structures.

The third section addresses the experimental component of the thesis focusing on QDash laser samples. This involves the testing and characterization of laser devices to evaluate key parameters of the device.

1.2 Historical Background

Mode-locking was first observed by Gurs et al. in ruby lasers in the year 1963, followed by Startz et al in He-Ne lasers[23]. Since then, significant advancements have been made in this field. The first reported instance of the mode-locking using an external modulator was reported by Hangrove et al. in 1964. This approach, later termed as active mode-locking mechanism, paved the way for further advancements[1], [23].

The introduction of saturable absorbers within the cavity revolutionized the field in the mid 1970s, driven by the pioneering work by New[24] and Haus[25], [26]. Haus introduced the concept of dynamics involving fast and slow saturable absorbers. Meanwhile, New explains computer simulations of the mode-locking mechanism in dye lasers[23], marking the beginning of a transformative era in laser technology. Subsequently, the integration of semiconductor material into laser devices brought another breakthrough, making the devices more compact and less costly[10].

Several theoretical models were developed to better understand the dynamics of the mode-locking within the cavity. Among the most influential was the master equation introduced by Haus[26]. The work provided a framework for analyzing passive mode-lock mechanism under various assumptions. This seminal work is discussed in the beginning of Section 3.2.

In 1989, Govind P. Agrawal introduced the Time-Domain Travelling model, which explained the gain and phase dynamics of light pulses in semiconductor optical amplifiers (SOAs). The model offered critical insights into non-linear effects such as self-phase modulation, carrier dynamics and, gain saturation mechanisms[27], [28]. By describing the spatio-temporal variations of the field within the laser cavity, Agrawal's model laid the foundation for subsequent innovations.

The TDTW model was later extended to passive mode-locked laser by Koumans et al. [29], and was subsequently adopted by Rosetti et al. for Quantum Dot-based laser devices[30]. This model culminated in the development of numerical models such as the Delay Differential Equation (DDE) model, introduced by Vladimirov et al. in 2004, particularly for passive mode-locked QWell lasers[22]. In the year 2006, Viktorov et al. extended this work to explain mode-locking dynamics in QDot lasers[5].

These foundation models have greatly enhanced our understanding of mode-locking mechanisms and have served as the inspiration for this work. These theoretical models such as the TDTW and DDE will be discussed in detail in the subsequent chapters.

1.3 Thesis Outline

The upcoming chapters discuss various aspects of the work conducted as part of this thesis:

The thesis begins with a **Literature Review** providing a detailed introduction to the mode-locking phenomenon in QDots and a background on the progress and characteristics of quantum-sized materials. It also includes a detailed description of carrier dynamics in QDot materials.

Chapter 1 introduces the thesis, describing the research objectives, motivation, and the historical background about mode-locking mechanism. This chapter describes the work presented in the subsequent chapters to meet these goals.

Chapter 2 explores the applicability of Optoelectronic Oscillator models, developed by Dr. Trevor Hall in Simulink to lasers, as both are examples of Time Delay Oscillators (TDO). The primary objective of this chapter is to enhance the understanding of the complex dynamics occurring within the laser cavity. The chapter discusses the time-domain modelling of lasers as oscillators using the Simulink platform.

Chapter 3 delves into the numerical modelling of QWell lasers in Simulink, based on the Delay Differential Equation (DDE) model first proposed by Vladimirov. It provides an in-depth explanation of the equations used in the model and their implementation in the Simulink platform. It also briefly describes the use case of the model in QDot-based structures.

Chapter 4 focuses on the simulation tools used in this work, such as Harold and PICWave. It highlights the capabilities and limitations of these tools, with an implementation of the QWell-based laser design on a GaAs substrate. Since these tools currently do not support QDot structures, the simulations are restricted to QWell designs.

Chapter 5 discusses the experimental analysis of Quantum Dash lasers, conducted at the National Research Council of Canada (NRC) in Ottawa. This chapter covers the L-I curve measurements, optical spectrum analysis, and RF testing performed on a 5-layer Quantum Dash sample. Additionally, it details dispersion measurements carried out on a bar sample with different geometrical specifications than the laser sample used in earlier experiments.

In the final chapter, **Chapter 6**, an overall summary of the work conducted in this thesis is presented, highlighting the key results obtained and the objectives achieved. The chapter also discusses the future scope of the research, identifying potential areas for further exploration and improvement.

CHAPTER 2
Laser as an Optoelectronic Oscillator Model

2.1 Introduction

The output light from a laser is a result of various physical processes occurring within the resonant cavity. Modelling this complex dynamical behaviour is crucial for understanding the underlying physics and the characteristics of light sources. To address this, the Optoelectronic Oscillator (OEO) Delay Differential Equation model developed by Abhijeet Banerjee and Trevor J. Hall [31] in the Simulink simulation platform is extended to lasers. The DDE-based OEO model discussed in [32] comprises of the complex envelope and reduced phase simulation models based on the injection locking phenomenon with an external source. Since OEOs and lasers are examples of time-delay oscillators (TDO), they share some similarities in their operational principles, hence, the model developed for OEOs can be extended to lasers to understand the complex dynamical behaviour. This extension enabled us to model and better comprehend the complex dynamics of lasers, such as gain amplification, gain saturation mechanism, and the band-pass filtering action of the resonant cavity, which supports the accumulation of specific selective longitudinal modes in the laser cavity. This chapter provides a detailed discussion of each Simulink block used to describe the time-delay oscillator model, which is based on the lumped component approach. In this model, the various processes occurring within the cavity are represented as individual blocks.

Despite their similarities, lasers and OEOs exhibit some key differences. A laser generates optical signals through a resonant cavity containing a sustaining amplifier, while an OEO generates microwave signals via a photonic link. The OEO comprises a pump laser, an optical fibre delay line, a photodetector, and a feedback loop with an intensity modulator, amplifier, and filter. OEOs are known for low-phase noise which is accomplished through a large delay provided by the low-

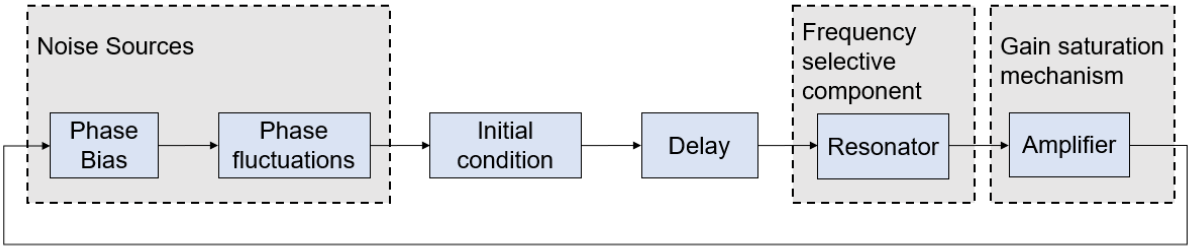

Figure 3: Block Diagram representing Laser as an Oscillator

loss optical fiber transmission line. However, the frequency spacing between adjacent oscillation modes decreases with an increase in delay, posing challenges in designing an RF resonator with sufficient selectivity to suppress side modes. As a result, the multimode operation can be considered an artefact of OEO, with significant implications for their behaviour.

Time-delay oscillators, such as lasers and OEOs, support the oscillation of multiple modes within their links or resonant cavities. Due to the phenomenon of injection, based on an underlying principle of synchronization, these multiple oscillating modes are compelled to align their frequency and phase with light fed from an external source. This process is known as injection-locking phenomenon. The external source is often referred to as the 'master' while the device receiving the input is termed as a 'slave', as described in the reference[33]. In devices that support multimode operation, injection locking can cause spikes when an adjacent mode becomes injection-locked to the initially oscillating mode. This spiking phenomenon results in the coherent superposition of multiple modes, forming a periodic spike train. Over time, this eventually leads to the generation of mode-locked pulse trains. Thus, the spiking phenomenon contributes to the emergence of the mode-locked phenomenon.

2.2 Description of OEO Setup

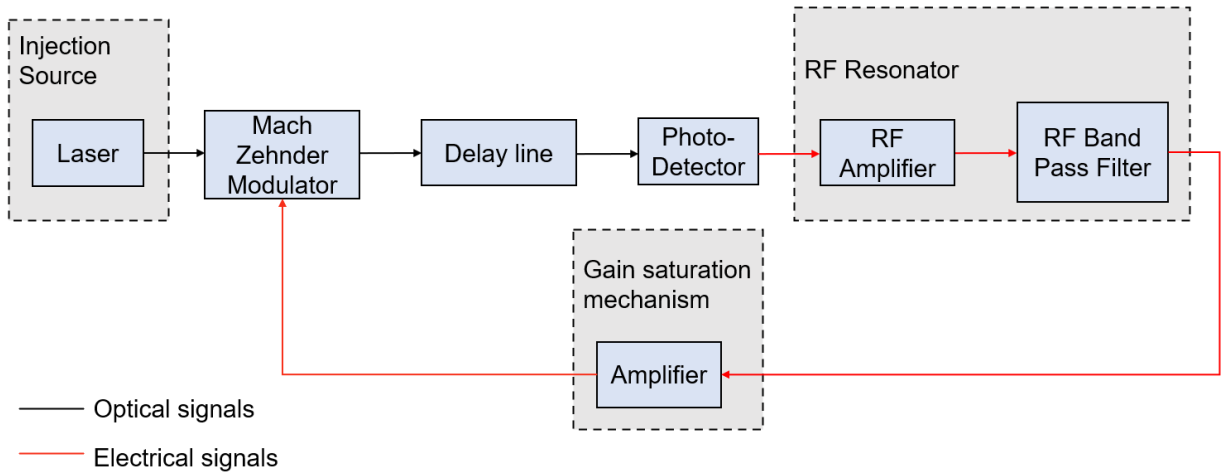

Figure 4: Block Diagram representing Optoelectronic Oscillator setup used in [32]. RF is an acronym used for Radio Frequency.

The OEO model depicted in Figure 4 represents the OEO setup discussed in the reference[32] broadly consists of two main components: an RF photonic link and an RF amplifier link arranged in a loop. The RF photonic link consists of the laser diode which serves as the external light source ('master'), a Mach Zehnder modulator (MZM) functioning as the intensity modulator, an optical fiber introducing the delay τ_D in the link, and a photodetector that recovers intensity-modulated RF signal generated by MZM. These components decide the time delay of the oscillator. Whereas the RF amplifier link consists of an RF amplifier and an RF band pass filter (BPF), also referred to as an RF resonator with an on-resonance group delay τ_R. The RF amplifier acts as a sustaining amplifier, while the RF BPF ensures that only desired modes are sustained within the link. The overall round-trip time becomes $\tau_G = \tau_D + \tau_R$ and usually $\tau_D \gg \tau_R$.

The OEO models described in the article[32] are based on injection-locking phenomenon from an external source, which, in this case, is the laser. However, if we only consider the **free-running oscillator, i.e., without injection locking, the free-running oscillator model essentially represents the behaviour of a laser** as shown in Figure 3. The fundamental principles are same for lasers and optoelectronic oscillators as both are examples of time delay oscillators.

2.3 Functionality of Free-running OEO Simulink Models

a)

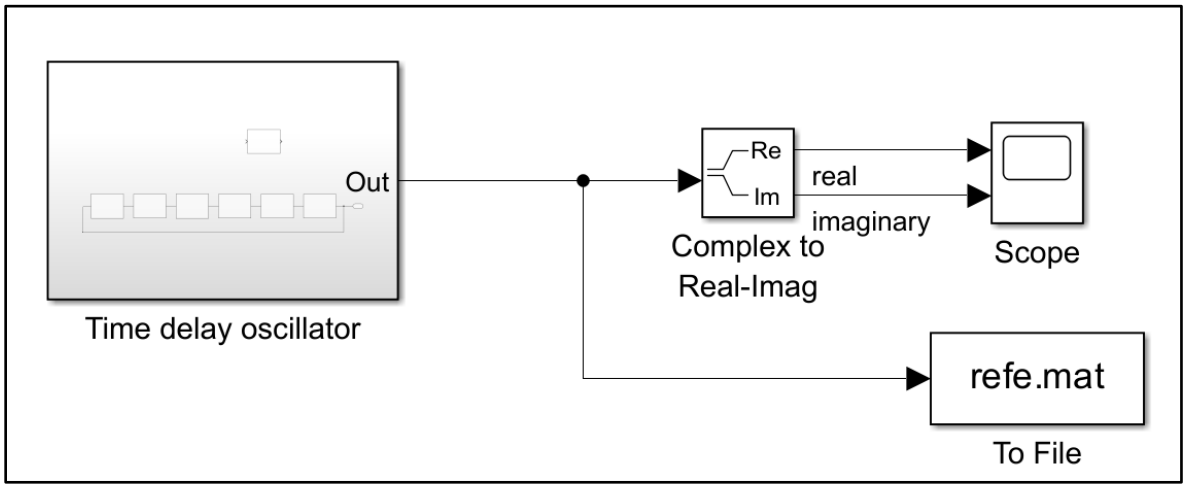

b)

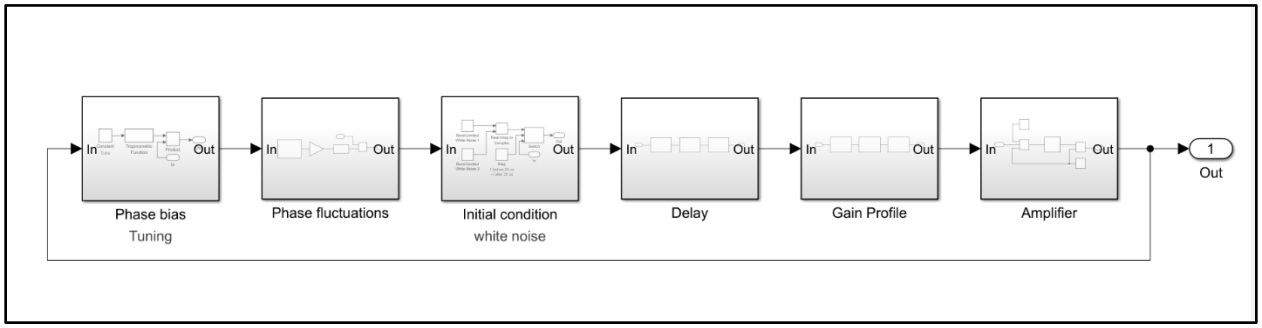

Figure 5: a) Block diagram of Time Delay Oscillator envelope model.
b) Block diagram depicting the constituents of the Time Delay Oscillator block.

At first, the transients or noise considered in the phase bias block causes the initial buildup of oscillations. The phase fluctuation block introduces different types of noise like Brownian motion, flicker, and white noise responsible for introducing phase noise inside the system. The initial condition subsystem blocks are necessary to set initial conditions for the system. There are various initial conditions which could be specified depending on the type of oscillations we want to build inside the loop. During the buildup of oscillations, the saturating amplifier operates in a linear region allowing the oscillations to grow in magnitude. The growth rate of the oscillation mode is directly proportional to the net gain it encounters during each round-trip. Following this is a delay block which introduces the delay τ_D into the system to model the round-trip time of the modes in the cavity. The modes then pass through an appropriately tuned BPF block with a bell-shaped transmission function. The BPF block supports the growth of one mode over the other modes. The gain control mechanism allows the saturating amplifier to reach saturation, which lowers the

round-trip gain and maintains it at a constant value as the oscillation's magnitude increases[34]. This allows the desired mode to be sustained by net unit gain, while the neighbouring modes gradually suffer net loss, causing them to slowly decay. The sidemode spectral components continue to modulate the phase of the oscillation, while the gain control mechanism maintains the oscillation's magnitude at a steady value once it has been achieved.

The dynamic equation describing the free-running OEO is given as[32]:

$$v = e^{i\phi} K(h \otimes (D_{\tau_D} v)) \tag{2.3.1}$$

where v is the complex envelope of the oscillator's output.

D_{τ_D} describes the delay operator implemented by the delay subsystem of the Simulink model. This can be expressed as:

$$(D_{\tau_D} v)(t) = v(t - \tau_D) \tag{2.3.2}$$

$h \otimes$ implemented by the Gain profile or band-pass filter block, describes the convolution between the filter and the complex envelope of the oscillator's output after passing through the delay block.

K describes the amplifier block which plays an important role in the gain saturation mechanism. The phase of the output complex envelope from the amplifier block is similar to the input complex envelope. However, after each round trip, the magnitude keeps on increasing, to control the increasing magnitude, the amplifier block implements a user-defined Matlab code which provides the magnitude equivalent to unity.

$e^{i\phi}$ describes the net phase contributed by the intra-loop and other components. This part is introduced by the Phase bias block.

2.4 Complex Envelope Simulink Model

Since the behaviour of the free-running optoelectronic oscillator (OEO) model closely resembles that of a laser, only the free-running OEO models will be discussed in detail in this thesis. The blocks discussed in this section are based on the complex envelope method, in which the oscillation is described as:

$$v = a_v e^{i\theta_v} \tag{2.4.1}$$

where v represents the complex envelope of the oscillation.

The real part of the complex envelope is given by:

$$Re(v e^{i\omega_0 t}) \tag{2.4.2}$$

where ω_0 is the nominal frequency. The nominal frequency is chosen to be close to the oscillating frequency such that the magnitude a_v and phase θ_v can be considered as slowly varying under 'slowly varying approximation'.

The gain control mechanism implemented by the BPF and amplifier effectively suppresses the amplitude fluctuations but cannot maintain a constant phase of the oscillation, as the sidemode spectral components modulate the phase. Under certain approximations, the magnitude of the oscillations is held constant, and amplitude fluctuations are significantly suppressed. This allows the complex envelope to be simplified into a reduced-phase model. In the reduced-phase model, the dynamical equation (2.3.1) is simplified to an equation involving only the phase θ_v.

By using equation (2.4.1), the dynamical equation in terms of phase is given as:

$$\theta_v = \phi + h \otimes (D_{\tau_D}\theta_v) \tag{2.4.3}$$

Here, θ_v describes the phase of the free-running oscillator.

ϕ represents the phase introduced due to the intra-loop and other components.

The dynamical equation solution for free-oscillating modes can be described as:

$$v(t) = a_p e^{s_p t} \; ; s_p = \sigma_p + i\omega_p \tag{2.4.4}$$

To sustain oscillations, the oscillator must satisfy the Barkhausen criteria. According to these criteria, the magnitude of the dynamical equation represented in (2.3.1) must be unity, and the phase must equal to $0°$ or $360°$ or multiple of 2π.

Using equation (2.4.4) and applying the Fourier transform to expression (2.3.2), the Fourier domain representation of equation (2.3.1) becomes:

$$\kappa H(s_p) e^{i\phi} e^{-s_p \tau_D} = 1 \tag{2.4.5}$$

The magnitude and phase criteria for the above expression are given as:

$$\kappa \left| H(s_p) \right| e^{-\sigma_p \tau_D} = 1 \tag{2.4.6a}$$

$$2\pi p + \phi + \angle H(s_p) - \omega_p \tau_D = 0, \qquad p \in Z \tag{2.4.6b}$$

Here, κ represents the saturated gain determined using the describing function method. The gain saturation mechanism ensures that the oscillator's magnitude remains constant, thereby setting $\kappa = 1$. This also helps maintain the oscillation frequency of the oscillator close to the centre frequency of the BPF.

The integer p denotes the number of cycles, with mode p oscillating within the resonant cavity of the oscillator.

The BPF acts as a phase filter. It allows only a specific oscillation mode to sustain and results in all the other modes oscillating the cavity to decay with time. However, to obtain sustained multimode oscillations, either the resonator block must be removed entirely, or the Gaussian-shaped passband filter must be replaced with flat-top passband filter to allow the maintenance of various multiple modes in the cavity. In this case, the impulse response for the flat-top filter is given by the Dirac delta function is derived in detail in Appendix Section II).

2.5 Functionality and Description of Simulink Blocks

2.5.1 Phase Fluctuation Block

The phase fluctuation block is used to introduce some disturbances in the phase of the modes oscillating inside the loop. This introduces phase noises within the system to increase the model's practicality. The Product and Gain blocks form a phase modulator that acts on the output generated from the Gain and Power law fluctuation blocks. The Gain block controls the overall fluctuations pertaining in the loop.

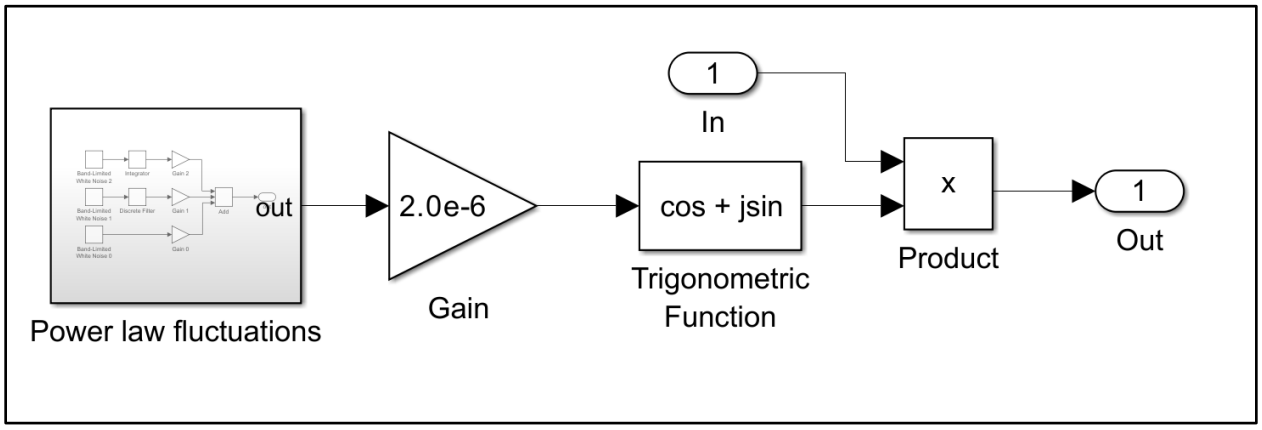

Figure 6: Block diagram illustrating the components of phase fluctuation block.

The trigonometric block converts the fluctuations into a complex envelope, which is then introduced into the signal coming through the feedback. This is achieved by multiplying the signal with the phase fluctuation's complex envelope.

2.5.2 Power Law Fluctuation Block

The Power fluctuation block consists of three arms: the arm with Gain 0 generates white noise (f^0) , the arm with Gain 1 introduces flicker noise (f^{-1}), and the arm with Gain 2 produces Brownian fluctuations (f^{-2}), also known as random walk fluctuations. These stochastic Gaussian

noise processes are generated using Band-Limited White Noise blocks. The various types of phase noises are discussed in detail in the book section presented in reference[35].

a) **b)**

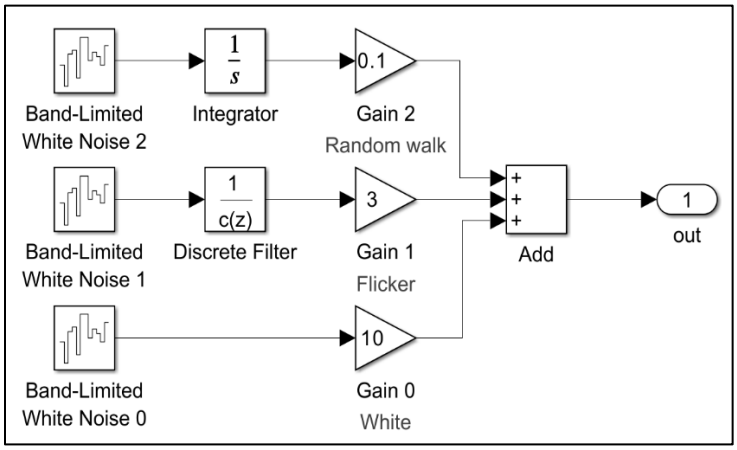


```
% discrete filter coefficients
m = 30000;
c = zeros(1,m);
c(1) = 1;
for k=1:(m-1)
    c(k+1) = ((2*k-3)/(2*k))*c(k);
end

% white noise block seeds
rng('default'); % reset global stream
s = randi(10000,[1,10]);
```

Figure 7: a) Schematic diagrams illustrating the three arms of the Power Law Fluctuation subsystem. b) MATLAB code implementing the discrete filter block located in the second arm of part (a), designed to simulate flicker noise.

The values for the Gain blocks are selected based on the experimentally measured OEO phase noise spectral density data presented in[32]. White noise accounts for thermal and shot noise inherent in semiconductor optoelectronic devices due to temperature and current pulses respectively. Since white noise is an additive noise which is always present in the system, it does not require filtering. The arm responsible for flicker noise utilizes a Discrete Filter block, while the arm with Brownian motion uses an integrator to generate a Brownian motion stochastic process. This method is talked about in detail in[36].

2.5.3 Initial Condition Blocks

The initial condition blocks offer the initial conditions for the single mode or multimode oscillation states. The Delay Differential Equation described for the time delay oscillator requires some initial conditions for the loop. The initial conditions discussed in the chapter form an infinite dimensional vector space.

a) Initial condition (Bessel mode)

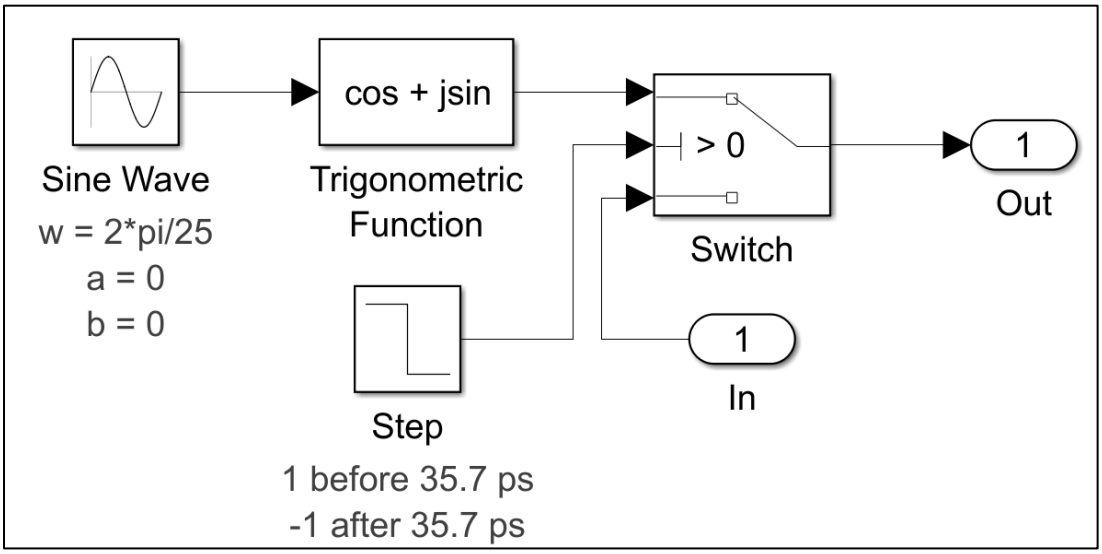

Figure 8: Schematic diagram showcasing the elements of Bessel-initial condition.

Each initial condition i.e. Bessel mode and white noise condition have different purposes. The Bessel mode initial condition is used when a frequency comb-like initial condition is required. In contrast, the white noise initial condition is useful in cases when the oscillation buildup from noise or the evolution of single-mode oscillation from multimode oscillations has to be portrayed.

The switch block passes through the first input when the criteria selected is achieved at input 2. Input 1 i.e. $\cos\left(\frac{2\pi}{25}\right) + isin\left(\frac{2\pi}{25}\right) = 0.9685 + i0.2486$ is passed as an output before $35.7\ ps$ of the simulation time else, the feedback signal is obtained as the output with $180°$ phase shift.

The sine wave and trigonometric block forms a complex envelope of the carrier. The phase of the carrier depends upon the parameters of the sine wave block. The parameters like frequency (in our case $\frac{2\pi}{25}$), amplitude a, and bias b, are the parameters of sine block.

b) Initial condition (white noise):

The working of the white noise block is similar to the Bessel mode block as explained above. Here, two band-limited white noise blocks are used to generate random numbers which are then converted into complex numbers by using real & imag to complex conversion block. The switch connects the first input i.e. the complex envelope signal to output until a condition specified at input 2 is met. Once the condition specified is met at input 2, the input at port 3 is fed at the output.

The random noise values generated by the band-limited white noise blocks are coded via a Matlab program, as shown in part b of Figure 7. The code produces 1×10 row vector of random integers, with each integer value ranging between 1 and 10,000.

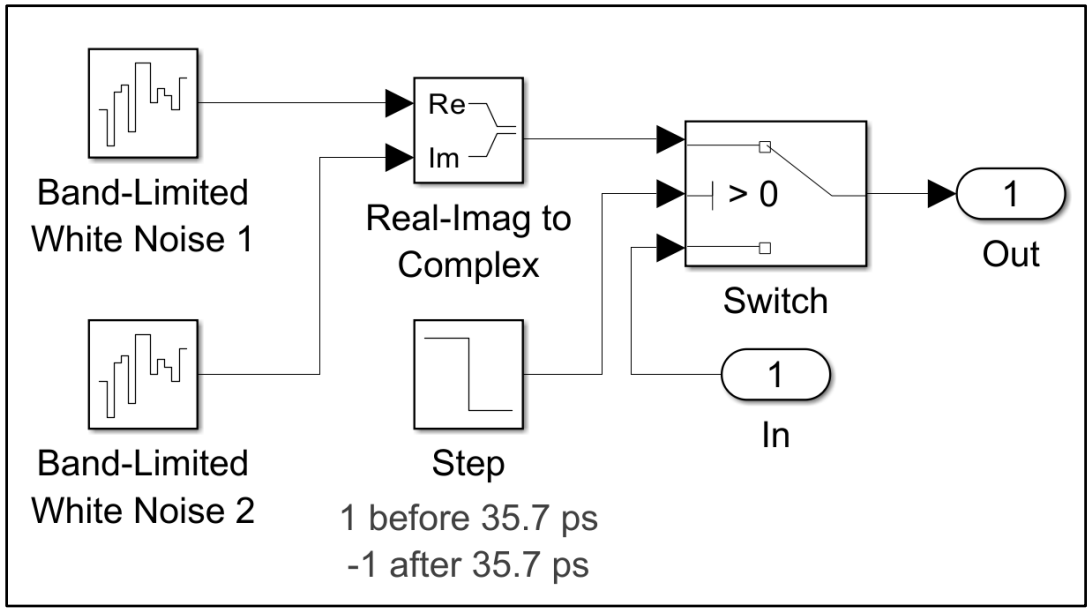

Figure 9: Block diagram describing the white noise initial condition.

2.5.4 Delay subsystem

The delay operator $D_{\tau D}$ is accomplished using delay block. The transport delay block only accepts real vectors, not complex input and output variables. Two conversion blocks are used to delay the input signal: one from complex to real at the start and another from real to complex at the end. This block depicts the roundtrip time of the laser cavity. Hence, the value $35.7\ ps$ depicts the cavity round-trip time of the simulated device parameter.

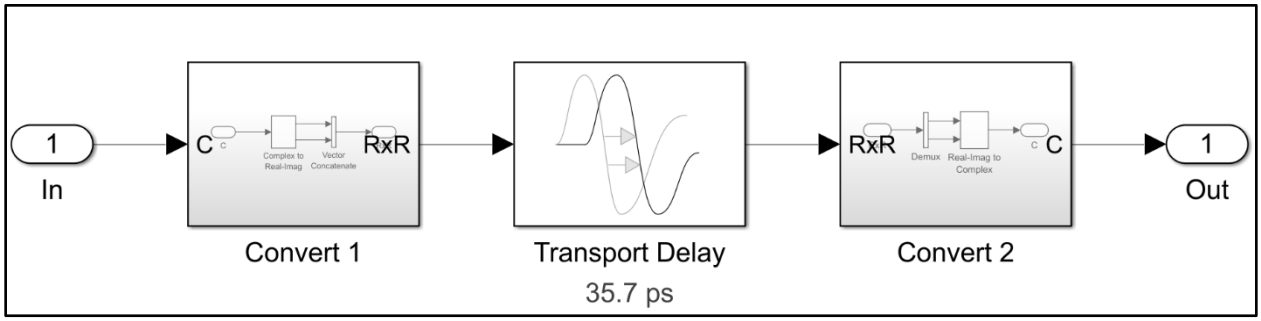

Figure 10: Block diagram illustrating the Delay subsystem. This block decides the cavity round-trip time of the simulated laser device.

2.5.5 Phase Bias or Phase Shifter Block

The functionality of phase bias block can be understood with some examples-

a)

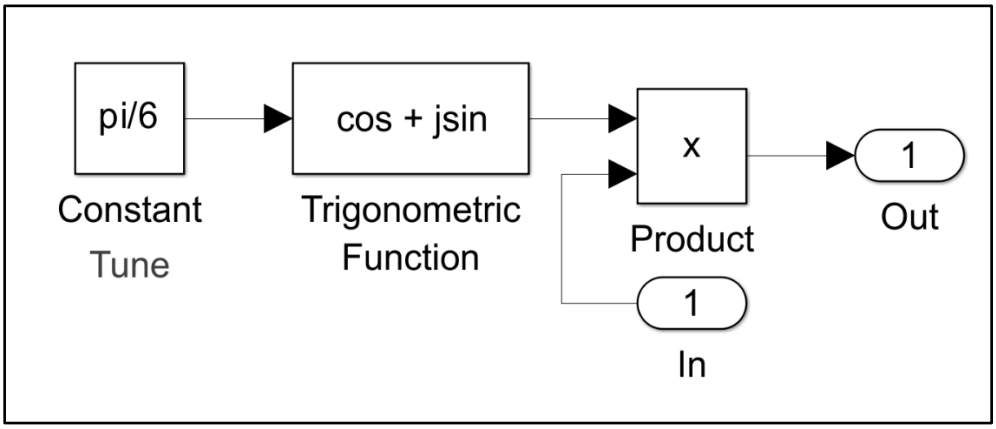

b)

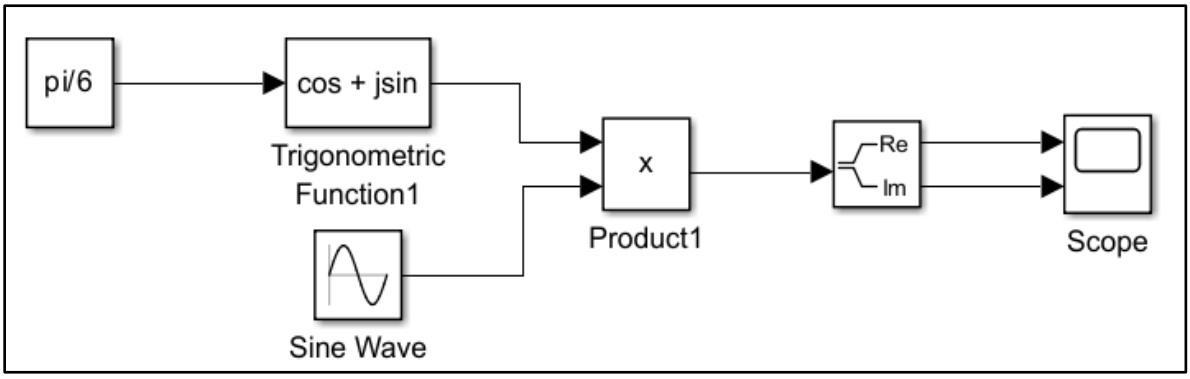

Figure 11: a) Illustrates the internal components of the Phase Bias block with the angle set to π/6.
b) A block diagram presenting an example to demonstrate the functionality of the Phase Bias subsystem using sine block.

In the example depicted in Figure 11a), the angle is chosen to be $\frac{\pi}{6}$. Thus, the output generated from the trigonometric block will be constant values for the real and imaginary parts. When these values are multiplied with a sinusoidal function, the overall output generated by the block is:

$$\left[\cos\left(\frac{\pi}{6}\right) + jsin\left(\frac{\pi}{6}\right)\right] \sin(2\pi ft)$$

$$\Rightarrow \quad [0.866 + j0.5] \sin(2\pi ft)$$

$$\Rightarrow \quad \underbrace{0.866 \sin(2\pi ft)}_{\text{Real}} + \underbrace{j0.5 \sin(2\pi ft)}_{\text{Imaginary}}$$

There is no phase shift in the dummy input sine wave signal; only a variation in magnitude is observed. Hence, the sine function does not fulfill the purpose of providing phase bias. However, when a ramp signal is used instead of the sine wave and fed into the trigonometric block, which is then multiplied with the above expression, a phase shift is obtained. This is illustrated in the following example:

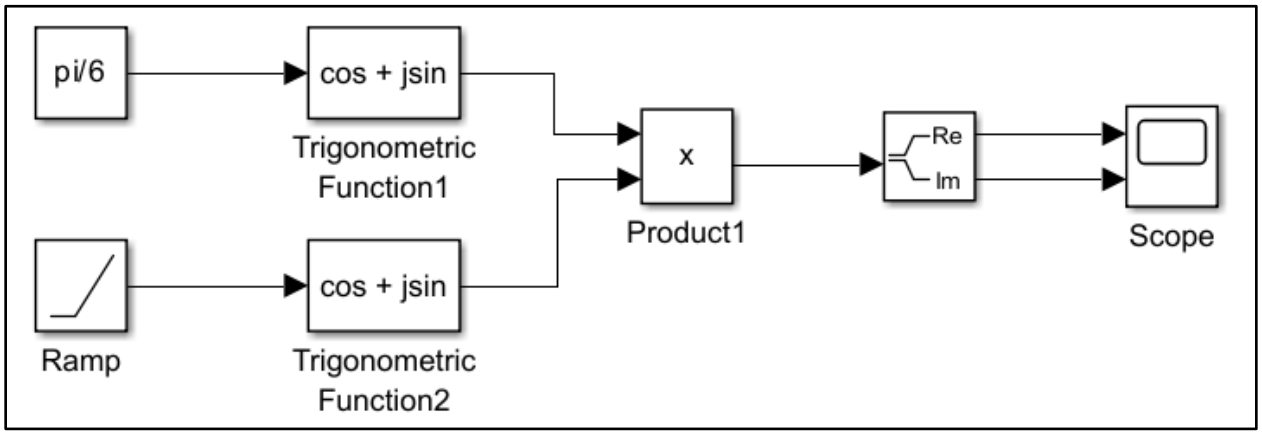

Figure 12: Block diagram depicting an example demonstrating the functionality of the Phase Bias subsystem by using the ramp signal.

$$tu(t)[cos + jsin].\left[\cos\left(\frac{\pi}{6}\right) + jsin\left(\frac{\pi}{6}\right)\right]$$

$$\Rightarrow [\cos(t) + jsin(t)].[0.866 + j0.5]$$

$$\Rightarrow [0.866\cos(t) + j0.5\cos(t) + j0.866\sin(t) - 0.5\sin(t)]$$

$$\Rightarrow [0.866\cos(\mathrm{t}) - 0.5\sin(t)] + j[0.5\cos(t) + 0.866\sin(t)]$$

$$\Rightarrow [0.866\cos(\mathrm{t}) - 0.5\cos(90° - t)] + j[0.5\cos(t) + 0.866\cos(90° - \mathrm{t})]$$

There is a phase shift

The latter example demonstrates that the phase bias block works as a phase shifter when a feedback signal from the loop is fed into the subsystem.

2.5.6 Gain Profile Subsystem

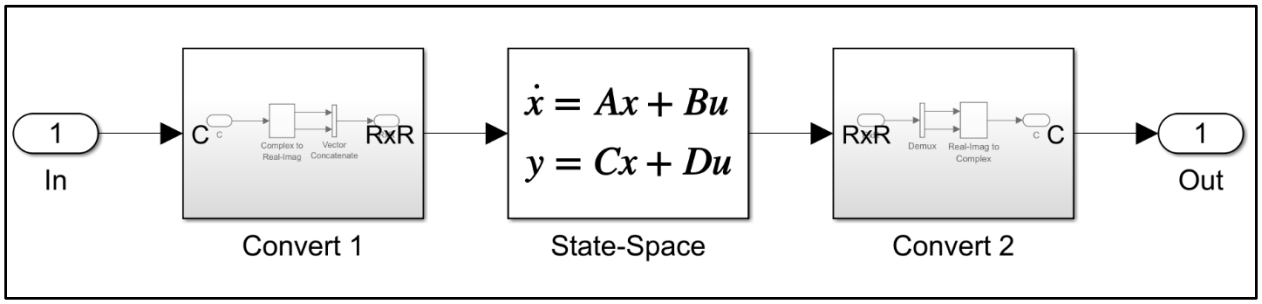

Figure 13: Schematic representation of gain profile subsystem executing band pass filter.

The convolution operator $(h \otimes)$ in equation $e^{i\phi}K\big(h \otimes (D_{\tau D}u)\big)$ is implemented using the gain profile block. Since the state-space block does not support complex scalars, therefore, the incoming complex envelope signal is first converted into real vectors before being fed into the state-space block. Similarly, the output is converted back from real to complex and passed to the subsequent blocks.

The state-space block implements a single-pole Low-Pass Filter (LPF), which is equivalent to a Band-Pass Filter (BPF). The details of baseband equivalence between the LPF and BPF are explained in the Section I) of the appendix. By comparing the state-space equations with the low-pass filter equation (16) in the appendix, the variables A, B, C, and D for the single-pole baseband LPF, which is equivalent to BPF are obtained as:

$$\boldsymbol{A = -I/\tau_R}$$

$$\boldsymbol{B = I/\tau_R}$$

$$\boldsymbol{C = I}$$

$$\boldsymbol{D = 0}$$

where τ_R is the on-resonance group delay of the resonator or gain profile block, and I is the 2×2 identity matrix.

2.5.7 Gain Saturating Amplifier

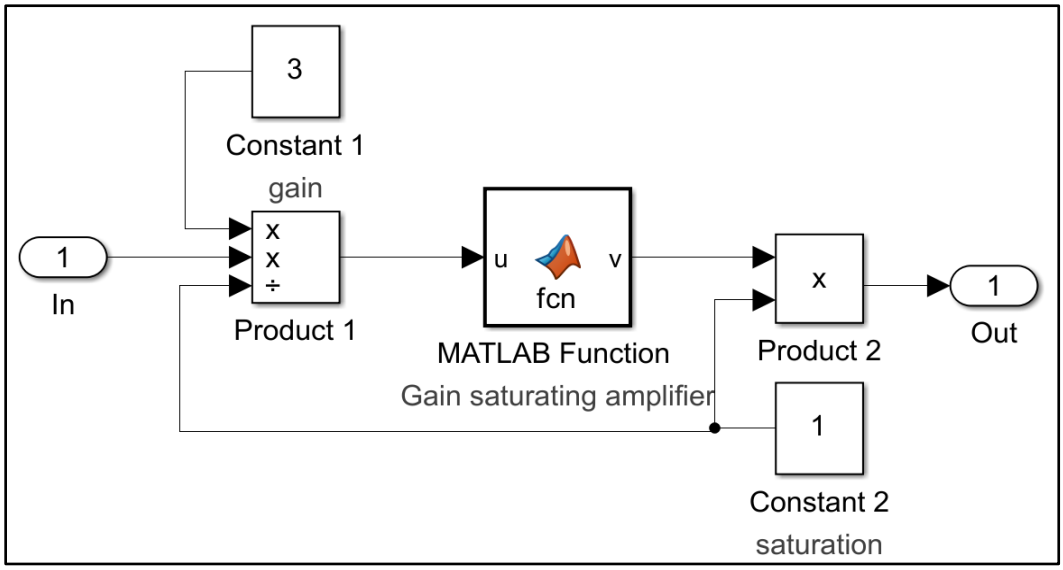

Figure 14: Schematics of Simulink depicting the gain saturation mechanism.

The operator K in equation (2.3.1) is implemented by the amplifier block. It is responsible for providing the gain saturation mechanism by maintaining the increasing magnitude of the complex envelope of the modes oscillating inside the loop to a unit gain-saturated value whereas the phase of the output complex envelope signal remains the same as the input signal. The gain saturation amplifier block uses a Matlab code to implement the equation which provides saturable gain with unit linear gain.

```
function v = fcn(u)
% Amplifier gain saturation model
% unit linear gain
% unit magnitude saturation

a = (4/pi)*abs(u);
if a<=1
    v = u;
else
    th = 2*acos(1/a);
    v = (1 - (th - sin(th))/pi)*u;
end
```

Figure 15: MATLAB code implementing gain saturation mechanism

2.6 Description of Simulation Results

All the blocks discussed above are arranged into a loop, as shown in Figure 5, to enable the build-up of sustained oscillations from the specified initial conditions within the loop. The simulation results obtained vary based on the initial conditions, as discussed earlier.

The total simulation time of the models is considered as $1\ ps$, with the round-trip cavity time for the simulation being $35.7\ ps$.

2.6.1 White noise initial condition

When the simulations are run with white noise initial condition, the real and imaginary components of the time-domain results of the modes oscillating within the loop look like the ones shown in Figure 16.

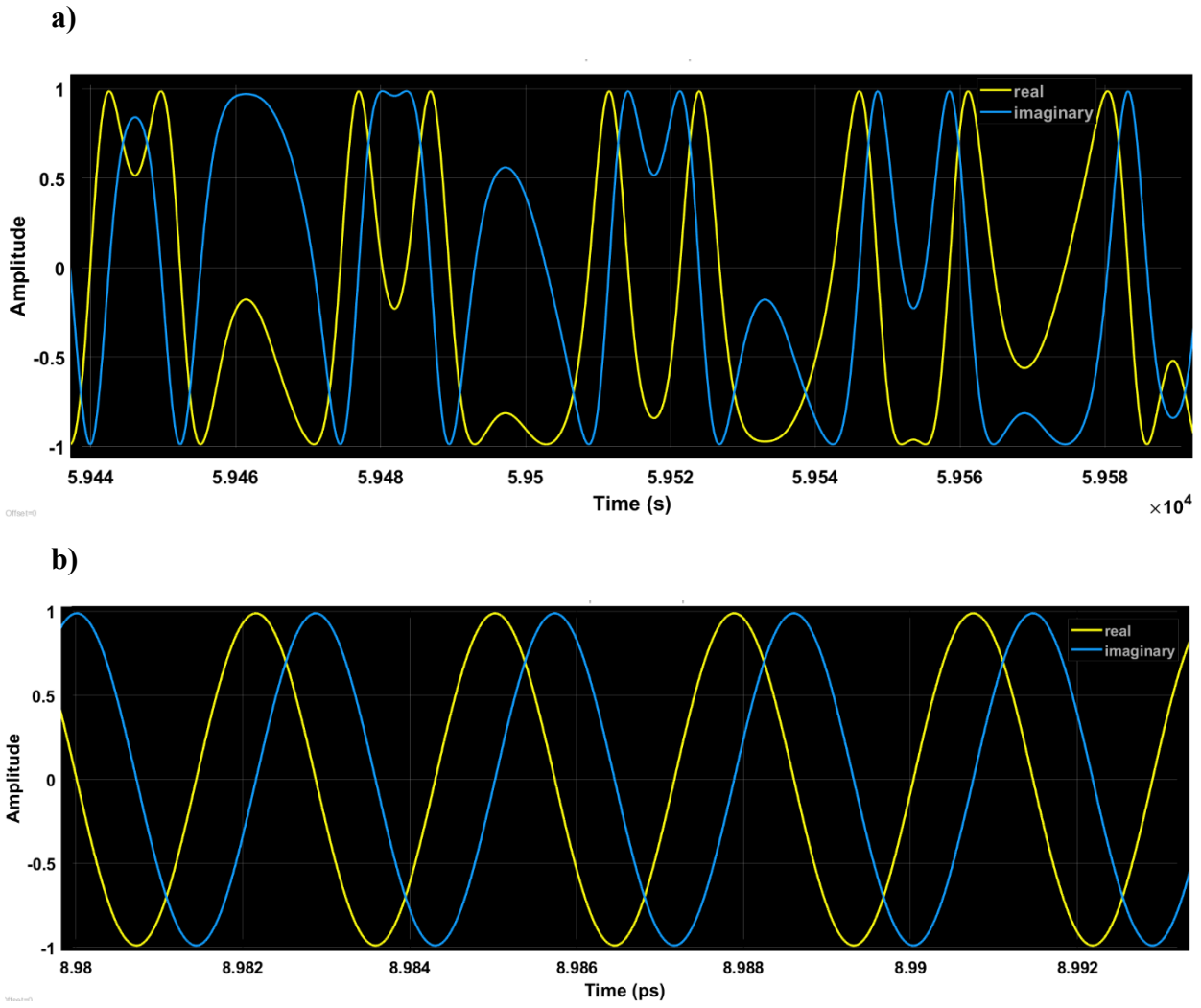

Figure 16: The results highlight the build-up of sustained oscillations from the noise introduced by the white noise initial condition block.

Figure 16 shows the results for white noise initial condition. Part a) of the figure highlights the gradual evolution of sustained oscillations (as shown in part b) from a random Gaussian distributed complex noise. This initial noise serves as the trigger for the oscillation build-up, which ultimately stabilises into a steady oscillatory state within the loop as the time progresses.

The spacing between the two consecutive peaks is 28 GHz, which corresponds to the inverse of the delay time of the model. This spacing also represents the pulse repetition rate of the simulation.

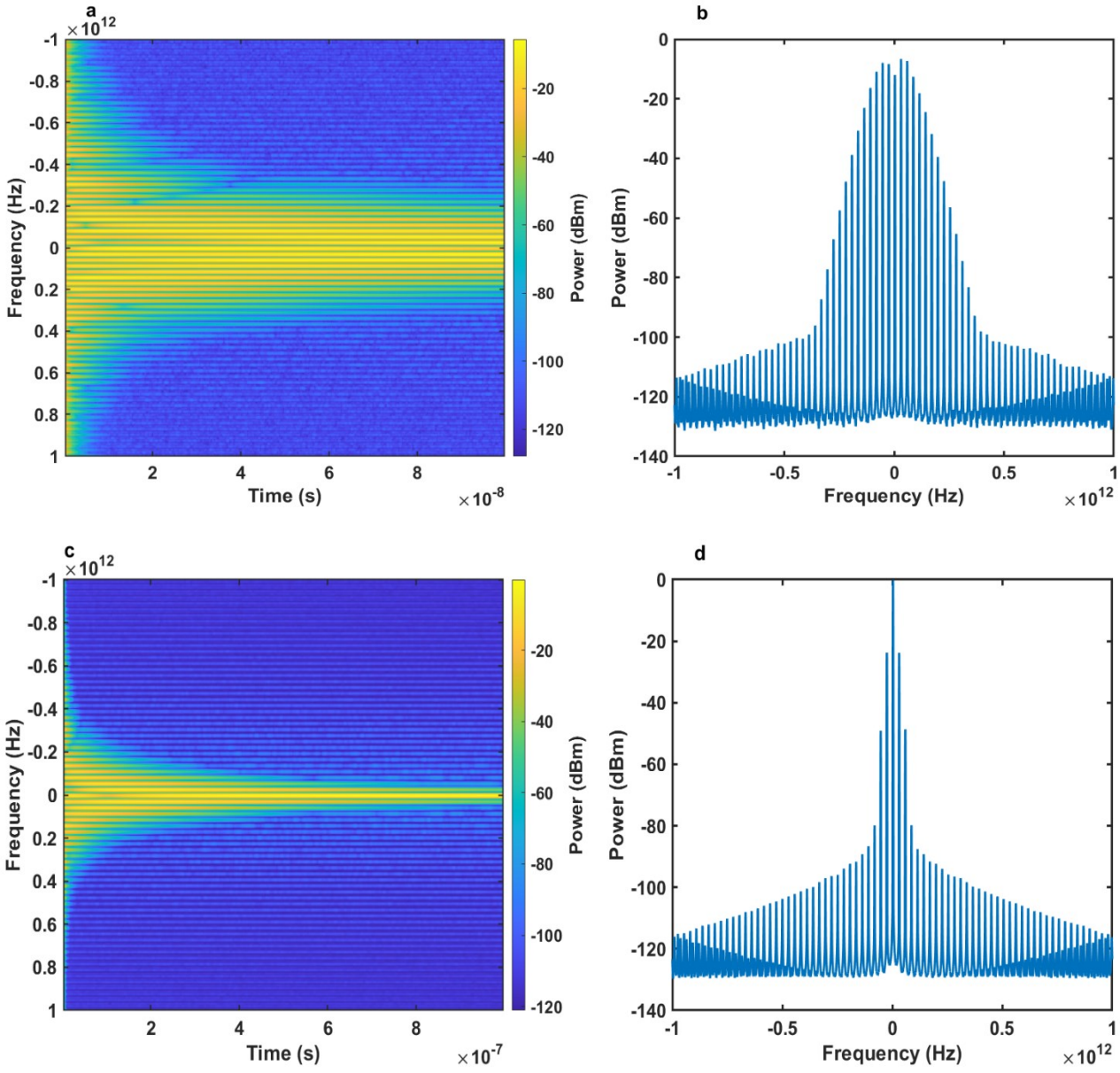

Figure 17: The simulation results for white noise initial condition highlight the time-evolving power spectra of laser at different simulation times. The results in a) and b) show the spectra obtained when the simulation time is set to 0.1 ps. *In contrast, figures c) and d) illustrate the spectra results for a simulation of* 1 ps.

Figure 17 presents the time-evolving light output (on the left) and optical power spectra (on the right) of the laser output under a white noise initial condition, captured at various simulation times. The time-evolving spectrum is a valuable tool for understanding the laser's dynamic properties and operational parameters. It provides information about the dominant mode oscillating within the cavity, as is shown in part d) of Figure 17, and indicates whether the laser has achieved stable output or exhibits any unstable dynamics and fluctuations. Additionally, it provides information about the critical parameters such as the pulse repetition rate, side modes and the presence of noise within the loop.

In part a) of Figure 17, the results highlight the presence of multiple modes oscillating within the loop at a simulation time of $0.1\ ps$. The result in part b) represents the frequency comb spectrum of the mode-locked laser. Over time, the band pass filter gradually suppresses the side modes, allowing a single mode to dominate and oscillate within the loop. This transition reflects the laser's evolution towards single-mode operation, also highlighting the changes in spectral intensity and energy distribution in Figure 17a).

Due to the Gaussian or bell-shaped profile of the band pass filter, the side modes decay slowly with time. This decay is more evident in parts c) and d) of Figure 17 when the spectrum is recorded for the simulation time of $1\ ps$. However, the side modes are not suppressed completely indicating the practicality of the model.

2.6.2 Bessel mode initial condition

a)

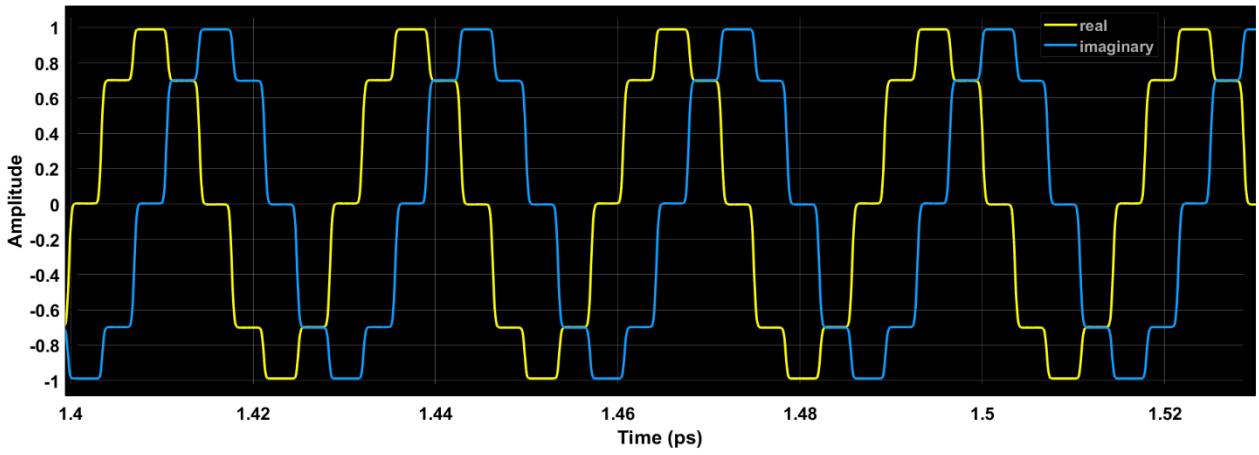

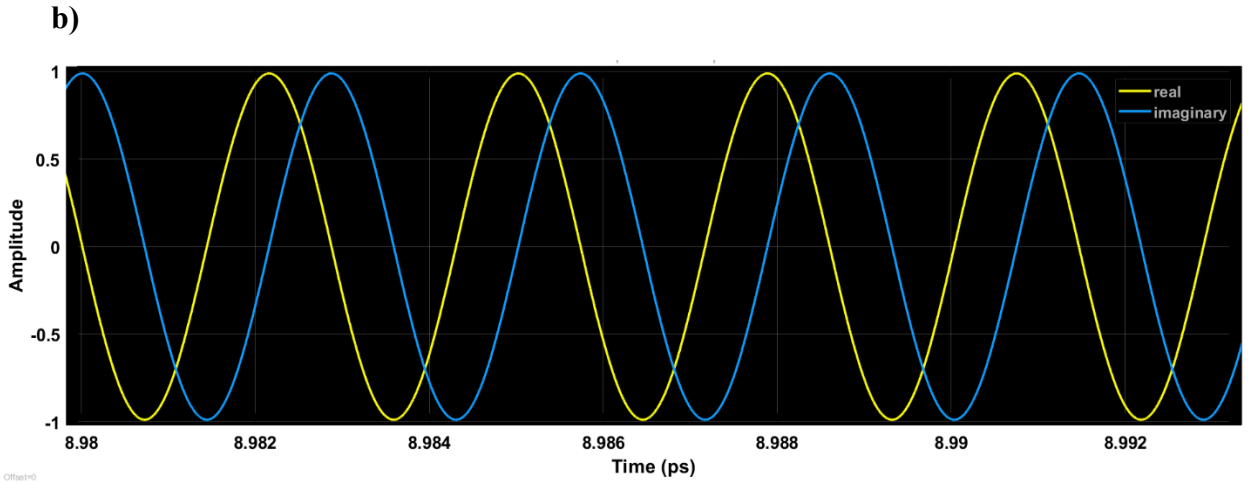

Figure 18: Illustration of the transition from early staircase-shaped oscillations to complex stable oscillations. The staircase-shaped oscillations arise due to the Bessel-mode initial condition block.

The Bessel mode initial condition causes the early oscillations to resemble a staircase waveform, which eventually stabilizes into complex, steady oscillations. This initialization method uses the Bessel function to define the system's starting conditions. As previously discussed for the white noise initial condition, the results in Figure 19 showcase the system's behaviour under varying simulation times.

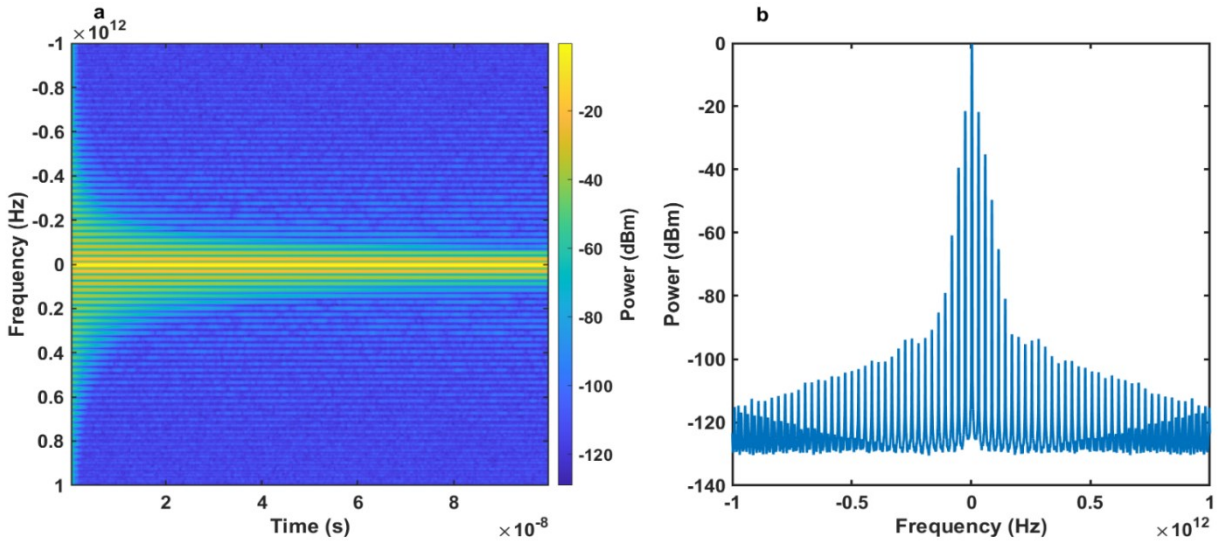

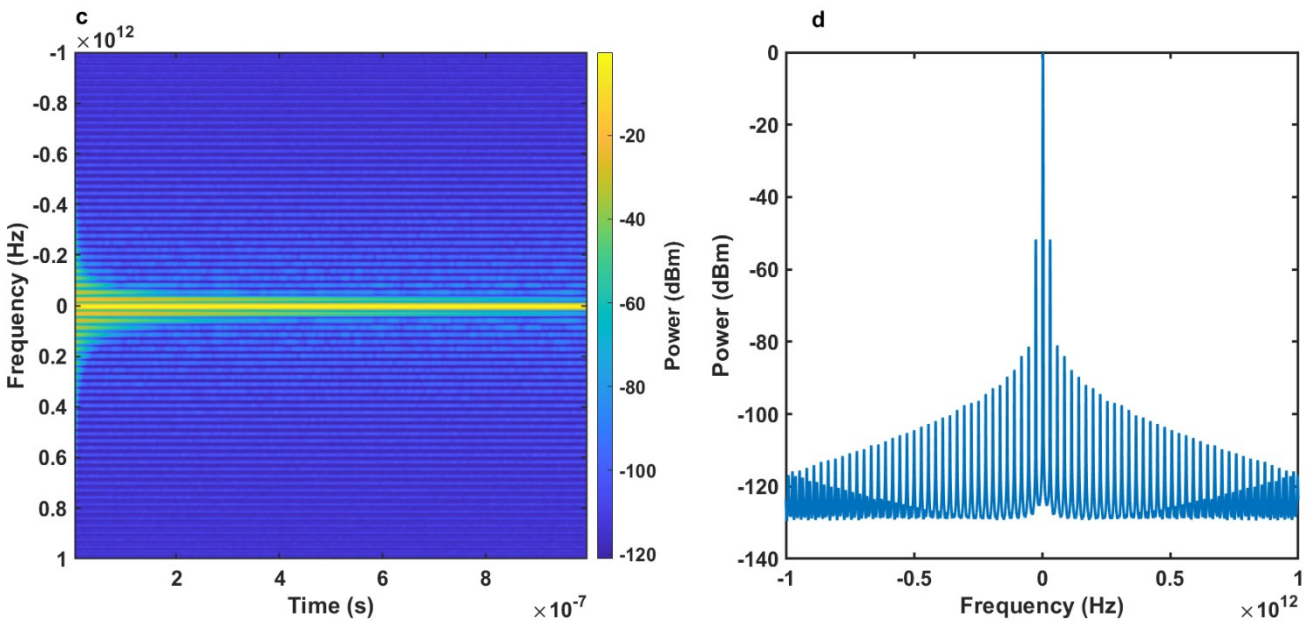

Figure 19: The results for Bessel mode initial condition highlight the time-evolving power spectra of laser at different simulation times. The results in a) and b) show the spectra obtained when the simulation time is set to $0.1\ ps$*. Whereas, figures c) and d) illustrate the spectra results for a simulation of* $1\ ps$ *depicting the dominant mode.*

The output results, presented in Figure 19, depict a series of narrow, evenly spaced modes oscillating within the loop. These modes maintain a fixed phase relationship, resulting in the power spectrum shown in part b of Figure 19. This spectrum represents the frequency comb characteristic of a mode-locked laser, highlighting the coherence and regularity achieved through the oscillation dynamics.

2.7 Results and Discussions

This chapter examines the applicability of the time-delay oscillator model, developed for optoelectronic oscillators[32], to laser systems using the Simulink platform. The model focuses on explaining the dynamical behaviour and the build-up of oscillations within the resonator cavity under various initial conditions, such as noise or Bessel-mode conditions. The functionality of the laser device is represented through subsystems, with each block discussed in detail. The cavity round trip time, mentioned in the delay block is set to $35.7\ ps$, which corresponds to the characteristic parameter obtained for QDash device during experimental analysis, as described in Section 5.4. Other device parameters, including the cavity length $(1500\ \mu m)$ and pulse repetition rate $(28\ GHz)$, are consistent with the values discussed in Table 6. The simulation time is set to $1\ ps$. The outcomes of these simulations are illustrated in Figure 16-20.

CHAPTER 3

Numerical Modelling of Quantum Well and Quantum Dot Lasers

3.1 Time-Domain Travelling Wave Model

Building on the need for time-domain models and the insights discussed in the previous chapter, this chapter furthers the objective of extending our understanding of the complex processes occurring within the laser cavity. The mode-locking mechanism, as previously described, is a combination of various physical processes like gain, saturable absorption, modulation and dispersion[37]. As light waves propagate within the cavity, the short-duration pulses of the order of picoseconds or femtoseconds experience amplification. This process in a laser amplifier is known to cause distortion and spectral broadening due to a non-linear phenomenon known as self-phase modulation[27]. The physical process responsible for self-phase modulation is gain saturation. The changes in the carrier density cause variations in the intensity which further causes variations in the refractive index as it is the function of intensity. These complex mechanisms make theoretical modelling important for better understanding the dynamics of light waves in a laser. Therefore, some models like Time-Domain Travelling Wave (TDTW) as explained by Agrawal in [27], [38] and Delay Differential Equations (DDE) model proposed by Vladimirov attached in reference[22] will be discussed in detail in this chapter.

TDTW model is an important theoretical computational method used to understand the dynamic properties of physical processes like gain, saturable absorption, modulation and dispersion in semiconductor lasers[37]. It is a useful tool to analyze, simulate and comprehend the complex dynamics of mode-locking phenomenon, to visualize the various causes of distortion and spectral

broadening due to self-phase modulation[27] such that measures can be developed to reduce the effect of distortion and broadening on the laser's gain.

The TDTW model considers the time-varying effect of changes in the refractive index, which is accounted for as susceptibility, changes in the carrier density, the impact of linewidth broadening[39], the transverse distribution of modes along the dimensions of the active region (confinement factor), and differential gain in a semiconductor mode-locked laser[27]. The final expression for the TDTW model, considering the propagation of electromagnetic waves inside the cavity is achieved by solving Maxwell's equations in the spatial and temporal domain along the length of the laser cavity. The model considers the 'slowly-varying envelope approximations' to capture the travelling wave nature of light. The travelling wave equations are coupled with the carrier rate equations, giving insights into the time and space domain variations of the carrier concentrations in the active medium. The spatial resolution of the complex envelope of electric field across the cavity length allows the modelling of spatial hole burning and inhomogeneous broadening effects.

This model is also used to characterize intricate structures such as Quantum Well and Quantum dot material lasers, where the spatial inhomogeneities and carrier dynamics have a substantial impact on the performance of the laser, as discussed in reference[5].

TDTW model is then further extended to the Delay Differential Equation model which is based on the reference formulated by Vladimirov [22] and is discussed in detail in the next section of this chapter.

In the paper [27], the expression for the propagation of light waves inside the cavity is described as-

$$\nabla^2 E - \frac{\epsilon}{c^2}\frac{\partial^2 E}{\partial t^2} = 0 \tag{3.1.1}$$

where $\nabla^2 = \left[\frac{\partial^2}{\partial x^2} + \frac{\partial^2}{\partial y^2} + \frac{\partial^2}{\partial z^2}\right]$, ϵ is the dielectric constant and c is the velocity of light.

The dielectric constant ϵ can be described as:

$$\epsilon = n^2 + \chi \tag{3.1.2}$$

Here, n is the refractive index which is a function of the transverse plane x & y and χ is the susceptibility which is the function of the linewidth enhancement factor (α), effective mode index $(\bar{n})$, and carrier density (N) in the active region of the laser amplifier.

$$\chi = -\frac{\bar{n}c}{\omega_0}(\alpha + i)\, g(N - N_0)$$

$$= -i\left(\frac{\bar{n}c}{\omega_0}\right)(1 - i\alpha)\, g(N - N_0) \tag{3.1.3}$$

where $\bar{n}$ represents the effective mode index, c is the speed of light, α is the Henry's linewidth enhancement factor, g is the differential gain, N is the carrier density and N_0 is the carrier density required to achieve transparency.

From equation (3.1.2), equation (3.1.1) can be modified as:

$$\nabla^2 E - \frac{n^2}{c^2}\frac{\partial^2 E}{\partial t^2} = \chi \frac{1}{c^2}\frac{\partial^2 E}{\partial t^2} \tag{3.1.4}$$

Initially, setting $\chi = 0$ for the device to act as a passive waveguide. In this case, equation (3.1.4) becomes:

$$\nabla^2 E - \frac{n^2}{c^2}\frac{\partial^2 E}{\partial t^2} = 0 \tag{3.1.5}$$

Since the refractive index is the function of (x, y), the trial solution of the form:

$$E(x, y, z, t) = F(x, y; \omega)U(z, t) \tag{3.1.6}$$

where,

$$U(z, t) = e^{i(k(\omega)z - \omega t)} \tag{3.1.7}$$

and $F(x, y; \omega)$ signifies the mode-distribution along the x and y plane of the waveguide as a function of frequency ω.

After applying the appropriate boundary conditions, equation (3.1.6) becomes an eigenfunction-eigen value problem for the waveguide modes due to the transverse variation of the refractive index.

After double differentiating the product rule of differentiation, the expression becomes:

$$\frac{\partial^2}{\partial x^2}(FU) = \frac{\partial}{\partial x}\left(\left(\frac{\partial F}{\partial x}\right)U + F\left(\frac{\partial U}{\partial x}\right)\right) = \left(\frac{\partial^2 F}{\partial x^2}\right)U + 2\left(\frac{\partial F}{\partial x}\right)\left(\frac{\partial U}{\partial x}\right) + F\left(\frac{\partial^2 U}{\partial x^2}\right)$$

The second derivatives are:

$$\frac{\partial^2}{\partial x^2}(FU) = \left(\frac{\partial^2 F}{\partial x^2}\right)U + 2\left(\frac{\partial F}{\partial x}\right)\left(\frac{\partial U}{\partial x}\right) + F\left(\frac{\partial^2 U}{\partial x^2}\right) \tag{a}$$

$$\frac{\partial^2}{\partial y^2}(FU) = \left(\frac{\partial^2 F}{\partial y^2}\right)U + 2\left(\frac{\partial F}{\partial y}\right)\left(\frac{\partial U}{\partial y}\right) + F\left(\frac{\partial^2 U}{\partial y^2}\right) \tag{b}$$

$$\frac{\partial^2}{\partial z^2}(FU) = \left(\frac{\partial^2 F}{\partial z^2}\right)U + 2\left(\frac{\partial F}{\partial z}\right)\left(\frac{\partial U}{\partial z}\right) + F\left(\frac{\partial^2 U}{\partial z^2}\right) \quad (c)$$

$$\frac{\partial^2}{\partial t^2}(FU) = \left(\frac{\partial^2 F}{\partial t^2}\right)U + 2\left(\frac{\partial F}{\partial t}\right)\left(\frac{\partial U}{\partial t}\right) + F\left(\frac{\partial^2 U}{\partial t^2}\right) \quad (d)$$

Since $F = func(x, y; \omega)$ and $U = func(z, t)$, some of the expressions are reduced as:

$$\frac{\partial F}{\partial z} = 0 \quad ; \quad \frac{\partial F}{\partial t} = 0 \quad ; \quad \frac{\partial U}{\partial x} = 0 \quad ; \quad \frac{\partial U}{\partial y} = 0$$

The second derivatives are reduced to:

$$\frac{\partial^2}{\partial x^2}(FU) = \left(\frac{\partial^2 F}{\partial x^2}\right)U \quad (3.1.8)$$

$$\frac{\partial^2}{\partial y^2}(FU) = \left(\frac{\partial^2 F}{\partial y^2}\right)U \quad (3.1.9)$$

$$\frac{\partial^2}{\partial z^2}(FU) = F\left(\frac{\partial^2 U}{\partial z^2}\right) \quad (3.1.10)$$

$$\frac{\partial^2}{\partial t^2}(FU) = F\left(\frac{\partial^2 U}{\partial t^2}\right) \quad (3.1.11)$$

Substituting equations (3.1.8)-(3.1.11) in equation (3.1.5):

$$\left(\frac{\partial^2 F}{\partial x^2} + \frac{\partial^2 F}{\partial y^2}\right)U + F\left(\frac{\partial^2 U}{\partial z^2} - \frac{n^2}{c^2}\frac{\partial^2 U}{\partial^2 t}\right) = 0 \quad (3.1.12)$$

$\frac{\partial^2 U}{\partial z^2} = (ik)^2 e^{i(k(\omega)z - \omega t)} = -k^2 e^{i(k(\omega)z - \omega t)}$ and

$$\frac{\partial^2 U}{\partial t^2} = (-i\omega)^2 e^{i(k(\omega)z - \omega t)} = -\omega^2 e^{i(k(\omega)z - \omega t)}$$

Substituting the above values in equation (3.1.12)

$$\left(\frac{\partial^2 F}{\partial x^2} + \frac{\partial^2 F}{\partial y^2}\right)e^{i(k(\omega)z - \omega t)} + F\left(\omega^2\frac{n^2}{c^2} - k^2\right)e^{i(k(\omega)z - \omega t)} = 0$$

$$\left(\frac{\partial^2 F}{\partial x^2} + \frac{\partial^2 F}{\partial y^2}\right) + F\left(\omega^2\frac{n^2}{c^2} - k^2\right) = 0 \quad (3.1.13)$$

Infinitely many eigenfunctions can be made orthonormal (meaning they are both independent and normalized). The eigenvalues of such eigenfunctions depend on both the frequency (ω) and wave number (k). For each mode, ω is a function of k. All these eigenfunctions form a complete set together, which depicts that any change in the field in the transverse plane can be approximated by combining these eigenfunctions. The coefficients of this combination can be found by multiplying the field with the complex conjugate of the orthonormal eigenfunction and integrating it over the entire transverse plane. Usually, the fundamental mode makes an important contribution to the modal expansion. The eigenfunctions depend slightly on changes in (ω, k) when the deviations from the operating values are small. Hence, we continue to use the function F for values of (ω, k) which are close enough to (ω_0, k_0).

Equation (3.1.6) describes a wave behaviour in terms of an eigenfunction-eigenvalue problem. An eigenfunction F_v is a specific solution to the problem with eigenvalue k_v^2. Both eigenfunction and eigenvalue are a function of frequency ω. The eigenvalue indicates the mode's propagation constant. On the other hand, boundary conditions decide whether the modes are localized, i.e. confined within the waveguide, or have continuous solutions. The eigenfunctions form a complete basis of solutions which means the square-integrable function i.e. a function with a finite energy in the plane (x, y) can be expressed as a summation of these eigenfunctions. The modes can propagate in the forward or backward direction. The sign of the square root of the eigenvalue k_v^2 depicts the direction of propagation. The temporal pulse can be described as a wave packet that combines many eigenfunctions with different eigenvalues and frequencies.

$$E_v(x, y, z, t) = \int_{-\infty}^{\infty} F_v(x, y; \omega)\hat{\mathrm{A}}(\omega)\, e^{(i(k_v(\omega)z - \omega t)}\, d\omega \tag{3.1.14}$$

where $k_v(\omega)$ is the branch of the dispersion relation associated with the mode indexed by v. Assuming a narrowband wave packet $\hat{A}_v(\omega)$, is concentrated on a nominal operating frequency ω_0, which permits a Taylor series approximation up to the first order of dispersion relation $k_v(\omega)$ about ω_0:

$$k_v(\omega) \sim k_v(\omega_0) + \left.\frac{\partial k_v}{\partial \omega_0}\right|_{\omega=\omega_0} \tag{3.1.15}$$

The mode profile F_v is weakly dependent upon ω and consequently may be approximated by:

$$F_v(x, y; \omega) \sim F_v(x, y; \omega_0) \tag{3.1.16}$$

The equation (3.1.14) when taken out of the integral becomes:

$$E_v(x, y, z, t) = F_v(x, y; \omega_0) A_v(z, t) e^{(i(k_v(\omega_0)z - \omega_0 t)} \tag{3.1.17}$$

where A_v is the slowly varying envelope function whose Fourier transform is described by $\widehat{\mathrm{A}}_v$. If A_v is a constant, then $\widehat{\mathrm{A}}_v$ becomes the Dirac delta function depicting the spectral line of infinitesimal width. However, if A_v is time-varying, its spectrum widens, and A_v turns into a wave packet. A wave packet is a combination of many plane waves spread over a narrow range of frequencies for a slowly varying envelope. The integration shows the distribution of plane waves in a wave packet across different frequencies.

The inverse Fourier transform for $A_v(z,t)$ is given as:

$$A_v(z,t) = \int_{-\infty}^{\infty} \widehat{\mathrm{A}}_v(\omega_0 + \delta\omega)\, e^{\left(i\left(\frac{\partial k_v(\omega_0)}{\partial \omega_0} z - t\right)\delta\omega\right)}\, d(\delta\omega) \tag{3.1.18}$$

where $\delta\omega = \omega - \omega_0$, The pure carrier in equation (3.1.17) propagates at the phase velocity which is given by the relation:

$$v_p = \frac{\omega_0}{k_v(\omega_0)} \quad or \quad \left(\frac{k_v(\omega_0)}{\omega_0}\right)^{-1} \tag{3.1.19}$$

Since equation (3.1.18) contains the envelope that is propagating at the group velocity given by the relation:

$$v_{g,v} = \left(\frac{\partial k_v(\omega_0)}{\partial \omega}\right)^{-1} \tag{3.1.20}$$

Hence, A_v is a solution of the free advection equation:

$$\left(\frac{\partial}{\partial z} + \frac{1}{v_{g,v}}\frac{\partial}{\partial t}\right) A_v = 0 \tag{3.1.21}$$

The group velocity is different for different modes. Thus, the inter-modal dispersion causes spreading in an initial pulse which is primarily due to the superposition of modes. The dispersion due to waveguide structure is also included using the dispersion relation. The effect due to material dispersion could also be accounted but it is usually small and hence is neglected for simplicity purposes.

Setting:

$E = A(z,t)V$ where $V = F_v(x,y;\omega)e^{i(k_0 z - \omega_0 t)}$ and k_0 accounts for $k_0 = k_v(\omega_0)$ (3.1.22)

By integrating equations (3.1.8) to (3.1.11) into equation (3.1.4), the left-hand side of the equation is simplified as:

$$\nabla^2 E - \frac{n^2}{c^2}\frac{\partial^2 E}{\partial t^2} = A\left(\frac{\partial^2}{\partial x^2} + \frac{\partial^2}{\partial y^2}\right)V + \frac{\partial^2}{\partial z^2}(AV) - \frac{n^2}{c^2}\frac{\partial^2}{\partial t^2}(AV) \tag{3.1.23}$$

From equations (c) and (d), the above equation can be written as:

$$\nabla^2 E - \frac{n^2}{c^2}\frac{\partial^2 E}{\partial t^2} = A\left(\frac{\partial^2}{\partial x^2} + \frac{\partial^2}{\partial y^2}\right)V + \frac{\partial^2 A}{\partial z^2}V + 2\frac{\partial A}{\partial z}\frac{\partial V}{\partial z} + A\frac{\partial^2 V}{\partial z^2} - \frac{n^2}{c^2}\left(\frac{\partial^2 A}{\partial t^2}V + 2\frac{\partial A}{\partial t}\frac{\partial V}{\partial t} + A\frac{\partial^2 V}{\partial t^2}\right)$$
$$= A\left[\left(\frac{\partial^2}{\partial x^2} + \frac{\partial^2}{\partial y^2} + \frac{\partial^2}{\partial z^2}\right)V - \frac{n^2}{c^2}\frac{\partial^2 V}{\partial t^2}\right] + \left(\frac{\partial^2 A}{\partial z^2}V + 2\frac{\partial A}{\partial z}\frac{\partial V}{\partial z}\right) - \frac{n^2}{c^2}\left(\frac{\partial^2 A}{\partial t^2}V + 2\frac{\partial A}{\partial t}\frac{\partial V}{\partial t}\right)$$

From equation (3.1.13), the first term in the above expression equates to 0 i.e.

$$\left(\frac{\partial^2}{\partial x^2} + \frac{\partial^2}{\partial y^2} + \frac{\partial^2}{\partial z^2}\right)V - \frac{n^2}{c^2}\frac{\partial^2 V}{\partial t^2} = 0$$

The expression is modified as:

$$\nabla^2 E - \frac{n^2}{c^2}\frac{\partial^2 E}{\partial t^2} = \left(\frac{\partial^2 A}{\partial z^2}V + 2\frac{\partial A}{\partial z}\frac{\partial V}{\partial z}\right) - \frac{n^2}{c^2}\left(\frac{\partial^2 A}{\partial t^2}V + 2\frac{\partial A}{\partial t}\frac{\partial V}{\partial t}\right)$$

The above expression can be reduced as:

$$\frac{\partial V}{\partial t} = F_v(x, y; \omega)\frac{\partial e^{i(k_0 z - \omega_0 t)}}{\partial t} + e^{i(k_0 z - \omega_0 t)}\frac{\partial F_v(x, y; \omega)}{\partial t}$$

Since,

$$\frac{\partial F_v(x, y; \omega)}{\partial t} = 0$$

$$\frac{\partial V}{\partial t} = -i\omega_0 F_v(x, y; \omega)e^{i(k_0 z - \omega_0 t)} = -i\omega_0 V$$

Similarly, the expression $\frac{\partial V}{\partial z}$ is reduced to become:

$$\frac{\partial V}{\partial z} = ik_0 F_v(x, y; \omega)e^{i(k_0 z - \omega_0 t)} = ik_0 V$$

Therefore, the wave equation is reduced to become:

$$\nabla^2 E - \frac{n^2}{c^2}\frac{\partial^2 E}{\partial t^2} = \left(\frac{\partial^2 A}{\partial z^2}V + 2ik_0\frac{\partial A}{\partial z}V\right) - \frac{n^2}{c^2}\left(\frac{\partial^2 A}{\partial t^2}V + 2i\omega_0\frac{\partial A}{\partial t}V\right)$$

Multiplying the first term for expansion of the left-hand side of the wave equation with k_0^2 and second term with ω_0^2, the overall expression becomes

$$\nabla^2 E - \frac{n^2}{c^2}\frac{\partial^2 E}{\partial t^2} = \left[k_0^2\left(\frac{1}{k_0^2}\frac{\partial^2 A}{\partial z^2} + \frac{2i}{k_0}\frac{\partial A}{\partial z}\right) - \frac{n^2}{c^2}\omega_0^2\left(\frac{1}{\omega_0^2}\frac{\partial^2 A}{\partial t^2} - \frac{2i}{\omega_0}\frac{\partial A}{\partial t}\right)\right]V \qquad (3.1.24)$$

The right side of the wave equation in (3.1.4) can be expanded as:

$$\chi\frac{1}{c^2}\frac{\partial^2 E}{\partial t^2} = \chi\frac{1}{c^2}\left(\frac{\partial^2 A}{\partial t^2}V + 2\frac{\partial A}{\partial t}\frac{\partial V}{\partial t} + A\frac{\partial^2 V}{\partial t^2}\right) \qquad (3.1.25)$$

From equation (3.1.11), the value for $\frac{\partial^2 V}{\partial t^2}$ becomes:

$$\frac{\partial^2 V}{\partial t^2} = \frac{\partial^2 (F_v U)}{\partial t^2} = F_v\frac{\partial^2 U}{\partial t^2} = -\omega_0^2 F_v e^{i(k_0 z - \omega_0 t)} = -\omega_0^2 V$$

Equation (3.1.25) can be reduced in the form:

$$\chi\frac{1}{c^2}\frac{\partial^2 E}{\partial t^2} = \chi\frac{1}{c^2}\left(\frac{\partial^2 A}{\partial t^2}V - 2i\omega_0\frac{\partial A}{\partial t} - \omega_0^2 A\right)V$$

Multiplying the right-hand side of the equation with ω_0^2, the above equation becomes:

$$= \chi\frac{\omega_0^2}{c^2}\left(\frac{1}{\omega_0^2}\frac{\partial^2 A}{\partial t^2}V - \frac{2i}{\omega_0}\frac{\partial A}{\partial t} - A\right)V \qquad (3.1.26)$$

Substituting equations (3.1.24) and (3.1.26) into the original equation (3.1.4):

$$k_0^2\left(\frac{1}{k_0^2}\frac{\partial^2 A}{\partial z^2} + \frac{2i}{k_0}\frac{\partial A}{\partial z}\right) - \frac{n^2}{c^2}\omega_0^2\left(\frac{1}{\omega_0^2}\frac{\partial^2 A}{\partial t^2} - \frac{2i}{\omega_0}\frac{\partial A}{\partial t}\right) = \chi\frac{\omega_0^2}{c^2}\left(\frac{1}{\omega_0^2}\frac{\partial^2 A}{\partial t^2}V - \frac{2i}{\omega_0}\frac{\partial A}{\partial t} - A\right) \qquad (3.1.27)$$

The complex envelope A containing the different modes is assumed to be slowly varying which means that the second-order terms in equation (3.1.27) would be neglected and the slowly varying envelope moves contain the spatial period as $\delta z = 2\pi/k_0$ and the temporal period is $\delta t = 2\pi/\omega_0$. Hence, the final term is dominant for each of the brackets in above equation:

$$2ik_0\frac{\partial A}{\partial z} + 2i\omega_0\frac{n^2}{c^2}\frac{\partial A}{\partial t} = -\chi\frac{\omega_0^2}{c^2}A \qquad (3.1.28)$$

The effective index of the guided mode can be approximated as:

$$\frac{\partial A}{\partial z} + \frac{\omega_0}{k_0}\frac{n^2}{c^2}\frac{\partial A}{\partial t} = \chi\frac{i}{2k_0}\frac{\omega_0^2}{c^2}A \qquad (3.1.29)$$

$$\because \qquad k_0 = \frac{\bar{n}\omega_0}{c}$$

The equation (3.1.29) becomes:

$$\frac{\partial A}{\partial z} + n^2 \frac{1}{\bar{n}c}\frac{\partial A}{\partial t} = \chi \frac{i\omega_0}{2\bar{n}c} A \tag{3.1.30}$$

Both sides are the summation of all the modes. The orthogonality is invoked by multiplying the sums through the complex conjugate of the field profile of the mode of interest and integrating over the whole transverse plane, we get:

$$\frac{\partial A}{\partial z} + \frac{1}{\bar{n}c}\left(\int_{-\infty}^{\infty}\int_{-\infty}^{\infty} F_v^* F_v \, n^2 dxdy\right)\frac{\partial A}{\partial t} = \frac{1}{2} i \left(\frac{\omega_0}{\bar{n}c}\right)\left(\int_{-\infty}^{\infty}\int_{-\infty}^{\infty} F_v^* F_v \chi dxdy\right) A$$

$$\frac{\partial A}{\partial z} + \frac{1}{\bar{n}c}\left(\int_{-\infty}^{\infty}\int_{-\infty}^{\infty} |F_v|^2 \, n^2 dxdy\right)\frac{\partial A}{\partial t} = \frac{1}{2} i \left(\frac{\omega_0}{\bar{n}c}\right)\left(\int_{-\infty}^{\infty}\int_{-\infty}^{\infty} |F_v|^2 \chi dxdy\right) A \tag{3.1.31}$$

Noting that $\chi \cong 0$ outside the active region, the confinement factor is introduced to represent the extent to which the modes are confined within the dimensions of the active region. w and d represents the width and thickness of the active region. The right side of equation (3.1.31) can be modified as:

$$\frac{\partial A}{\partial z} + \frac{1}{\bar{n}c}\left(\int_{-\infty}^{\infty}\int_{-\infty}^{\infty} |F_v|^2 \, n^2 dxdy\right)\frac{\partial A}{\partial t} = \frac{1}{2} i \left(\frac{\omega_0}{\bar{n}c}\right)\chi\left(\int_{-w/2}^{w/2}\int_{-d/2}^{d/2} |F_v|^2 dxdy\right) A \tag{3.1.32}$$

Dividing the above equation by the factor of $\int_{-\infty}^{\infty}\int_{-\infty}^{\infty}|F_v|^2 dxdy$, the above equation is written as:

$$\frac{1}{\int_{-\infty}^{\infty}\int_{-\infty}^{\infty}|F_v|^2 dxdy}\frac{\partial A}{\partial z} + \frac{1}{\bar{n}c}\left(\frac{\int_{-\infty}^{\infty}\int_{-\infty}^{\infty}|F_v|^2 \, n^2 dxdy}{\int_{-\infty}^{\infty}\int_{-\infty}^{\infty}|F_v|^2 dxdy}\right)\frac{\partial A}{\partial t} = \frac{1}{2} i \left(\frac{\omega_0}{\bar{n}c}\right)\chi\left(\frac{\int_{-w/2}^{w/2}\int_{-d/2}^{d/2}|F_v|^2 dxdy}{\int_{-\infty}^{\infty}\int_{-\infty}^{\infty}|F_v|^2 dxdy}\right) A \tag{3.1.33}$$

The term $|F_v|^2$ is assumed to be normalized such that:

$$\int_{-\infty}^{\infty}\int_{-\infty}^{\infty}|F_v|^2 dxdy = 1 \tag{3.1.34}$$

The above equation becomes

$$\frac{\partial A}{\partial z} + \frac{n_g}{c}\frac{\partial A}{\partial t} = \frac{1}{2} i\Gamma \left(\frac{\omega_0}{\bar{n}c}\right)\chi A \tag{3.1.35}$$

where confinement factor, Γ is defined as:

$$\Gamma = \frac{\int_{-w/2}^{w/2}\int_{-d/2}^{d/2}|F_v|^2 dxdy}{\int_{-\infty}^{\infty}\int_{-\infty}^{\infty}|F_v|^2 dxdy} \tag{3.1.36}$$

and n_g represents the group index defined as:

$$n_g = \frac{1}{\bar{n}}\frac{\int_{-\infty}^{\infty}\int_{-\infty}^{\infty} n^2|F_v|^2 dxdy}{\int_{-\infty}^{\infty}\int_{-\infty}^{\infty}|F_v|^2 dxdy} \tag{3.1.37}$$

The term c/n_g introduces the group velocity v_g in the Time-Domain Travelling Wave expression.

Using the expression for χ in equation (3.1.35), the expression can be reduced to a form:

$$\frac{\partial A}{\partial z} + \frac{1}{v_g}\frac{\partial A}{\partial t} = -\frac{1}{2} i\Gamma\left(\frac{\omega_0}{\bar{n}c}\right) i\left(\frac{\bar{n}c}{\omega_0}\right)(1 - i\alpha)\, g(N - N_0)A$$

$$\boldsymbol{\frac{\partial A}{\partial z} + \frac{1}{v_g}\frac{\partial A}{\partial t} = \frac{1}{2}\Gamma(1 - i\alpha)\, g(N - N_0)\, A} \tag{3.1.38}$$

According to the charge neutrality, the electron density in the active region is same as the hole density. For simplicity, our analysis is focused on the electron density (N). The carrier density rate equation is crucial in understanding the temporal variation in the number of carriers (electrons) within the active region. This variation is governed by the electrons introduced into the active region through the injection current and the carriers lost due to the radiative and non-radiative recombination processes.

The rate equation for electron density as given in the reference [27] is written as:

$$\frac{\partial N}{\partial t} = D\nabla^2 N + \frac{I}{qV} - \frac{N}{\tau_c} - \frac{g(N - N_0)}{\hbar\omega_0}|E|^2 \tag{3.1.39}$$

where,

N is the electron density

N_0 is the electron density required for transparency

D is the diffusion coefficient

I is the injection current

V is the volume of the active region

τ_c is the spontaneous carrier's lifetime

$\hbar\omega_0$ is the photon energy

g is the gain coefficient

$|E|^2$ is the local electric field strength

The term containing the diffusion constant is neglected under the assumption of charges being uniformly distributed over the transverse direction of the active region.

Hence, the equation (3.1.39) can be written as:

$$\frac{\partial N}{\partial t} = \frac{I}{qV} - \frac{N}{\tau_c} - \frac{g(N - N_0)}{\hbar\omega_0}|E|^2 \tag{3.1.40}$$

Similar to the carrier density rate equation, it is important to analyze the rate of photon generation by net stimulated recombination and the loss of photons within the resonant cavity. This behaviour is described by the photon density rate equation which is expressed as[40]:

$$\frac{\partial P}{\partial t} = R_{sp} + g\Gamma v_g(N - N_0)P - \frac{P}{\tau_p} \tag{3.1.41}$$

where,

P denotes the photon density.

R_{sp} represents the net photon generated due to the spontaneous emission rate.

v_g is the group velocity.

g is the differential gain

Γ is the confinement factor

N is the injected carrier (electron) density

N_0 is the carrier (electron) density required to achieve transparency

τ_p represents the photon lifetime.

The net generated photons due to the spontaneous emission rate are much less than the stimulated emission rate. Thus, the term R_{sp} can be neglected which reduces the equation (3.1.40) to:

$$\frac{\partial P}{\partial t} = g\Gamma v_g(N - N_0)P - \frac{P}{\tau_p} \tag{3.1.42}$$

According to the conservation of charges in the time-domain travelling wave model, the net stimulated photon emission must equal the net stimulated electron-hole recombination. The continuity equation for electron density as explained in the section 4.3.2 Continuity Equations is given as:

$$\frac{\partial N}{\partial t} - \frac{1}{q}\nabla \cdot \boldsymbol{J}_N = G_N - R_N; \quad \boldsymbol{J}_N = qNv_g\boldsymbol{e_z} \tag{3.1.43}$$

Similarly, the continuity equation for photon density becomes:

$$\frac{\partial P}{\partial t} + \nabla \cdot \boldsymbol{J}_P = \left.\frac{\partial P}{\partial t}\right|_{net} \quad ; \quad \boldsymbol{J}_P = qPv_g\boldsymbol{e_z} \tag{3.1.44}$$

where, N and P are the electron and photon densities respectively, G_N & R_N denotes the generation and recombination rates of electrons, J_N & J_P represents the electron current density and photon current density, v_g is the group velocity, $\boldsymbol{e_z}$ is the unit vector for the laser axis, $\frac{\partial P}{\partial t}$ is the rate of net generated photons due to stimulated emission. The minus sign in equation (3.1.43) indicates the charge of an electron.

The source-free travelling wave equation for $|A|^2$ is consequently a statement of conservation of photon density. Hence, by equating the LHS of equation (3.1.43) with RHS of (3.1.44), the carrier rate equation becomes:

$$\frac{\partial N}{\partial t} = qNv_g - \frac{N}{\tau_c} - g\Gamma v_g(N - N_0)|A|^2 \tag{3.1.45}$$

Solving the equation further yields the following result:

$$\boldsymbol{\frac{\partial N}{\partial t} = J - \frac{N}{\tau_c} - g\Gamma v_g(N - N_0)|A|^2} \tag{3.1.46}$$

where:

τ_C is the carrier lifetime (the inverse of carrier density relaxation rate) which is considered equal to τ_p.

$J = qNv_g$ is the current density which is obtained by comparing the units of the equations

$|A|^2$ is taken to represent the local photon number density P:

$$P = |A|^2 \tag{3.1.47}$$

The field power $\mathcal{P}$ is then given by:

$$\mathcal{P} = \sigma v_g \hbar\omega_0 |A|^2 \tag{3.1.48}$$

where σ is the cross-sectional area of the active region, v_g is the group velocity, $\hbar\omega_0$ denotes the photon energy, A is the slowly varying complex envelope.

In summary, the time domain travelling wave model is defined by:

$$\left(\frac{\partial}{\partial z} + \frac{1}{v_g}\frac{\partial}{\partial t}\right) A = \frac{1}{2} g\Gamma(1 - i\alpha_H)(N - N_0)A$$

$$\frac{\partial N}{\partial t} = J - \frac{N}{\tau_c} - v_g g\Gamma(N - N_0)|A|^2$$

3.2 Delay Differential Equation Model for Passive Mode Locking of Semiconductor lasers

The Delay Differential Equation (DDE) model, also known as the non-linear integro-differential equations, proposed by Vladimirov[22], provides a theoretical framework for understanding passive mode-locked semiconductor lasers. Some of the earliest models of mode-locking theory were introduced by New [30] and Haus [31]. Haus' theory, based on the master equation[41], differs from New's theory by incorporating physical phenomena, such as dispersion, along with other assumptions and approximations. Haus's model considers that the relaxation time of the saturable absorber is longer than the pulse duration, a condition known as 'slow absorber'. In contrast, New's model assumes that the absorber's relaxation time is shorter than the pulse duration. Haus incorporates several assumptions and approximations, including homogeneous broadening in the active medium, the effects of bandwidth limitation on gain requirements, and the absence of pulse broadening in the gain and absorber media.

The impact of spectral filtering or dispersion is accounted for in Haus model by introducing a passive linear element. It is known that the constraint in bandwidth causes pulse broadening in time domain[26], which leads to some changes in the gain requirements. Haus describes the spectral filtering coefficient by using parabolic approximation. In another approximation of weak

saturation in the absorber, Haus describes the pulse shape as a hyperbolic secant, suggesting that the pulse's amplitude decreases exponentially rather than the trailing edge of the Gaussian curve, as the pulse moves away from its center.

Despite the differences, both models share the common approximation of a small trip time through the gain and absorber media. These models were effective for solid-state dye laser systems, however, they failed to model the dynamics of semiconductor lasers[24],[26],[42]. In contrast, Vladimirov's proposed model is based on passive mode-locking in semiconductor Quantum Well lasers and does not consider the assumptions of weak absorber saturation and small trip time across the gain and absorber media. Vladimirov's approach to employ a spectral filter[43] is analogous to the dispersive medium used by Haus. The unidirectional ring-shaped cavity is the major assumption in Vladimirov's model [22]. This model was further extended to describe the dynamic properties in Quantum dot mode-locked lasers [5]. These dynamics, as discussed in [5], are based on the capture and escape processes (discussed in detail in Section C) of Literature Review) in quantum dot structures.

This section describes Vladimirov's Delay Differential Equation model of passive mode-locked semiconductor lasers, following the analysis presented in reference [22]. The passive mode-locking is a powerful mechanism to obtain ultra-short pulses for various applications requiring optical temporal or frequency comb generators such as time-domain multiplexing[44]; dense wavelength division multiplexing (DWDM) [45], advanced modulation schemes such as Nyquist pulse generation & orthogonal frequency division multiplexing (OFDM); and, ultra-low phase noise microwave sources [43],[46],[47]. In a passive mode-locked laser, a saturable absorber is placed within the cavity in addition to the active gain medium. The absorber saturates faster than the amplifying medium, creating a small temporal window with a net gain to compensate for the losses experienced by the pulses in the cavity and hence sustain the locking regime. In cases where the relaxation time of the absorber is larger than the pulse duration, the absorber is referred to as a "slow absorber"[1],[31].

It is convenient to construct a model of a ring laser (see Figure 20) with propagation in the cavity assumed unidirectional for simplicity. Nevertheless, the ring laser model is found to apply to mode-locking phenomena in Fabry-Perot semiconductor lasers which support forward, and backward propagating modes provided the effects of pulse collision within active regions may be neglected. The model contains a spectral filter which describes the gain profile combined with the transmission of any frequency-selective components placed within the cavity. The spectral filter is often assumed to have a Lorentzian power transmission function although that is not a necessary assumption.

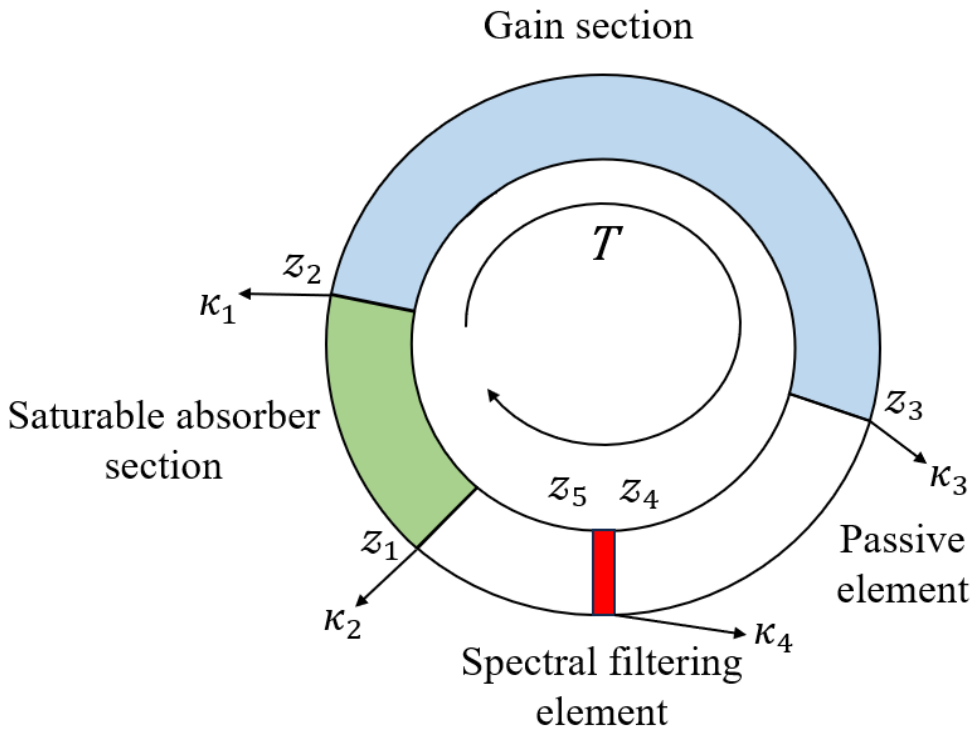

Figure 20: Image illustrating ring-shaped laser model.
Source: Reproduced from the reference [49].

Figure 20 is a schematic of a ring laser and uses a lumped element approach to include gain, saturable absorber, spectral filtering elements and non-resonant losses. The coordinate z is considered along the laser axis and is the direction of propagation of longitudinal laser modes. The laser cavity is divided into three segments, the segment between $(z_1 < z < z_2)$ comprises the absorber material, the segment between $(z_2 < z < z_3)$ contains the active medium, the spectral filter is located between $(z_4 < z < z_5)$ and the remaining regions between $(z_3 < z < z_4)$ and $(z_5 < z < z_1 + L)$ are passive sections. The evolution of the complex envelope of a travelling electromagnetic wave in the amplifying and absorbing segments can be described by the following partial differential equations (as discussed in detail in the previous section):

$$\frac{\partial E(t,z)}{\partial z} + \frac{1}{v_g}\frac{\partial E(t,z)}{\partial t} = \frac{g_G \Gamma_G}{2}(1 - i\alpha_G)\left[N_G(t,z) - N_{0,G}\right] E(t,z) \qquad (3.2.1a)$$

$$\frac{\partial E(t,z)}{\partial z} + \frac{1}{v_g}\frac{\partial E(t,z)}{\partial t} = \frac{g_Q \Gamma_Q}{2}(1 - i\alpha_Q)\left[N_Q(t,z) - N_{0,Q}\right] E(t,z) \qquad (3.2.1b)$$

$$\frac{\partial N_G(t,z)}{\partial t} = J - \frac{N_G(t,z)}{\tau_G} - v_g g_G \Gamma_G \left[N_G(t,z) - N_{0,G}\right] |E(t,z)|^2 \qquad (3.2.2a)$$

$$\frac{\partial N_Q(t,z)}{\partial t} = -\frac{N_Q(t,z)}{\tau_Q} - v_g g_Q \Gamma_Q \left[N_Q(t,z) - N_{0,Q}\right] |E(t,z)|^2 \qquad (3.2.2a)$$

G subscript signifies the gain amplifying medium and Q depicts the absorbing medium.

$E(t,z)$ is the complex envelope of the electric field.

N is the carrier density.

N_0 is the carrier density at transparency, the parameter is a function of material.

v_g is the group velocity.

Γ is the confinement factor which describes transverse modal confinement.

g is the differential gain which is a function of material.

α is the linewidth enhancement factor which models the carrier-induced refractive index changes.

τ is the carrier lifetime, and the inverse is defined as the carrier lifetime relaxation rate.

$J = Iq/\sigma$ is the injection current density with σ as the cross-sectional area of the active region.

The factor $|E(t,z)|^2$ describes the photon density.

Since the passive section has no carriers ($N = N_0$) hence, the right side of equation (3.2.1) becomes 0 and the electric field amplitude in the passive segments is governed by the relation:

$$\frac{\partial E(t,z)}{\partial z} + \frac{1}{v_g}\frac{\partial E(t,z)}{\partial t} = 0 \qquad (3.2.3)$$

The last segment is the spectral filter ($z_4 < z < z_5$) that is assumed to be infinitely thin i.e. $z_4 = z_5$. The purpose of incorporating the spectral filter is to consider the finite bandwidth of gain spectrum. The evolution of electric-field amplitude in this segment in the time domain is described as the convolution function between the incoming electric field and the impulse function of the filter element $f(t)$:

$$E(t,z_5) = f(t) \otimes E(t,z_4) \;\; or$$
$$E(t,z_5) = \int_{-\infty}^{\tau} f(t-\theta)E(\theta,z_4)\, d\theta$$

In the Fourier domain, the above expression becomes:

$$\hat{E}(\omega,z_5) = \hat{f}(\omega)\hat{E}(\omega,z_4) \qquad (3.2.4)$$

here $\hat{E}(\omega, z_4)$ and $\hat{E}(\omega, z_5)$ are the Fourier components of the amplitudes of the electric field $E(t, z_4)$ and $E(t, z_5)$. The component $\hat{f}(\omega)$ specifies the spectral line profile of the filter.

Another assumption made is that the electric-field amplitude in a ring laser satisfies the periodic boundary condition because $z_4 + L = z_5$:

$$E(t, z + L) = E(t, z) \tag{3.2.5}$$

where L is the cavity length.

Introducing the coordinate transformation from $(t, z) \rightarrow (\tau, \zeta)$ to represent the changing of the frame to coordinates moving with the electric field. Here $\tau = t - z/v_g$ is the retarded time. Equation (3.2.1) for amplifying segment becomes:

$$\frac{\partial E(t,z)}{\partial z} + \frac{1}{v_g}\frac{\partial E(t,z)}{\partial t} = \frac{g_G \Gamma_G}{2}(1 - i\alpha_G)\left[N_G(t,z) - N_{0,G}\right] E(t,z)$$

$$\tau(t, z) = t - \frac{z}{v_g} \tag{3.2.6}$$

$$\zeta(t, z) = z \tag{3.2.7}$$

$$A(\tau\,(t, z), \zeta(t, z)) = E(t, z) \tag{3.2.8}$$

From the above expressions:

$$\frac{\partial \tau}{\partial z} = -\frac{1}{v_g} \tag{3.2.9}$$

$$\frac{\partial \tau}{\partial t} = 1 \tag{3.2.10}$$

$$\frac{\partial \zeta}{\partial z} = 1 \tag{3.2.11}$$

$$\frac{\partial \zeta}{\partial t} = 0 \tag{3.2.12}$$

The left side of equation (3.2.1a) with the application of coordinate transformation can be re-written as:

$$\left(\frac{\partial}{\partial z} + \frac{1}{v_g}\frac{\partial}{\partial t}\right) E(t, z) = \left(\frac{\partial \tau}{\partial z}\cdot\frac{\partial}{\partial \tau} + \frac{1}{v_g}\frac{\partial \tau}{\partial t}\cdot\frac{\partial}{\partial \tau} + \frac{\partial \zeta}{\partial z}\cdot\frac{\partial}{\partial \zeta} + \frac{1}{v_g}\frac{\partial \zeta}{\partial t}\cdot\frac{\partial}{\partial \zeta}\right) A \tag{3.2.13}$$

Substituting equations (3.2.9)-(3.2.12) in equation (3.2.13) we get,

$$\left(\frac{\partial}{\partial z}+\frac{1}{v_g}\frac{\partial}{\partial t}\right)E(t,z)=\left(\frac{-1}{v_g}\cdot\frac{\partial}{\partial \tau}+\frac{1}{v_g}\cdot 1\cdot\frac{\partial}{\partial \tau}+1\cdot\frac{\partial}{\partial \zeta}+\frac{1}{v_g}\cdot 0\cdot\frac{\partial}{\partial \zeta}\right)A$$

$$\left(\frac{\partial}{\partial z}+\frac{1}{v_g}\frac{\partial}{\partial t}\right)E(t,z)=\left(\frac{\partial}{\partial \zeta}\right)A(\tau,\zeta) \tag{3.2.14}$$

$$\frac{\partial A(\tau,\zeta)}{\partial z}=\frac{1}{2}(1-i\alpha_G)\,g_G\Gamma_G\left[N_G(t,z)-N_{0,G}\right]A(\tau,\zeta) \tag{3.2.15}$$

Applying the coordinate transformation in the carrier density equation, the modified expression becomes-

$$\frac{\partial N_G(t,z)}{\partial t}=\left[\frac{\partial \tau}{\partial t}\cdot\frac{\partial}{\partial \tau}+\frac{\partial \zeta}{\partial t}\cdot\frac{\partial}{\partial \zeta}\right]N_G(\tau,\zeta)=\left[1\cdot\frac{\partial}{\partial \tau}+0\cdot\frac{\partial}{\partial \zeta}\right]N_G(\tau,\zeta)$$

$$\frac{\partial N_G(t,z)}{\partial t}=\left(\frac{\partial}{\partial \tau}\right)N_G(\tau,\zeta) \tag{3.2.16}$$

$$\frac{\partial N_G(\tau,\zeta)}{\partial \tau}=J-\frac{N_G(\tau,\zeta)}{\tau_G}-v_g g_G\Gamma_G\left[N_G(\tau,\zeta)-N_{0,G}\right]|A(\tau,\zeta)|^2 \tag{3.2.17}$$

Similarly for absorbing medium, the equations become:

$$\frac{\partial A(\tau,\zeta)}{\partial \zeta}=-\frac{1}{2}\left(1-i\alpha_Q\right)g_Q\Gamma_Q\left[N_Q(\tau,\zeta)-N_{0,Q}\right]A(\tau,\zeta) \tag{3.2.18}$$

$$\frac{\partial N_Q(\tau,\zeta)}{\partial \tau}=-\frac{N_Q(\tau,\zeta)}{\tau_Q}-v_g g_Q\Gamma_Q\left[N_Q(\tau,\zeta)-N_{0,Q}\right]|A(\tau,\zeta)|^2 \tag{3.2.19}$$

For the passive elements:

$$\frac{\partial A(\tau,\zeta)}{\partial \zeta}=0 \tag{3.2.20}$$

The transformation of the fields as it passes through the segments of the cavity provided by equations (3.2.16) to (3.2.20) is described in the following sections:

1) **<u>Amplifying segment ($z_2 < z < z_3$):</u>**

Integrating the field equation over the length of the gain amplifying section:

$$\int_{z_2}^{z_3}\frac{\partial A(\tau,\zeta)}{\partial \zeta}\partial\zeta=\frac{1}{2}(1-i\alpha)\int_{z_2}^{z_3}g_G\Gamma_G\left[N_G-N_{0,G}\right]d\zeta\,.A$$

$$\int_{z_2}^{z_3} \frac{1}{A} \frac{\partial A(\tau,\zeta)}{\partial \zeta} \partial\zeta = \frac{1}{2}(1 - i\alpha) \int_{z_2}^{z_3} g_G \Gamma_G \left[N_G - N_{0,G}\right] d\zeta$$

$$\ln A|_{z_2}^{z_3} = \frac{1}{2}(1 - i\alpha) G(\tau)$$

$$[\ln A(z_3,\tau) - \ln A(z_2,\tau)] = \frac{1}{2}(1 - i\alpha) G(\tau)$$

$$\ln\left[\frac{A(\tau,z_3)}{A(\tau,z_2)}\right] = \frac{1}{2}(1 - i\alpha) G(\tau)$$

$$\frac{A(\tau,z_3)}{A(\tau,z_2)} = e^{\left[\frac{1-i\alpha_G}{2} G(\tau)\right]}$$

$$A(\tau,z_3) = e^{\left[\frac{1-i\alpha_G}{2} G(\tau)\right]} A(\tau,z_2) \tag{3.2.21}$$

where:

$$G(\tau) = \int_{z_2}^{z_3} g_G \Gamma_G \left[N_G - N_{0,G}\right] d\zeta = \int_{z_2}^{z_3} n_G \, d\zeta \tag{3.2.22}$$

The term $G(\tau)$ described in equation (3.2.22) represents the overall gain in the amplifying section.

Introducing the term κ_1 which denotes the internal non-resonant attenuation loss occurring at the intersection of the absorber and gain sections due to changes in materials and depends on the length of each of the elements.

The boundary condition of the electric field at the intersection between each element is described as:

$$\boldsymbol{A(\tau, z_3) = \sqrt{\kappa_1} e^{\left[\frac{1-i\alpha_G}{2} G(\tau)\right]} A(\tau, z_2)} \tag{3.2.23}$$

From equation (15):

$$A^* \left(\frac{\partial A(\tau,\zeta)}{\partial \zeta}\right) = \frac{1}{2}(1 - i\alpha_G)\, n_G A A^*$$

$$= \frac{1}{2}(1 - i\alpha_G)\, n_G |A|^2 \tag{3.2.24}$$

$$A\left(\frac{\partial A^*(\tau,\zeta)}{\partial \zeta}\right) = \frac{1}{2}(1 + i\alpha_G)\, n_G A^* A$$

$$= \frac{1}{2}(1 + i\alpha_G)\, n_G |A|^2 \tag{3.2.25}$$

Adding (3.2.23) and (3.2.24), we get

$$\frac{\partial|A|^2}{\partial\zeta} = n_G|A|^2 \tag{3.2.26}$$

Integrating the above equation over the length of the gain section

$$\int_{z_2}^{z_3}\frac{\partial|A|^2}{\partial\zeta} = g_G\Gamma_G\int_{z_2}^{z_3}\left[N_G - N_{0,G}\right]|A|^2 d\zeta$$

$$\Rightarrow \qquad |A(\tau,z_3)|^2 - |A(\tau,z_2)|^2 = g_G\Gamma_G\int_{z_2}^{z_3}\left[N_G - N_{0,G}\right]|A|^2 d\zeta \tag{3.2.27}$$

Differentiating equation (3.2.22) with respect to τ, we get:

$$\frac{\partial G(\tau)}{\partial\tau} = g_G\Gamma_G\int_{z_2}^{z_3}\frac{\partial N_G}{\partial\tau}d\zeta - g_G\Gamma_G\int_{z_2}^{z_3}\frac{\partial N_{0,G}}{\partial\tau}d\zeta$$

$$\therefore \qquad \int_{z_2}^{z_3}\frac{\partial N_{0,G}}{\partial\tau}d\zeta = 0 \ \ as\ N_0\ is\ constant$$

From equation (3.2.17) the above equation can be written as:

$$\frac{\partial G(\tau)}{\partial\tau} = g_G\Gamma_G\int_{z_2}^{z_3}Jd\zeta - g_G\Gamma_G\int_{z_2}^{z_3}\frac{N_G}{\tau_G}d\zeta - g_G\Gamma_G\nu_g\int_{z_2}^{z_3}g_G\Gamma_G\left[N_G - N_{0,G}\right]|A|^2 d\zeta \tag{3.2.28}$$

Expanding the second term on RHS further by adding and subtracting $N_{0,G}$, we get:

$$\int_{z_2}^{z_3}N_G d\zeta = \int_{z_2}^{z_3}(N_G - N_{0,G})d\zeta + \int_{z_2}^{z_3}N_{0,G}d\zeta$$

Multiplying both sides by $g_G\Gamma_G$, the above equation becomes:

$$g_G\Gamma_G\int_{z_2}^{z_3}N_G d\zeta = g_G\Gamma_G\int_{z_2}^{z_3}(N_G - N_{0,G})d\zeta + g_G\Gamma_G\int_{z_2}^{z_3}N_{0,G}d\zeta$$

From equation (3.2.22), we can write:

$$g_G\Gamma_G\int_{z_2}^{z_3}N_G d\zeta = G + g_G\Gamma_G\int_{z_2}^{z_3}N_{0,G}d\zeta$$

Substituting the above expression in equation (3.2.28)

$$\frac{\partial G(\tau)}{\partial \tau} = g_G \Gamma_G \int_{z_2}^{z_3} \left(J - \frac{N_{0,G}}{\tau_G}\right) d\zeta - \frac{G}{\tau_G} - g_G \Gamma_G v_g \int_{z_2}^{z_3} g_G \Gamma_G \left[N_G - N_{0,G}\right] |A|^2 d\zeta$$

From equation (3.2.26), the above equation can be modified as:

$$\frac{\partial G(\tau)}{\partial \tau} = g_G \Gamma_G \int_{z_2}^{z_3} \left(J - \frac{N_{0,G}}{\tau_G}\right) d\zeta - \frac{G}{\tau_G} - g_G \Gamma_G v_g (|A(\tau, z_3)|^2 - |A(\tau, z_2)|^2) \quad (3.2.29)$$

2) <u>Saturable absorbers ($z_1 < z < z_2$):</u>

The relation between input and output field amplitudes:

$$A(\tau, z_2) = e^{\left[-\frac{1-i\alpha_Q}{2} Q(\tau)\right]} A(\tau, z_1) \quad (3.2.30)$$

where $Q(\tau)$ is the dimensionless integral carrier density in the absorbing segment:

$$Q(\tau) = \int_{z_1}^{z_2} n_Q(\tau, \zeta)\, d\zeta \quad (3.2.31)$$

Similarly, including the internal non-resonant loss for the absorber section κ_2 in equation (30):

$$A(\tau, z_2) = \sqrt{\kappa_2} e^{\left[-\frac{1-i\alpha_Q}{2} Q(\tau)\right]} A(\tau, z_1) \quad (3.2.32)$$

In case of the absorber section, the equation (3.2.25), (3.2.26) and (3.2.28) are modified as:

$$\frac{\partial |A|^2}{\partial z} = -n_Q |A|^2 \quad (3.2.33)$$

$$-|A(\tau, z_2)|^2 + |A(\tau, z_1)|^2 = g_Q \Gamma_Q \int_{z_1}^{z_2} \left[N_Q - N_{0,Q}\right] |A|^2 d\zeta \quad (3.2.34)$$

$$\frac{\partial Q(\tau)}{\partial \tau} = -g_Q \Gamma_Q \int_{z_1}^{z_2} \left(\frac{N_{0,Q}}{\tau_q}\right) d\zeta - \frac{Q}{\tau_Q} - g_Q \Gamma_Q v_g (-|A(\tau, z_2)|^2 + |A(\tau, z_1)|^2) \quad (3.2.35)$$

The above equation describes the **time evolution transformation of $Q(\tau)$**.

3) <u>Passive segment ($z_3 < z < z_4$) and ($z_5 < z < z_1 + L$):</u>

The equations give the electric field amplitude transformation in these segments:

$$A(\tau, z_4) = \sqrt{\kappa_3} A(\tau, z_3),$$

$$A(\tau, z_1 + L) = A(\tau, z_5) \tag{3.2.36}$$

4) **Spectral Filter ($z_4 < z < z_5$):**

The component $A(\tau, z_5)$ contributing to the Gain profile forms a linear time-invariant system that is characterized by the impulse response f and convolution describes its action, so that equation (3.2.4) is equivalent to the time domain representation:

$$A(\tau, z_5) = f(\tau) \otimes \sqrt{\kappa_4} A(\tau, z_4)$$

$$A(\tau, z_5) = \sqrt{\kappa_4} \int_{-\infty}^{\tau} f(\tau - \theta) A(\theta, z_4)\, d\theta \tag{3.2.37}$$

From equation (3.2.5), the periodic boundary equation is modified to a form as:

$$E(t, z + L) = E(t, z)$$

$$A(\tau, z + L) = A(\tau + T, z) \tag{3.2.38}$$

The delay from the first segment to the last segment can be described as:

$$(D_T A)(\tau) = A(\tau - T) \tag{a}$$

Similarly, the delay from the last segment back to the first segment is described as:

$$(D_T A)(\tau + T) = A(\tau) \tag{b}$$

Substituting the equations (3.2.21), (3.2.29), (3.2.34), (3.2.36) into equation (3.2.35)

The transformation of the electric field amplitude at the input of the absorbing segment after a cavity roundtrip is given as:

$$A(\tau + T) = \sqrt{\kappa_1 \kappa_2 \kappa_3 \kappa_4} \int_{-\infty}^{\tau} f(\tau - \theta) e^{\left[\frac{1 - i\alpha_G}{2} G(\theta) - \frac{1 - i\alpha_Q}{2} Q(\theta)\right]} A(\theta)\, d\theta$$

In simplified version, the above equation can be written as:

$$\boldsymbol{A(\tau + T) = \sqrt{\kappa} \int_{-\infty}^{\tau} f(\tau - \theta) e^{\left[\frac{1 - i\alpha_G}{2} G(\theta) - \frac{1 - i\alpha_Q}{2} Q(\theta)\right]} A(\theta)\, d\theta} \tag{3.2.39}$$

Here, $\sqrt{\kappa} < 1$ where $\kappa = \kappa_1\kappa_2\kappa_3\kappa_4$ denotes the total internal attenuation losses experienced by the pulse as it travels the roundtrip inside the cavity. The factor κ is described as $\kappa = e^{-ax}$ where a is the attenuation loss per unit length and x denotes the length of the section for which the losses are accounted. Hence, κ is different for different elements depending upon the length of the section and the loss experienced by the light wave inside the section.

The notation $A(\tau) = A(\tau, z_1)$ and $T = L/v_g$ is the time of cavity roundtrip. Note that L is the round-trip length which is equal to twice the cavity length i.e. $L = 2l$.

Substituting

$$A(\tau, z_3),\ A(\tau, z_2) \text{ and } A(\tau, z_1) = A(\tau)$$

$$|A(\tau, z_2)|^2 = A(\tau, z_2) \cdot A^*(\tau, z_2)$$

$$|A(\tau, z_2)|^2 = \sqrt{\kappa_2} e^{\left[-\frac{1-i\alpha_Q}{2} Q(\tau)\right]} A(\tau, z_1) \cdot \sqrt{\kappa_2} e^{\left[-\frac{1+i\alpha_Q}{2} Q(\tau)\right]} A^*(\tau, z_1)$$

$$\Rightarrow\ |A(\tau, z_2)|^2 = \kappa_2 e^{\left[-\frac{1-i\alpha_Q+1+i\alpha_Q}{2} Q(\tau)\right]} |A(\tau, z_1)|^2$$

$$|A(\tau, z_2)|^2 = \kappa_2 e^{-Q(\tau)} |A(\tau, z_1)|^2 \tag{3.2.40}$$

Similarly, for the gain section, amplitude can be written as:

$$|A(\tau, z_3)|^2 = A(\tau, z_3) \cdot A^*(\tau, z_3)$$

$$|A(\tau, z_3)|^2 = \sqrt{\kappa_1} e^{\left[\frac{1-i\alpha_G}{2} G(\tau)\right]} A(\tau, z_2) \cdot \sqrt{\kappa_1} e^{\left[\frac{1+i\alpha_G}{2} G(\tau)\right]} A^*(\tau, z_2)$$

$$\Rightarrow\ |A(\tau, z_3)|^2 = \kappa_1 e^{\left[\frac{1-i\alpha_G+1+i\alpha_G}{2} G(\tau)\right]} |A(\tau, z_2)|^2$$

$$|A(\tau, z_3)|^2 = \kappa_1 e^{G(\tau)} |A(\tau, z_2)|^2$$

From equation (3.2.38) the above equation can be modified as:

$$|A(\tau, z_3)|^2 = \kappa_1\kappa_2 e^{G(\tau)}\, e^{-Q(\tau)} |A(\tau, z_1)|^2$$

$$|A(\tau, z_3)|^2 = \kappa_1\kappa_2 e^{G(\tau)}\, e^{-Q(\tau)} |A(\tau)|^2 \tag{3.2.41}$$

By using equations (3.2.40) and (3.2.41), the equations (3.2.29) and (3.2.35) are modified as:

$$\frac{\partial G(\tau)}{\partial \tau} = g_G\Gamma_G \int_{z_2}^{z_3} \left(J - \frac{N_{0,G}}{\tau_G}\right) d\zeta - \frac{G}{\tau_G} - g_G\Gamma_G v_g (\kappa_1\kappa_2 e^{G(\tau)}\, e^{-Q(\tau)} |A(\tau, z_1)|^2 - \kappa_2 e^{-Q(\tau)} |A(\tau, z_1)|^2)$$

$$\boldsymbol{\frac{\partial G(\tau)}{\partial \tau} = g_G \Gamma_G \int_{z_2}^{z_3} \left(J - \frac{N_{0,G}}{\tau_G}\right) d\zeta - \frac{G}{\tau_G} - g_G \Gamma_G \nu_g \kappa_2 e^{-Q(\tau)} (\kappa_1 e^{G(\tau)} - 1)\, |A(\tau)|^2} \quad (3.2.42)$$

$$\frac{\partial Q(\tau)}{\partial \tau} = -g_Q \Gamma_Q \int_{z_1}^{z_2} \left(\frac{N_{0,Q}}{\tau_Q}\right) d\zeta - \frac{Q}{\tau_Q} - g_Q \Gamma_Q \nu_g (|A(\tau, z_1)|^2 - \kappa_2 e^{-Q(\tau)}\, |A(\tau, z_1)|^2)$$

$$\boldsymbol{\frac{\partial Q(\tau)}{\partial \tau} = -g_Q \Gamma_Q \int_{z_1}^{z_2} \left(\frac{N_{0,Q}}{\tau_Q}\right) d\zeta - \frac{Q}{\tau_Q} - g_Q \Gamma_Q \nu_g \left(1 - \kappa_2 e^{-Q(\tau)}\right) |A(\tau)|^2} \quad (3.2.43)$$

The above highlighted equations describe the passive-mode locking in a ring laser with arbitrary line profile of spectral filter specified by the function $f(\tau)$.

Let us assume the Lorentz profile of the spectral filter:

$$f(\tau - \theta) = \gamma e^{-\gamma(\tau - \theta)} \quad (3.2.44)$$

The spectral filter functions as a bandpass filter. However, since it acts on a modulated carrier, it can be modelled as a low-pass filter applied to the complex envelope. The rationale behind this approach, where a bandpass filter is equivalently modelled as a low-pass filter, is thoroughly explained in the appendix section at the end of the document.

The Fourier transfer function of the low pass filter is given as:

$$H(\omega) = \frac{1}{1 + j\omega\tau_R}$$

where $\tau_R = \frac{2Q}{\omega_0}$

It has a Lorentzian line shape. The spectral power density becomes:

$$|H(\omega)|^2 = \frac{1}{1 + (\omega\tau_R)^2}$$

From equation (3.2.43) and using equation (3.2.16) of the appendix, the expression in equation (3.2.37) can be modified as a system of **delay differential equations** as:

$$\tau_R \frac{\partial A(\tau + T)}{\partial \tau} + A(\tau + T) = \left[\sqrt{\kappa} e^{\left[\frac{1 - i\alpha_G}{2} G(\tau) - \frac{1 - i\alpha_G}{2} Q(\tau)\right]} A(\tau)\right]$$

From equation (a), the above equation can be written as:

$$\frac{\partial A(\tau)}{\partial \tau} = \gamma \left[-A(\tau) + \sqrt{\kappa} e^{\left[\frac{1-i\alpha_G}{2} G(\tau - T) - \frac{1-i\alpha_Q}{2} Q(\tau - T)\right]} A(\tau - T) \right]$$

$$\boldsymbol{\frac{\partial A(\tau)}{\partial \tau} = \gamma \left[-A(\tau) + \sqrt{\kappa} e^{\left[\frac{1-i\alpha_G}{2} G(\tau - T) - \frac{1-i\alpha_Q}{2} Q(\tau - T)\right]} A(\tau - T) \right]} \quad (3.2.45)$$

where $\boldsymbol{\gamma = \frac{1}{\tau_R}}$

$$\boldsymbol{\frac{\partial G(\tau)}{\partial \tau} = g_G \Gamma_G \int_{z_2}^{z_3} \left(J - \frac{N_{0,G}}{\tau_G} \right) d\zeta - \frac{G}{\tau_G} - g_G \Gamma_G \nu_g \kappa_2 e^{-Q(\tau)} (\kappa_1 e^{G(\tau)} - 1) |A(\tau)|^2} \quad (3.2.46)$$

$$\boldsymbol{\frac{\partial Q(\tau)}{\partial \tau} = -g_Q \Gamma_Q \int_{z_1}^{z_2} \left(\frac{N_{0,Q}}{\tau_Q} \right) d\zeta - \frac{Q}{\tau_Q} - g_Q \Gamma_Q \nu_g \left(1 - \kappa_2 e^{-Q(\tau)}\right) |A(\tau)|^2} \quad (3.2.47)$$

The equations highlighted in the box above are the **delay differential integral equations** proposed in the paper[22].

3.3 Delay Differential Equation Modelling in Simulink

The Simulink implementation of the DDE model is based on the passive mode-locked lasers, as Vladimirov proposed in the DDE model. The functionality of the subsystems 'Phase Bias', 'Phase fluctuation', 'Initial condition', 'Delay', and 'Gain profile' subsystem blocks are thoroughly discussed in Section 2.5.

As discussed at the beginning of this chapter, a passive mode-locked laser comprises a saturable gain section and a saturable absorber section. This section will explore these subsystems in detail, highlighting their implementation and the resulting outputs.

The parameter values used in Simulink are based on estimations, with some extracted from the built-in passive mode-locking example in PICWave. The PICWave model serves as a reference, providing key parameters for the simulation.

The section begins with a discussion of the mode-locked laser implementation in PICWave, followed by an explanation of the implementation in Simulink.

3.3.1 Passive Mode-locked laser in PICWave

The passive mode-locking laser described in PICWave contains an InGaAsP active layer based on a ridge waveguide structure. The gain section has the length of $600\ \mu m$ and a ridge width of $5\ \mu m$, whereas the absorber section is $40\ \mu m$ in length. The epitaxial structures are identical for both the gain and absorber sections, with the primary differences in their lengths and operational conditions. The gain section is supplied with an injection current to achieve population inversion and amplification, whereas the absorber section operates without any electrical signal, as it must be reverse-biased to operate as a saturable absorber.

3.3.2 Parameter extraction for Simulink

The equation (3.2.29) can be modified to be written as:

$$\frac{\partial G(\tau)}{\partial \tau} = \frac{1}{\tau_G}[G_0 - G - s_G(|A(\tau, z_3)|^2 - |A(\tau, z_2)|^2)] \tag{3.3.1}$$

where,

$$G_0 = g_G \Gamma_G \int_{z_2}^{z_3} \left(\frac{J\tau_G}{N_{0,G}} - 1\right) d\zeta \tag{3.3.2}$$

$$s_G = g_G \Gamma_G v_g \tau_G |A|^2 \tag{3.3.3}$$

and

$$\tau_c = \tau_G \tag{3.3.4}$$

Simplifying the equation (3.3.1) in terms of gain would lead to the result:

$$G = \int \frac{1}{\tau_G} [G_0 - G - s_G(|A(\tau, z_3)|^2 - |A(\tau, z_2)|^2)] \ d\tau \tag{3.3.5}$$

Here, τ_c is the spontaneous carrier lifetime.

N_0 is the carrier density at transparency; it is a function of material

N is the carrier density of electrons and holes.

g is the differential gain coefficient which is a function of material.

Γ is the confinement factor

G is the gain of the gain section.

Substituting the value for $|A|^2$ from equation (3.1.48) in equation (3.3.3), the expression for s_G is reduced to:

$$s_G = g_G \Gamma_G \tau_G \frac{\mathcal{P}}{\sigma.\hbar\omega_0} \tag{3.3.6}$$

The carrier lifetime relaxation rate is the sum of radiative $(1/\tau_R)$ and non-radiative $(1/\tau_{NR})$ recombination rates.

$$\frac{1}{\tau_c} = \frac{1}{\tau_R} + \frac{1}{\tau_{NR}} \tag{3.3.7}$$

According to the reference[48], the radiative recombination rate is calculated as:

$$\frac{1}{\tau_R} = -\frac{1}{10^{-12} tr_0[ps]} - B_r[cm^3.s].N[cm^{-3}] - C_r[cm^6 s].N^2[cm^{-6}] \tag{3.3.8}$$

where, tr_0 is the inverse of Shockley-Read Hall coefficient, A_r.

B_r is the spontaneous emission recombination coefficient with units $(cm^3.s)$.

C_r is the Auger recombination coefficient with units $(cm^6 s)$.

These parameters are material-dependent; thus, they are extracted from the InGaAsP .mat file (attached in Figure 21) as InGaAsP is the device's active layer.

The parameters for the case of radiative and non-radiative recombination are presented in the Table 1.

```
//-----------------------------------------------------------------------
// define InGaAsP(x) material
// refractive index is for InGaAsP at the corresponding bandgap,
// and lattice matched to InP
// x is As content
BEGIN InGaAsP(x)                  // material name
ANAL_INGAASP1 20 0                // loads internal InGaAsP model at 20 Celcius
GAIN_POLYN 1.167e18  6.0e-6  1      // No [1/cm3] Gmat [cm3/s] polylen g_n2 g_n3... ;gain model
GAIN_LAMFUNC 10000 1.475 0.0 0.0 0 0    // g2[um-2] lam0[um] lamN1 lamN2 lamT1 lamT2
GAIN_EPS   1.04e-16                     // gaineps (non-linear gain) [cm3]
RADRECOMB  1e20    2e-10   0.0     // tsr0[ps]  Btsr[cm3/s]  Ctsr[cm6/s]  ; rad recombination
NRADRECOMB 1e4     0.0     0.0     // tsnr0[ps] Btsnr[cm3/s] Ctsnr[cm6/s] ; non-rad recombination
DIFFUSION  20.0    0               // Ddif0[cm2/s] Ddif_n[cm5/s] ; diffusion coefficients
LEF        0                       // lef ; linewidth enhancement factor
RHO        600                     // rho ; electrical resistivity
DOSCB 2.9E17          // [cm-3] dos in conduction band
DOSVB 8.4E17          // [cm-3] dos in valence band
END
//-----------------------------------------------------------------------
// define InGaAsP_SA(x) material (x-Parameter is bandgap - Saturable absorber material)
BEGIN InGaAsP_SA << InGaAsP
GAIN_POLYN 1.167e18  24.0e-6  1       // No [1/cm3] Gmat [cm3/s] polylen g_n2 g_n3... ;gain model
GAIN_LAMFUNC 10000 1.475 0.0 0.0 0 0  // g2[um-2] lam0[um] lamN1 lamN2 lamT1 lamT2
LEF        0                          // lef ; linewidth enhancement factor
NRADRECOMB 0.01     0.0     0.0       // tsnr0[ps] Btsnr[cm3/s] Ctsnr[cm6/s] ; non-rad recombination
END

//-----------------------------------------------------------------------
// define InGaAsP_SA(x) material (x-Parameter is bandgap - Saturable absorber material)
BEGIN InGaAsP_FP << InGaAsP
GAIN_POLYN 1.167e18  6.0e-6  1      // No [1/cm3] Gmat [cm3/s] polylen g_n2 g_n3... ;gain model
GAIN_LAMFUNC 10000 1.475 0.0 0.0 0 0    // g2[um-2] lam0[um] lamN1 lamN2 lamT1 lamT2
GAIN_EPS   1.04e-16                     // gaineps (non-linear gain) [cm3]
LEF        3                            // lef ; linewidth enhancement factor
END
//-----------------------------------------------------------------------
// define InGaAsPL(x) material (x-Parameter is bandgap)
BEGIN InGaAsPL << InGaAsP
ANAL_INGAASP1 20 1                // loads internal InGaAsP model at 20 Celcius
END
//-----------------------------------------------------------------------
```

Figure 21: InGaAsP material file in Harold

Parameters	Symbols	Units	Values
Shockley-Read Hall coefficient inverse	tr_0	ps	1×10^{20}
	tnr_0	ps	1×10^{4}
Spontaneous emission radiative recombination coefficient	B_r	cm^3/s	2×10^{-10}
Auger recombination coefficient	C_r	cm^6/s	0
Carrier density at transparency	$N_{0,G}$	cm^{-3}	1.167×10^{18}
Differential gain	g_G	cm^3/s	6×10^{-6}

Table 1: Parameter values for gain section

Similarly, the material parameters for the absorber section are summarized in the table below:

Parameters	Symbols	Units	Values
Shockley-Read Hall coefficient inverse	tnr_0	ps	0.01
Auger recombination coefficient	C_r	cm^6/s	0
Carrier density at transparency	$N_{0,Q}$	cm^{-3}	1.167×10^{18}
Differential gain	g_Q	cm^3/s	24×10^{-6}

Table 2: InGaAsP material parameters for saturable absorber section.

The charge carrier lifetime in the gain section of Quantum well lasers is ranges from $0.1 - 1ns$ and the carrier lifetime for absorber section is typically between $5 - 50ps$[49]. For simplicity, the carrier lifetimes in the gain and absorber sections are assumed to be equal.

The values of other parameters such as the confinement factor and group velocity are obtained as presented below:

- **Carrier lifetime, $\boldsymbol{\tau_c = 1\ ns = \tau_G = \tau_Q}$**
- **Confinement factor $\boldsymbol{\Gamma = 0.07864}$**
- **Group velocity, $\boldsymbol{v_g}$**

  In PICWave, the group velocity is a function of *zStep* and *tStep* simulation parameters which is given as:

$$t_{step} = \frac{z_{step}}{v_g} \tag{3.3.8}$$

$$\Rightarrow \quad v_g = \frac{z_{step}}{t_{step}} = \frac{10\ (\mu m)}{0.12305\ (ps)} = 81.26777 \times 10^6 (m/s)$$

$$\Rightarrow \quad \boxed{\boldsymbol{v_g = 0.81267 \times 10^{10} (cm/s)}}$$

After substituting the values into equations (3.3.2), (3.3.3), and (3.3.5), and performing the dimensionless conversion of the parameters to make them suitable for simulations, the parameters for the gain and absorber sections are outlined in Table 3:

Parameters	Symbols	Dimensionless Values
Saturation in gain section	s_G	1
Injection in gain section	G_0	$\log 6$
Recovery time	τ_G	1×10^3
Saturation in absorber section	s_Q	10
Injection in gain section	Q_0	-1
Recovery time	τ_Q	1×10^3
Linewidth enhancement factor	α_H	0

Table 3: Parameter values for Simulink simulations

3.3.3 Implementation of DDE model in Simulink

The Simulink model implementing the DDE framework for the passive mode-locking mechanism is represented in Figure 22.

a)

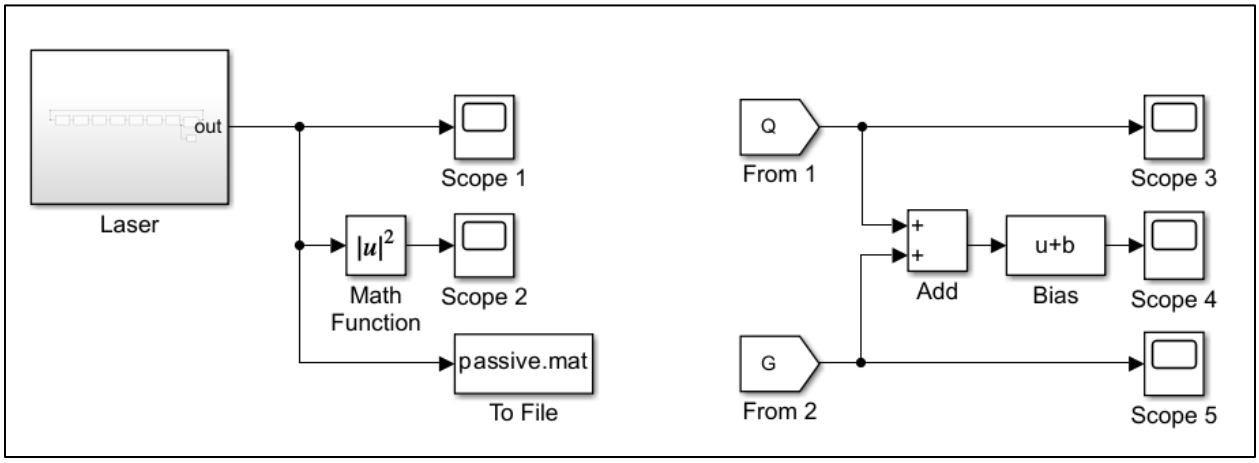

b)

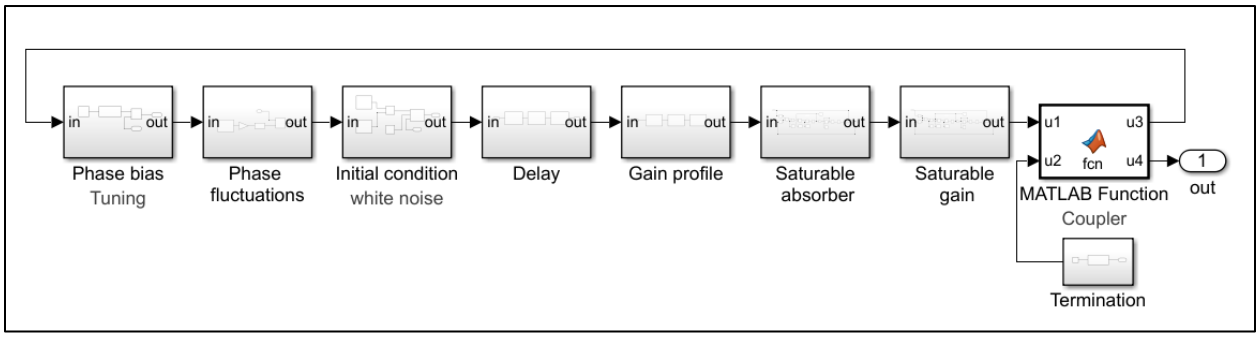

c)

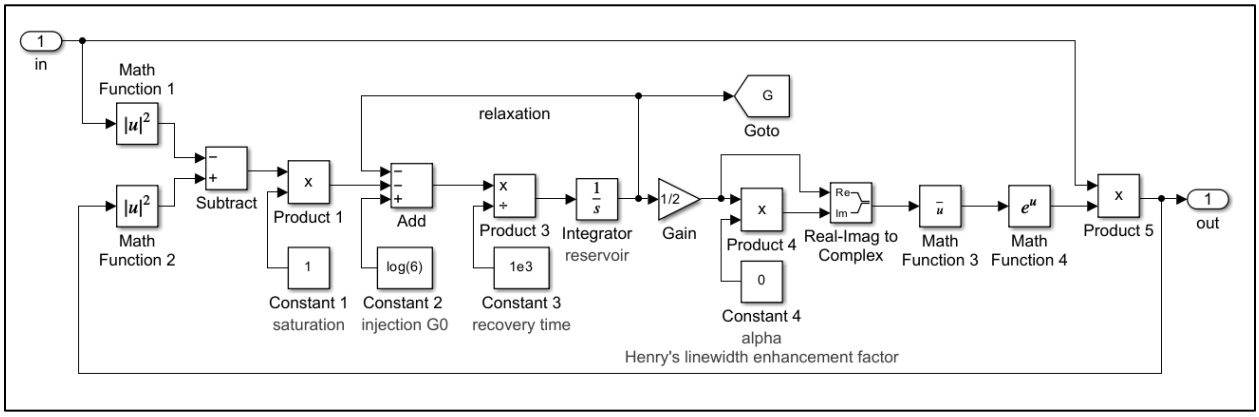

d)

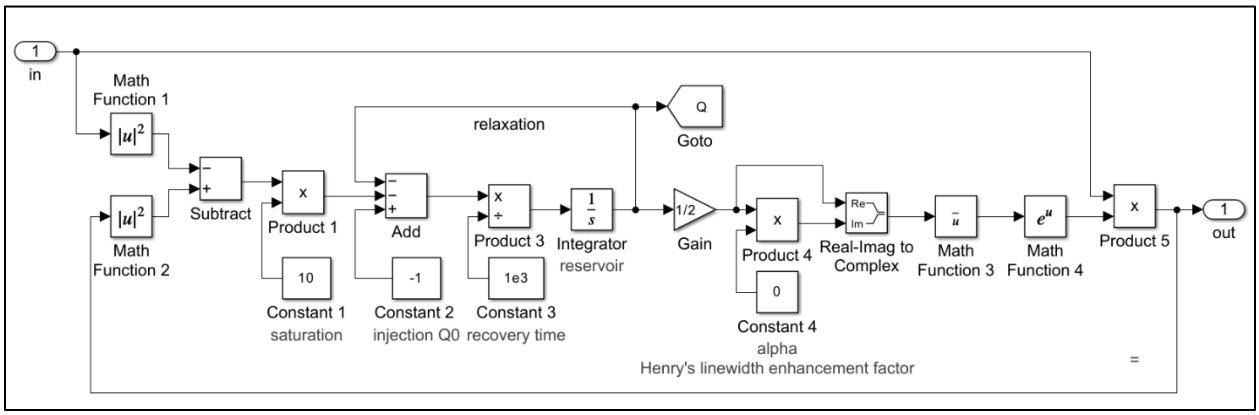

Figure 22: a) Block diagram illustrating the passive mode-locking mechanism implemented in Simulink. (b) The 'Laser' subsystem, displays components such as phase bias, phase fluctuation, initial conditions, delay, and other key blocks. (c) Internal structure of the Saturable Gain subsystem. (d) Internal structure of the Saturable Absorber subsystem implementing the absorber Delay Differential Equation.

The equations implemented in the saturable gain section, illustrated in Figure 22c) are:

$$A(\tau, z_3) = \sqrt{\kappa_1} e^{\left[\frac{1-i\alpha_G}{2} G(\tau)\right]} A(\tau, z_2) \qquad (i)$$

and

$$|\boldsymbol{A(\tau, z_3)}|^2 = \boldsymbol{\kappa_1 e^{G(\tau)} |A(\tau, z_2)|^2} \qquad (ii)$$

These equations are discussed in detail in Section 3.2 under "1) Amplifying segment". Since, Henry's linewidth factor is neglected, equation (i) is simplified as:

$$\boldsymbol{A(\tau, z_3) = \sqrt{\kappa_1} e^{\frac{1}{2} G(\tau)} . A(\tau, z_2)} \qquad (iii)$$

For the saturable absorber block (Figure 22d), the equations implemented are:

$$\boldsymbol{A(\tau, z_2) = \sqrt{\kappa_2} e^{-\frac{1}{2} Q(\tau)} . A(\tau, z_1)} \qquad (iv)$$

$$\boldsymbol{|A(\tau, z_2)|^2 = \kappa_2 e^{-Q(\tau)} |A(\tau, z_1)|^2} \qquad (v)$$

Here, κ_1 and κ_2 represents the non-resonant losses at the facets of gain and absorber segments respectively each of the section. These are assumed to be equal in both the gain and absorber segments, i.e. $\kappa_1 = \kappa_2 = \kappa$. The loss is implemented by the output coupler block, which is depicted as the coupler block in Figure 22b).

a)

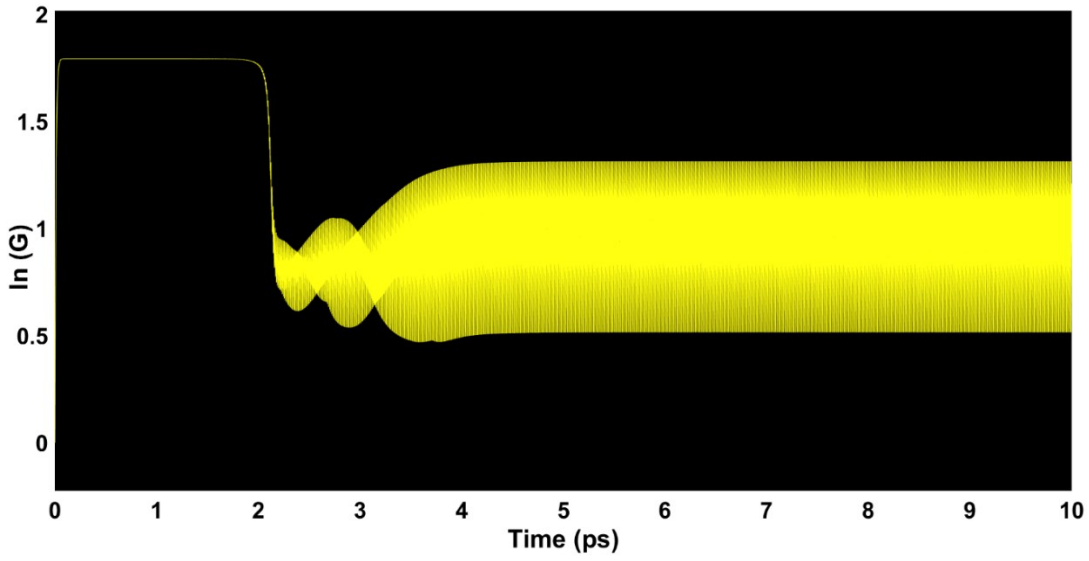

b)

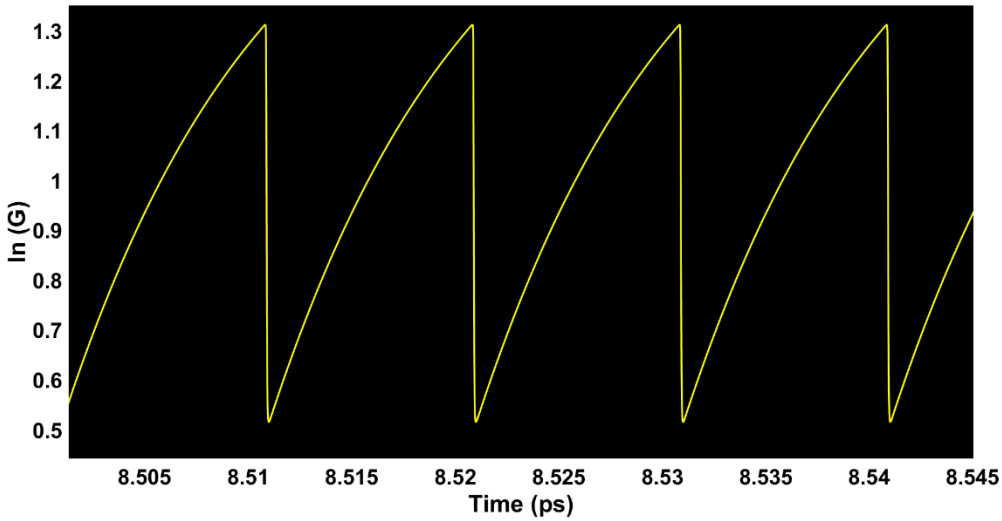

Figure 23: Simulation results representing the mode-locking dynamics within the saturable gain section.

Figure 23a) illustrates the amplification and sustenance of optical fields within the laser cavity. The results show the evolution of light pulses originating from random noise caused by spontaneous emission. Within this noise, short-duration pulses are selectively amplified. As the light waves reflect back and forth within the cavity, repeatedly passing through the gain section, the gain compensates for the losses in the cavity as the intensity of the light waves increases due to stimulated emission. Over time, the gain saturates, reaching a steady state, as depicted in Figure 23a).

In contrast, the dynamics of the absorber section operate inversely to those of the gain section. This contrast is evident when comparing Figure 23b) and Figure 24b), highlighting the opposing behaviours of gain and absorber sections.

The saturable absorber plays a crucial role in generating light pulses. It absorbs low-intensity light while allowing high-intensity light waves to pass through. As the intensity increases, the absorber saturates, reducing the losses experienced by the pulse. This loss reduction facilitates pulse formation. In a steady state, the pulse experiences minimal loss, leading to amplification and a further reduction in pulse duration, depicted in Figure 27.

a)

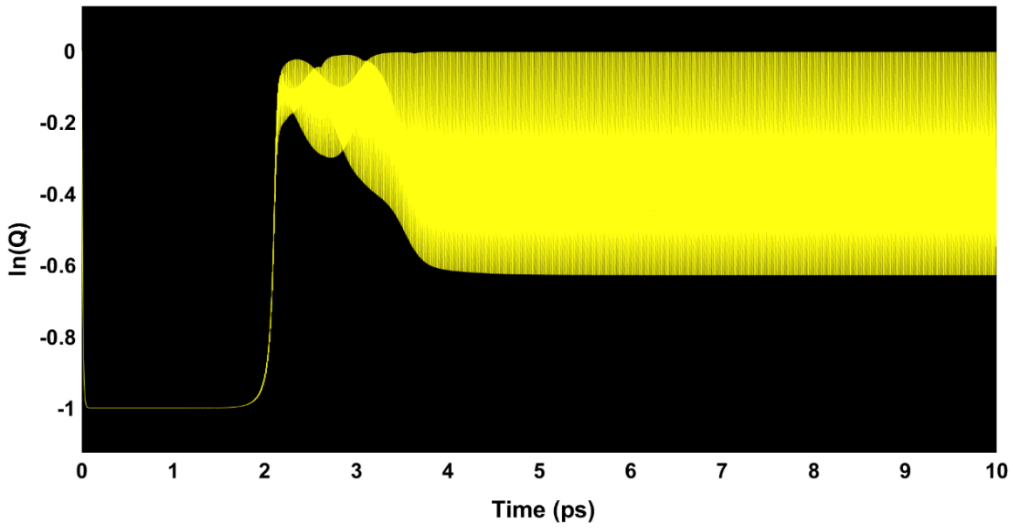

b)

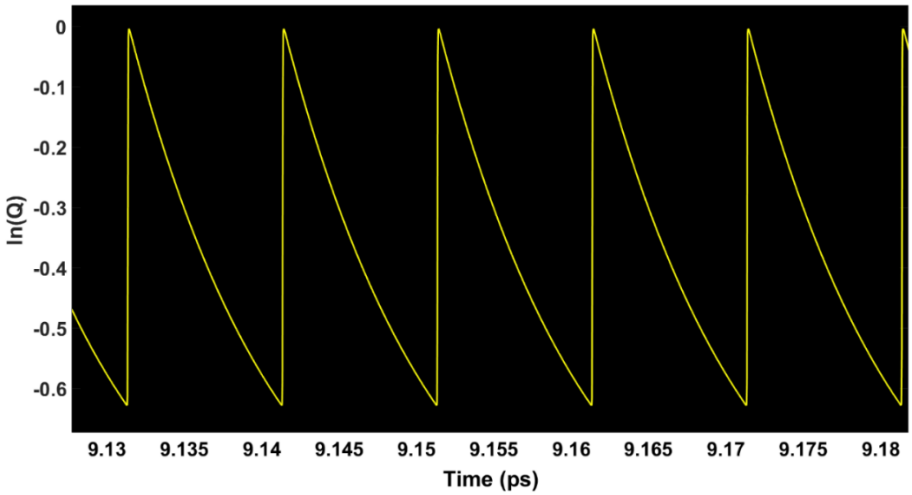

Figure 24: Simulink results representing the dynamics of the saturable absorber section.

The net gain in passive mode-locked lasers represents the balance between the amplification provided by the gain section and the losses introduced by the saturable absorber and other components, such as the output coupler. As illustrated in the Figure 25, an initial small net gain enables the buildup of noise within the cavity, which subsequently evolves into mode-locked pulses. Once the system stabilizes, the net gain reaches a constant value, with a maximum peak of 0.4, which is less than the magnitude obtained in the gain section. This indicates that the amplification by the gain section is balanced by the total losses within the cavity.

This balance is crucial for the formation of stable pulses and the sustained operation of mode-locking within the laser cavity.

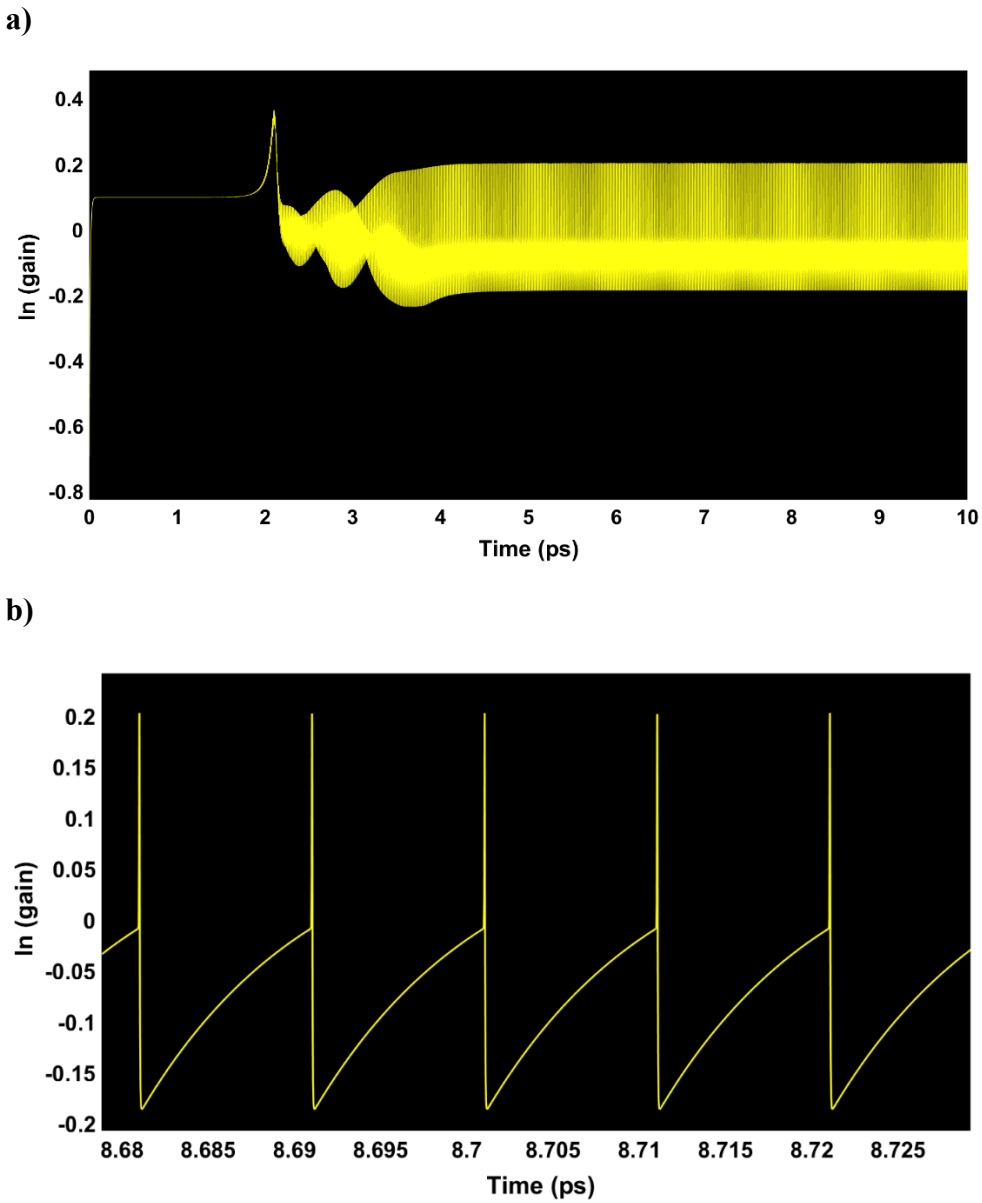

Figure 25: Results illustrating the net gain within the laser cavity, highlighting the initial buildup of noise leading to mode-locked pulses and the eventual stabilization of the net gain, where amplification is balanced by the cavity losses.

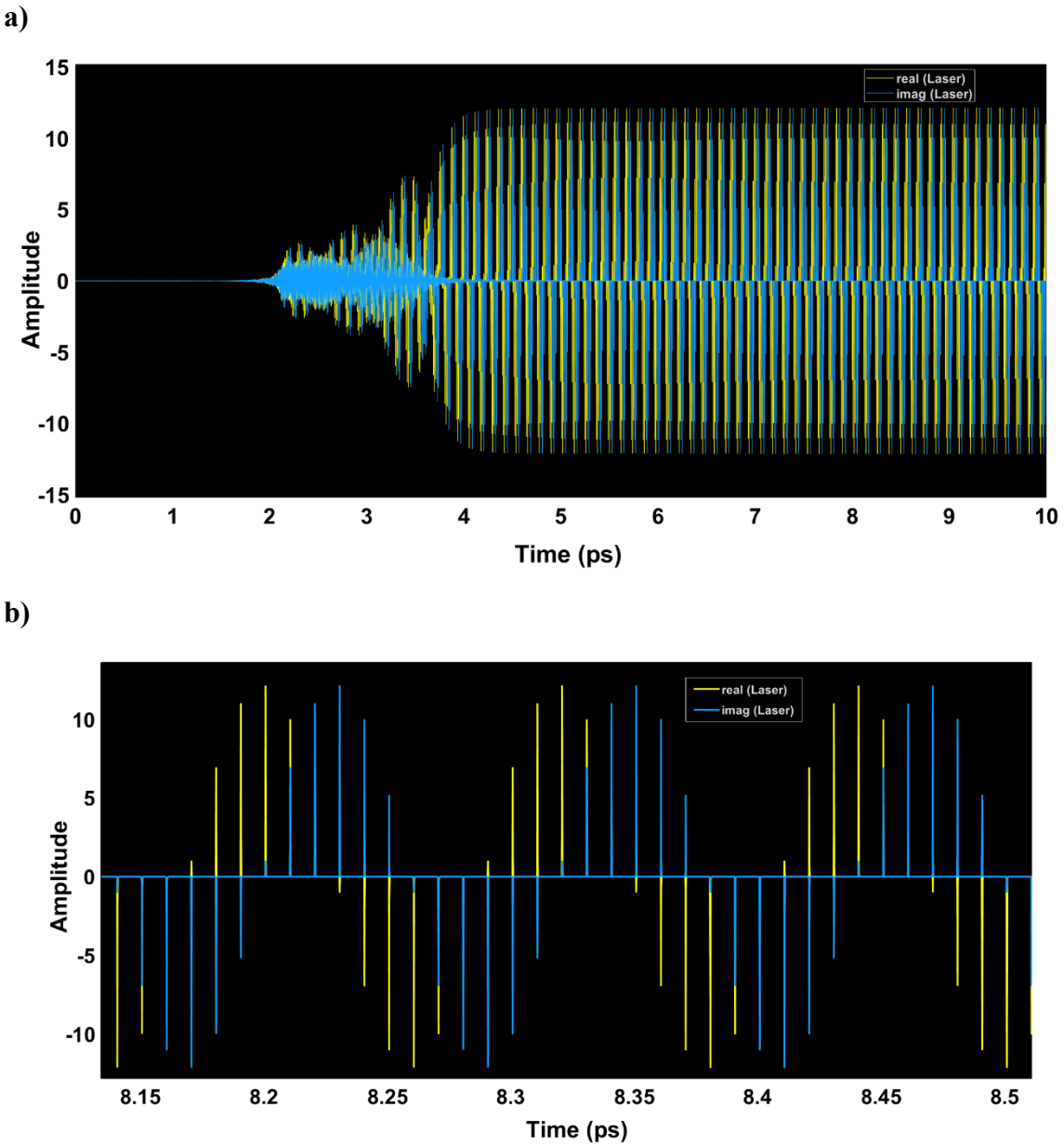

Figure 26: The results illustrate the evolution of a) the complex envelope from noise to a mode-locked mechanism, showcasing the temporal progression of the slowly varying complex envelope, A. b) Depicts the zoomed image of the envelope.

Figure 26 illustrates the temporal evolution of the complex envelope starting from noise contributed primarily by spontaneous emission. It demonstrates the implementation of Equation (3.2.45), as discussed in Section 3.2, and highlights the dynamics in the slowly varying envelope A.

a)

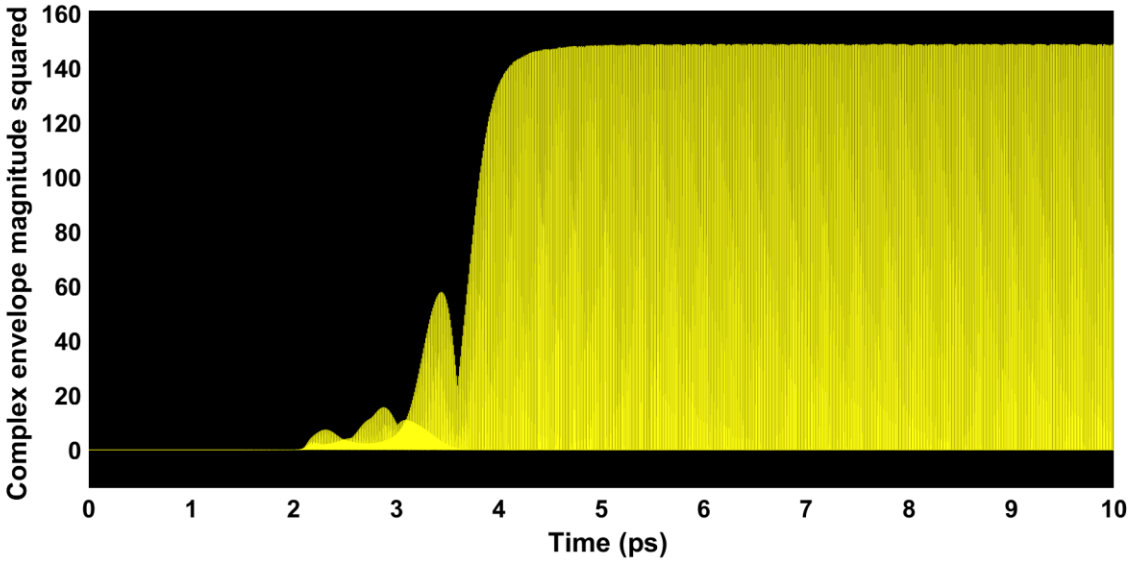

b)

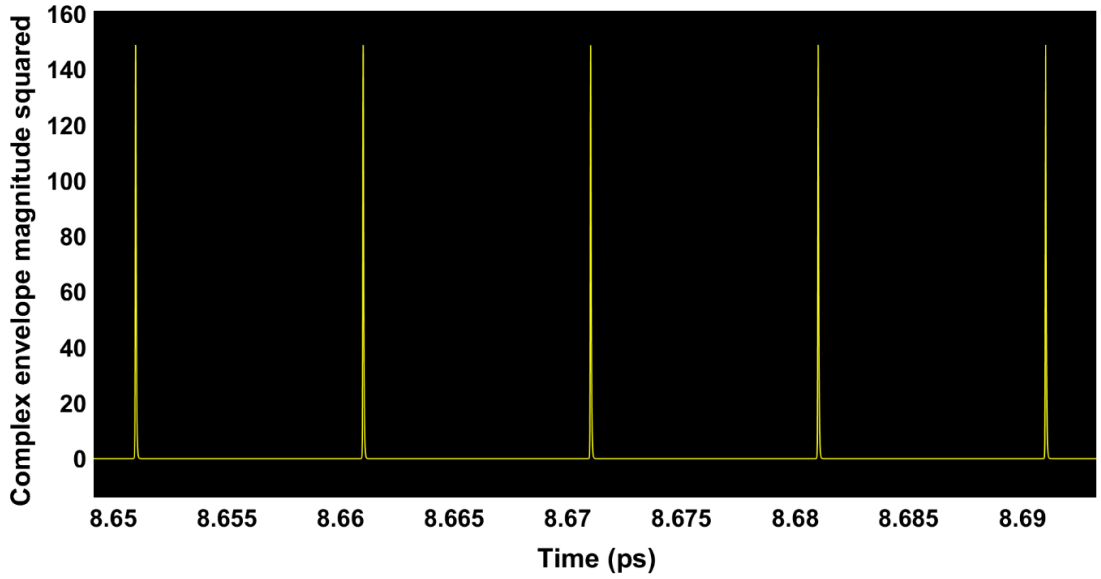

Figure 27: Temporal evolution of optical power in a passive mode-locked laser. These results are obtained by squaring the magnitude of the complex envelope i.e. $|A|^2$.

The observed results are consistent with the theoretical predictions and demonstrate how the balance of gain, loss, and other non-linear effects within the cavity contribute to the formation of mode-locked pulses. These findings provide insight into the dynamics of the passive mode-locking mechanism and its reliance on the slowly varying envelope approximation accurate modelling.

3.4 Model for mode-locking in Semiconductor Quantum Dot Lasers

The Delay Differential Equation model discussed in the previous section is for the semiconductor Quantum-Well structures proposed by Vladimirov[22]. However, this section extends the DDE equations for the Quantum Dot structures. This model is proposed by Viktorov as attached in the references[5],[50]. The saturable gain and absorption in the gain and absorber sections respectively are given as:

$$G(t) = 2g_g L_g[2\rho_g(t) - 1] \tag{3.4.1}$$

$$Q(t) = -2g_q L_q[2\rho_q(t) - 1] \tag{3.4.2}$$

The terms $\rho_g(t)$ and $\rho_q(t)$ describes the occupation probabilities in a dot located in the amplifying and the absorber sections, respectively.

By using the equations discussed in the previous section, the expression describing the occupational probabilities in dot and carrier densities in the amplifying and absorber sections can be described as[50]:

$$\frac{\partial \rho_g}{\partial t} = -\gamma_g \rho_g + F_g(\rho_g, N_g) - e^{-Q}(e^G - 1)|A|^2 \tag{3.4.3}$$

$$\frac{\partial \rho_q}{\partial t} = -\gamma_q \rho_q + F_q(\rho_q, N_q) - s(1 - e^{-Q})|A|^2 \tag{3.4.4}$$

The carrier densities in the wetting layers in gain and absorber sections is given by the equations:

$$\frac{\partial N_g}{\partial t} = N_{g0} - \Gamma_g N_g - 2F_g(\rho_g, N_g) \tag{3.4.5}$$

$$\frac{\partial N_q}{\partial t} = N_{q0} - \Gamma_q N_q - 2F_q(\rho_q, N_q) \tag{3.4.6}$$

Here,

$L_{g,q}$: describes the length of gain and absorber sections respectively

ρ_g: describes the occupation probabilities in a dot located in gain section.

ρ_q: describes the occupation probabilities in a dot placed in absorber section.

N: describes the carrier densities in the wetting layers or the QD carrier density.

$\Gamma_{g,q}$: describes the carrier relaxation rates in the wetting layers in gain and absorber sections respectively.

$\gamma_{g,q}$: defines the carrier relaxation rates in dots located in the gain and absorber sections respectively.

$F_{g,q}(\rho_{g,q}, N_{g,q})$: describes the carrier exchange rates between the wetting layers and the dots in the gain and absorber sections which is described as:

$$F_g(\rho_g, N_g) = R_g^{capture}(1 - \rho_g) - R_g^{escape}\rho_g \tag{3.4.7}$$

Similarly, for the absorbing section the carrier exchange rate between the wetting layers and dots is defined as:

$$F_q(\rho_q, N_q) = R_q^{capture}(1 - \rho_q) - R_q^{escape}\rho_q \tag{3.4.8}$$

where $1 - \rho_{g,q}$ is the Pauli blocking factor and

$R_{g,q}^{capture} = B_{g,q}N_{g,q}$ where $B_{g,q}$ is the rate at which the carriers $N_{g,q}$ are captured from the wetting layers to the dots in the gain and absorber segments respectively.

$R_{g,q}^{escape}$ is the coefficient describing the escape of the carriers from the QDots in the amplifying and absorbing segments to the wetting layers. It is a temperature-dependent coefficient.

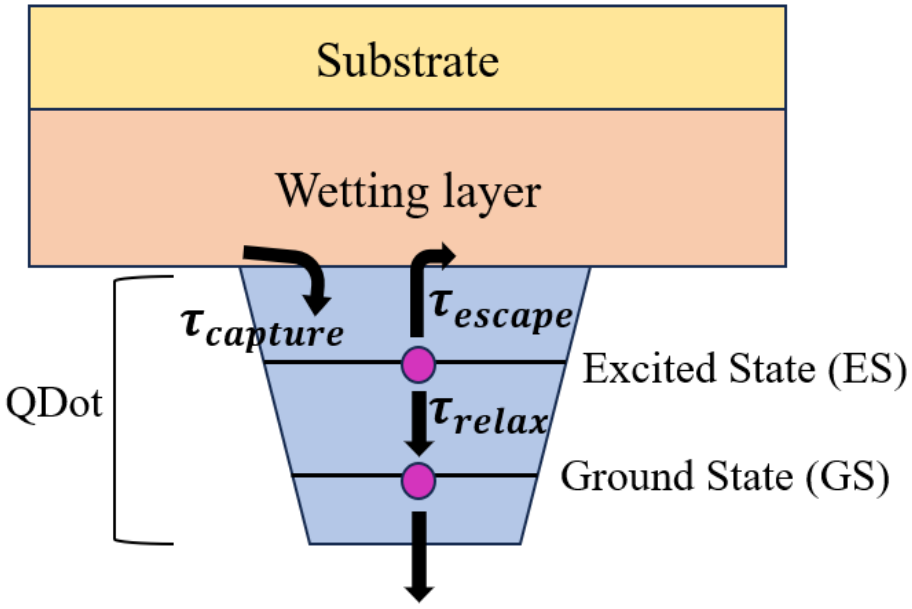

Figure 28: Schematic diagram representing the carrier dynamics in Quantum dot structures

The schematic of carrier dynamics in Figure 28 shows the different timescales involved in the carrier dynamics. τ_{escape} describes the rate at which the carriers transition from the Quantum Dot

material to the wetting layer material, while $\tau_{capture}$ denotes the rate for the transition of carriers from the wetting layer (WL) material to either the ground state (GS) or the excited state (ES) within the QDot structure. Similarly, τ_{relax} describes the intraband relaxation rate of the carriers within the QDot.

When carriers are pumped into the wetting layer by an applied injection current, they are captured from the 2-D WL into the ES of the QDot at a rate denoted by $\tau_{capture}$. The "captured" carriers then further relax into the GS, denoted by τ_{relax}. According to[51], the GS of the QDot can accommodate only two electrons-hole pairs (excitons). The relaxation rate from ES to GS is limited by the Pauli-blocking effect, which prevents more than two carriers from occupying the same quantum state. This effect is defined by a factor $(1-\rho)$ where ρ describes the occupational probabilities in the GS and ES.

When the injection current and the rate of stimulated emission exceeds the threshold, the carrier density in the WL increases, triggering the "capture" mechanism in the QDot structure. These carriers tend to occupy the ES before relaxing down to the GS. However, due to Pauli-blocking effect, only two carriers can occupy the GS, hence reducing the relaxation rate from ES to GS. As the carrier population increases in the ES relative to that in the GS, an uneven distribution of carriers arises, ultimately limiting the radiative emission from the GS. This results in the saturation of output power from the GS, because further relaxation of carriers from the ES would not contribute to lasing. When the carrier population in the ES increases beyond a threshold value, the radiative recombination from the ES begins to contribute to lasing, leading the ES to compete with the GS for carriers and optical gain. Consequently, the GS is no longer the sole contributor to lasing operation. This competition affects the overall lasing performance, leading to asymmetries in the gain spectrum and higher values of linewidth enhancement factor, α.

In dynamic operation, the QDot-based laser needs to respond swiftly to changes introduced in parameters such as injection current, and carrier densities, and carriers must move quickly between energy states within the QDots for the laser to function effectively in high-speed systems. However, the limited carrier occupation in the GS reduces parameters such as differential gain and results in gain compression which occurs in the laser when the optical gain decreases at high output intensities. The gain gets 'compressed' even if the carrier concentration is fixed at a stable value, ultimately reducing the laser's quantum efficiency and output power[3],[51].

3.5 Results and Discussions

This chapter presents a comprehensive mathematical analysis of two time-domain models: the Time Domain Travelling Wave (TDTW) model and Delay Differential Equation (DDE) model, which is based on the lumped element approach. The extraction of critical parameters, such as differential gain and saturation constants, from PICWave and their subsequent implementation in Simulink have yielded key findings regarding the establishment of the mode-locking regime within the laser cavity. The parameters are detailed in Table 3.

Section 3.3 provides valuable insights into the dynamics responsible for the initiation and sustenance of the mode-locking mechanism, beginning from the spontaneous emission noise. The results demonstrate that the complex envelope is well-described by Equation (3.2.45) of the DDE model (Section 3.2), while Figure 23 and Figure 24 illustrates the implementation and visualization of the dynamic interactions within the gain and absorber sections equations (3.2.46) and (3.2.47), discussed in Section 3.2. These findings significantly enhance the understanding of the mode-locking phenomenon, fulfilling the study's objectives.

Additionally, the simulations validate the practicality of the DDE model, demonstrating its capability for numerically simulating the physical processes within the cavity. The pulse widths obtained are on the order of $1\ ps$, aligning with expected outcomes.

While several authors have performed mathematical analyses of the DDE and TDTW models, their works often lack clarity and omit critical steps in the derivations. The models developed in this study address these gaps by providing a more transparent and detailed explanation of the mathematical processes, offering readers a clearer understanding of the steps involved in deriving the final outputs of the DDE and TDTW models.

These models have also been extended to describe Quantum Dot (QDot) structures, as presented in Section 3.4. However, the Simulink implementation of the DDE model for Quantum Dots remains a potential avenue for further research to extend this work.

CHAPTER 4
Simulation Tools

4.1 Introduction

In this chapter, we will discuss two commercial simulation tools, Harold and PICWave, primarily used to simulate Quantum-well laser structures for the thesis project. The Photon Design's simulation tool, Harold, is a heterostructure simulator which is used to model Fabry-Perot Quantum well laser structures. The tool can describe the electrical, optical, and thermal properties of laser diodes. Harold can support one-dimension and two-dimensional running modes, which perform the analysis in the vertical direction, and both YZ directions i.e. vertical and longitudinal device axes. Harold contains additional modules like HaroldXY module, which enables the modelling of laser devices with different geometrical shapes.

The other simulation tool, PICWave is an acronym for Photonic Integrated Circuit simulator, and Wave refers to the Time Domain Travelling Wave (TDTW) model used by the simulator to perform time-domain analysis of the laser device. In addition to simulating laser devices, it can also be used to simulate other active and passive optical components such as Mach Zehnder interferometers, ring resonators etc. A detailed description of the tool's capabilities can be found in reference[48]. The simulator can model various physical processes, including lateral carrier diffusion, dispersion, spectral hole-burning, spatial hole-burning in the lateral and longitudinal direction, non-linear gain, and free carrier absorption. The visualization of these complex physical processes is important for providing a better understanding of the dynamics of the mode-locking phenomenon. However, a limitation of these simulation tools, at the time of writing the thesis, is that these can only support Quantum-well structures and do not include the modelling of more

complex structures like Quantum Dots and Quantum Dashes in the gain medium. PICWave can be used to visualize the mode-locking phenomenon in Quantum-well laser devices.

One of the most important features of these two simulation tools is their ability to import and export model files between one another. Harold can export a laser device model, including gain, material, epitaxial, and spontaneous emission data, to the circuit simulation tool PICWave. This feature of both tools is extensively used in the work published in this thesis.

4.2 Simulation Process in Harold

The first step in modelling the geometry of laser device is by selecting the type and material of layers from a library of different material database such as bulk, metal, QWells. In the next step, other important geometrical aspects such as the layer thicknesses, doping concentrations and alloy compositions of layers are specified in the epitaxial layer editor of the tool. After the completion of this step, the complete epitaxial structure of the device is ready with layers of specific type, thicknesses, material doping, and alloy compositions stacked onto the substrate. The basic version of Harold focuses on defining the properties of epitaxial structure in the vertical direction. However, it solves the equations for electrical, optical, and thermal models in both the vertical and longitudinal directions.

Once the epitaxial structure information of the device is incorporated in the simulator, the device is discretized spatially along y-axis of each layer. The spatial discretization of the entire structure in Harold forms various rectangular elements of specific materials. The equations are solved for each rectangular element and the summation of solution of each element describes the characteristics of the device. Harold uses three discretization meshes for different models, Y-mesh for electrical and optical calculations, T-mesh for thermal calculations of the device and Z-mesh for scaling the device along the cavity axis. The latter meshing is not used by Harold internally. However, it is used when the device structure from Harold is imported to other simulation tools like PICWave for further analysis.

In the device editor window, some other geometrical parameters such as the device dimensions, scattering losses, and the reflectivity of the facets for Fabry-Perot lasers are described. Following the device specifications, the simulator window asks the users to define simulation parameters. Here the parameters like the maximum current, step size of current increment, wavelength range are specified. Then, Harold asks to run the simulations in any one of the three execution modes. The user selects one of the three execution modes depending on the application and device structure. The three execution modes are:

a) **Isothermal mode**: This mode is enabled for the pulsed operation of the laser.

b) **Self-heating mode**: This mode allows to model the continuous wave operation of the laser. It models the effect of temperature increment on the Light-Current (L-I) characteristics of the device. The increase in temperature is known to affect various physical processes such as the optical gain, optical losses, non-radiative recombination mechanisms, reduction in bandgap and carrier mobility[52]. With high temperatures, the resistance of the top contact increases which impacts the electrical characteristics of the device eventually causing a reduction in the optical gain of laser device. The primary contributor to increase in temperature is the current flowing through the device, this effect is called as Joule heating. To compensate for the decrease in optical gain of the quantum wells, the carrier density increases, due to which the recombination due to Auger process becomes more significant. The Auger recombination process is a mechanism in which the electron and hole recombines and instead of photon emission, the heat generated during the recombination process is taken up by a third carrier, an electron to come to the edge of the conduction band.

c) **Test mode**: This mode performs a quick 0V bias run to check that the device and its epitaxial structure are set up correctly.

Once the execution mode of the device is set up correctly based on the laser operation of interest, the next step is to define the dimensions for obtaining various simulation results:

1) **One-dimensional mode**: This mode performs computations and generates data only for Y-direction (vertical).
2) **Two-dimensional mode**: In this running mode, Harold generates simulation results for variations in different parameters across both the Y-direction (vertical) and along the cavity axis, Z- direction (longitudinal).
3) **PICWave mode**: This mode is chosen when the gain function data for the quantum well layer structures have to be imported into PICWave. It enables the modelling of other dynamics like stochastic noise, spectral hole burning, dispersion, and other behaviours of the designed laser structure. This execution mode generates gain results relative to carrier densities and temperature. The PICWave model is generated by running the 1-D isothermal mode for a set of bias currents and temperatures. This process generates files containing epitaxial layer data (.swg), material gain spectra (.gain) for carrier densities and temperatures using either the parabolic band or k.p model, spontaneous emission spectra (.spon) and material properties (.mat) such as refractive index, scattering loss, free carrier absorption, electron and hole mobility, and others. The Harold-PICWave link will be discussed in more detail in a later section of this chapter.

4.3 Basic Semiconductor Optoelectronic Equations

The core of each spatially resolved quantum well simulation lies in the Poisson, drift-diffusion, continuity, capture/escape and photon rate equations. These equations describe the electrical, thermal, and optical characteristics of the laser module.

In this section, we present the basic semiconductor optoelectronic equations which are used in modelling the semiconductor devices. These equations are based on Maxwell's equations and charge continuity equations[53].

The well-known fundamental Maxwell's equations are given as:

$$\nabla \times E = -\frac{\partial B}{\partial t} \tag{4.3.1}$$

$$\nabla \times H = J + \frac{\partial D}{\partial t} \tag{4.3.2}$$

$$\nabla . D = \rho \tag{4.3.3}$$

$$\nabla . B = 0 \tag{4.3.4}$$

where E is the electric field (V/m), H is the magnetic field (A/m), D is the electric displacement flux density (C/m^2), B is the magnetic flux density (Vs/m^2), J is the current density (A/m^2), ρ is the charge density (C/m^3).

In an isotropic medium, the magnetic flux density and electric displacement flux density can be extended as:

$$B = \mu H \text{ and } D = \varepsilon E \tag{4.3.5}$$

Here, μ describes the magnetic permeability of material and ε is the dielectric constant of the material.

4.3.1 Poisson's Equation

For the devices operating at low frequency or DC biases, the variation of the equation relative to time is almost negligible $\left(\frac{\partial}{\partial t} \approx 0\right)$ Hence, the equation (4.3.1) can be modified as:

$$\nabla \times E = 0 \tag{4.3.6}$$

Under an assumption that there is no application of external magnetic fields, the solution of the electric field is expressed as:

$$E = -\nabla\phi \tag{4.3.7}$$

Using relations in equations (4.3.5) and (4.3.7), equation (4.3.3) becomes:

$$\boldsymbol{\nabla.(\varepsilon\nabla\phi) = -\rho} \tag{4.3.8}$$

Equation (4.3.8) is the Poisson's equation where ϕ is the electrostatic potential and ρ is the charge density.

The overall charge density is described as:

$$\rho = q(p_T - n_T + N_D - N_A) \tag{4.3.9}$$

Substituting equation (4.3.9) in (4.3.8), the Poisson's equation becomes:

$$\boxed{\boldsymbol{\nabla.(\varepsilon\nabla\phi) + q(p_T - n_T + N_D - N_A) = 0}} \tag{4.3.10}$$

where ε is the dielectric constant, q is the magnitude of a unit charge, N_D and N_A represents the ionized donor and acceptor concentrations, respectively. p_T and n_T denote the sum of unconfined (p, n) and confined hole and electron densities (p_{QW}, n_{QW}) present in the quantum well structure. The relationships are given as:

$$p_T = p + p_{QW} \tag{4.3.11}$$

$$n_T = n + n_{QW} \tag{4.3.12}$$

4.3.2 Continuity Equations

From Maxwell's Ampere law

$$\nabla \times H = J + \frac{\partial D}{\partial t}$$

where H is the magnetic field (A/m), J is the conduction current density (A/m^2) which is equal to the sum of hole and electron current densities:

$$J = J_p + J_n \tag{4.3.13}$$

$$\nabla.(\nabla \times H) = \nabla.J + \frac{\partial(\nabla.D)}{\partial t} \tag{4.3.14}$$

The term $\nabla.(\nabla \times H) = 0$ as there is no application of an external magnetic field. Hence, the above expression after using the expression in (4.3.2) becomes:

$$\nabla . J + \frac{\partial \rho}{\partial t} = 0 \tag{4.3.15}$$

The equation (4.3.15) gives the relationship between the charge density and conduction current density.

Under the assumption that the donor and acceptor concentrations are constant i.e. they do not vary with time, the terms $N_D \; and \; N_A$ in equation (4.3.9) becomes 0, using equations (4.3.9), (4.3.13) in equation (4.3.15):

$$\nabla . (J_p + J_n) + q \frac{\partial}{\partial t}(p - n) = 0 \tag{4.3.16}$$

The above equation can be split into two equations for electrons and holes:

$$\nabla . J_n - q \frac{\partial}{\partial t} n - q(R_n - G_n) = 0 \tag{4.3.17}$$

$$\nabla . J_p + q \frac{\partial}{\partial t} p + q\left(R_p - G_p\right) = 0 \tag{4.3.18}$$

Here R_n and R_p denotes the recombination rates and G_n and G_p describes the generation rates for electrons and holes respectively.

Therefore, the current continuity equations for the electrons becomes:

$$\nabla . J_n - q(R_n - G_n) = q \frac{\partial n}{\partial t}$$

$$\Rightarrow \quad \nabla . J_n - qR_n + qG_n = q \frac{\partial n}{\partial t}$$

$$\Rightarrow \quad \boxed{\boldsymbol{\frac{\partial n}{\partial t} = G_n - R_n + \frac{1}{q} \nabla . J_n}} \tag{4.3.19}$$

Similarly, the continuity equation for holes becomes:

$$\boxed{\boldsymbol{\frac{\partial p}{\partial t} = G_p - R_p - \frac{1}{q} \nabla . J_p}} \tag{4.3.20}$$

4.3.3 Drift - Diffusion Equation

The total current density in the semiconductor device consists of two components: drift current and diffusion current. Diffusion current arises from the movement of charge carriers due to non-uniform distribution of carriers within the semiconductor material. The movement of carriers is due to concentration gradient i.e. carriers move from regions of higher concentration to regions of lower concentration, a process which occurs without the application of any external field.

In contrast, drift current is generated by the movement of carriers under the influence of an external electric field. This type of current depends on both the mobility of charge carriers and the strength of applied electric field.

The current density for both types of carriers can be written as:

$$J_n = q\mu_n nE + qD_n \nabla n \tag{4.3.21}$$

$$J_p = q\mu_p pE - qD_p \nabla p \tag{4.3.22}$$

where, μ_n and μ_p are the mobilities of electrons and holes.

n and p are the electron and hole densities.

E is the applied electric field.

D_n and D_p are the electron and hole diffusion coefficients.

∇n and ∇p and the concentration gradient of electrons and holes.

The relationship between diffusion coefficients D and charge carrier mobilities μ is expressed by the Einstein relation as:

$$\frac{D_n}{\mu_n} = \frac{kT}{q}$$

and,

$$\frac{D_p}{\mu_p} = \frac{kT}{q} \tag{4.3.23}$$

4.4 Radiative Generation and Recombination Processes in Semiconductors

In semiconductor physics, the process of creation of free charge carriers, electrons or holes is known as generation. When an electron gets excited under the influence of thermal energy, external electric field or optical excitation and moves from the valence band (VB) to conduction band (CB), the free carriers are created in the process. The rate at which the generation of electrons and holes mechanism takes place in a semiconductor material is denoted by G_n and G_p respectively. When the excited electron jumps from valence band to conduction band, both the free electrons and holes are created in the mechanism. In other words, the rate of generation of electrons and holes are equal hence, the relation can be written as:

$$G_n = G_p = e_r \tag{4.4.1}$$

Here, e_r is the emission rate.

When an electron in the conduction band drops down to the valence band and recombines with a hole, it causes the release of either photons or heat with energy equivalent to the bandgap energy is known as recombination mechanism. Recombination is basically of two types: radiative and non-radiative. In radiative recombination, the movement of electron from CB to VB causes the release of a photon whose energy is same as that of the bandgap energy. However, in non-radiative recombination, the release of electron from CB to VB is accompanied by the release of heat. There are several factors contributing to non-radiative mechanisms which will be discussed in detail in the next section.

The rate at which the recombination occurs is proportional to the carrier concentrations of electrons (n) and holes (p) present in the conduction and valence bands respectively.

$$R \propto np \tag{4.4.2}$$

Since, the recombination process involves the equal contribution of both the electrons and holes, hence the recombination rate for both types of carriers is given by the relation:

$$R_n = R_p = Bnp \tag{4.4.3}$$

The net recombination rate of the carriers is the difference between the recombination rate and the generation rate of the carriers, which is given by the relation:

$$R = R_n - G_n = R_p - G_P = Bnp - e_r \tag{4.4.4}$$

At thermal equilibrium i.e. at room temperature under the influence of no applied external field, the generation rate of carriers is equal to the recombination rate of carriers. Thus, the above equation becomes:

$$Bn_0p_0 = e_r \tag{4.4.5}$$

Here, n_0 and p_0 are the electron and hole concentrations generated at thermal equilibrium. According to the mass action law, the relationship between carrier concentrations in an intrinsic semiconductor at thermal equilibrium is given as:

$$n_0 p_0 = n_i^2 \tag{4.4.6}$$

where n_i is the intrinsic concentration of carriers per unit volume in a semiconductor at room temperature.

Using equation (4.4.5), equation (4.4.4) can be rewritten as:

$$R = Bnp - Bn_0 p_0 \tag{4.4.7}$$

Under the application of an external electric field, the increment in the electron and hole concentrations in the material is denoted by Δn and Δp respectively. The net electron and hole concentrations in the medium becomes:

$$n = n_0 + \Delta n \tag{4.4.8a}$$

$$p = p_0 + \Delta p \tag{4.4.8b}$$

Substituting equation (4.4.8) in equation (4.4.7), we get:

$$R = B[(n_0 + \Delta n)(p_0 + \Delta p) - n_0 p_0]$$

$$\Rightarrow \qquad R = B[(n_0 p_0 + n_0 \Delta p + p_0 \Delta n + \Delta n \Delta p) - n_0 p_0]$$

Simplifying the above expression, we obtain:

$$R = B(n_0 \Delta p + p_0 \Delta n + \Delta n \Delta p)$$

Considering the case with low-level injection condition i.e. Δn, $\Delta p \ll (n_0 + p_0)$ and with an assumption that the injected number of electrons and holes are equal ($\Delta n = \Delta p$), the above expression becomes:

$$R = B(n_0 \Delta n + p_0 \Delta n + \Delta n^2)$$

$$\Rightarrow \qquad R = B(n_0 + p_0 + \Delta n)\Delta n \tag{4.4.9}$$

The radiative carrier lifetime is given as:

$$\tau = \frac{1}{B(n_0 + p_0 + \Delta n)} \tag{4.4.10}$$

The net recombination rate is written as:

$$R = \frac{\Delta n}{\tau} \tag{4.4.11}$$

For the case of high-level injection current, i.e. application of high values of external electric field, $\Delta n = \Delta p \gg (n_0 + p_0)$, the radiative recombination also known as spontaneous emission rate is given by the expression[53]:

$$\boldsymbol{R_{spon} = B(\Delta n)^2 \approx Bn^2} \tag{4.4.12}$$

with an assumption of neglecting the carriers generated at thermal equilibrium as they are very small compared to the injected carriers by the external force.

4.5 Non-Radiative Generation and Recombination Processes in Semiconductors

In semiconductors, the non-radiative recombination processes are the mechanisms where the electrons recombine with holes with no release of photons. Instead, the energy is released in the form of lattice vibrations, called as phonons. The energy can also be transferred to a third particle such as in Auger processes. These processes occur mainly due to defects in the crystal structures, impurities and other reasons. The non-radiative recombination mechanisms affect the overall efficiency and performance of the device. These processes also boost the degradation of devices. There are various types of non-radiative recombination processes, some of which are discussed in detail as follows:

4.5.1 Shockley-Read-Hall (SRH) Recombination

This process also called trap-assisted recombination, is the process in which recombination occurs through the defect energy levels present in the bandgap or forbidden region. These are called “trap” energy states which could either be introduced by defects or dopants. Instead of jumping directly to the valence band, the electron in the conduction band is captured by the trap energy level present in the bandgap region. There are two major processes: capture and escape, which occur with the carriers located in the trap energy state. Capture involves the trapping of electrons from CB or holes from VB at the trap energy level, Conversely, escape, or emission refers to the release of carriers from the trap state to the energy levels present in the CB (in the case of electrons) or VB (in case of holes).

The capture and escape processes in the carriers can be caused by absorption or emission of phonons. These processes for electrons and holes are explained as follows:

1) **Electron Capture:** The equation (4.4.3) can be modified to describe the capture process of electrons as:

$$R_{n\_SRH} = B_n n N_t (1 - f_t) \tag{4.5.1}$$

Here,
B_n: the electron trapping coefficient,
n: electron concentration
N_t: trap states density
f_t : the probability of occupation of trap states by electrons
$1 - f_t$: probability of absence of electrons in the trap energy states.

2) **Electron Escape/Emission:** The movement of electrons from the trap state to higher energy levels or the energy states present in the CB, equation (4.4.1) can be modified as:

$$G_{n\_SRH} = e_n N_t f_t \tag{4.5.2}$$

e_n: emission coefficient for electrons

3) **Hole Capture:** Similarly, the capture process for holes can be described as:

$$R_{p\_SRH} = B_p p N_t f_t \tag{4.5.3}$$

where,
p: hole concentration
B_p: trapping coefficient for holes

4) **Hole Escape/ Emission:** The hole emission process from the trap energy states can be expressed as:

$$G_{p\_SRH} = e_p N_t (1 - f_t) \tag{4.5.4}$$

where, e_p is the emission coefficient for holes

In thermal equilibrium conditions, the generation and recombination rates of electrons and holes are equal i.e. $R_{n\_SRH} - G_{n_{SRH}} = 0$ and $R_{p_{SRH}} - G_{p_{SRH}} = 0$ respectively.

By using the relations from (4.5.1) to (4.5.4),

$$B_n n N_t (1 - f_t) - e_n N_t f_t = 0$$

$$\Rightarrow \quad B_n n N_t - B_n n N_t f_t - e_n N_t f_t = 0$$

$$\Rightarrow \quad f_t = \frac{B_n n}{B_n n + e_n} \tag{4.5.5}$$

Similarly, simplifying the expressions for holes, we get:

$$B_p p N_t f_t - e_p N_t (1 - f_t) = 0$$

$$\Rightarrow \qquad B_p p N_t f_t - e_p N_t + e_n N_t f_t = 0$$

$$\Rightarrow \qquad f_t = \frac{e_p}{B_p p + e_p} \tag{4.5.6}$$

Equating equations (36) and (37), the final expression becomes:

$$\Rightarrow \qquad \frac{B_n n}{B_n n + e_n} = \frac{e_p}{B_p p + e_p}$$

$$\Rightarrow \qquad B_n B_p np - e_p e_n = 0 \tag{4.5.7}$$

In a steady-state condition, the net recombination rate of electrons is equal to that of holes. The expression becomes:

$$R_{SRH} = R_{n\_SRH} - G_{n_{SRH}} = R_{p_{SRH}} - G_{p_{SRH}} \tag{4.5.8}$$

$$B_n n N_t (1 - f_t) - e_n N_t f_t - B_p p N_t f_t + e_p N_t (1 - f_t) = 0$$

$$B_n n N_t - B_n n N_t f_t - e_n N_t f_t - B_p p N_t f_t + e_p N_t - e_p N_t f_t = 0$$

$$B_n n + e_p - f_t\left(B_n n + e_n + B_p p + e_p\right) = 0 \tag{4.5.9}$$

Since the right-hand side of the equations (4.5.7) and (4.5.9) are equal to 0, they can be equated to each other. Hence, the final expression for recombination rate due to SRH becomes:

$$R_{SRH} = \frac{B_n B_p np - e_p e_n}{B_n n + e_n + B_p p + e_p} N_t$$

Dividing numerator and denominator with $B_n B_p$ yields the expression:

$$R_{SRH} = \frac{np - \frac{e_p e_n}{B_p B_n}}{\frac{B_n n}{B_n B_p} + \frac{e_n}{B_n B_p} + \frac{B_p p}{B_n B_p} + \frac{e_p}{B_n B_p}} N_t$$

Substituting,

$n_1 = \frac{e_n}{B_n}$, $p_1 = \frac{e_p}{B_p}$ and $\tau_n = \frac{1}{B_n N_t}, \tau_p = \frac{1}{B_p N_t}$

The simplified expression becomes:

$$\boldsymbol{R_{SRH} = \frac{np - n_1 n_2}{\tau_p(n + n_1) + \tau_n(p + p_1)}} \tag{4.5.10}$$

4.5.2 Auger Recombination

In Auger processes, the energy released from the recombination of electron with hole is transferred to a third carrier present in the same or nearer energy level. The excited electron or hole then moves to a higher energy level within the same band. The carrier then loses its excess energy by phonons, a process known as thermalization. In this process, an electron-hole pair is destroyed with no photon release. This process is more pronounced in semiconductor materials with high concentration of carrier densities.

The recombination rate in electrons is given as:

$$R_{n\_Aug} = Cn^2p \tag{4.5.11}$$

where C_n is the Auger coefficient, np denotes the concentration of electron-hole pairs and n denotes the third carrier, in this case, an electron.

Similarly, the recombination rate for holes is given as:

$$R_{p\_Aug} = Cnp^2 \tag{4.5.12}$$

At high injection currents, under the condition when $n \gg n_i^2$ and $p \gg n_i^2$, the combined expression for Auger recombination rate is written as:

$$R_{Aug} = Cnp(n + p)$$

Assuming the total concentration of electrons after injection is equal to the concentration of holes, the final expression becomes:

$$\boldsymbol{R_{Aug} \cong Cn^3} \tag{4.5.13}$$

The total recombination rates arising from both the radiative and non-radiative mechanisms become:

$$R = R_{SRH} + R_{Spon} + R_{Aug}$$

The above expression can be expanded in terms of carrier concentrations and carrier lifetimes as:

$$R = An + Bn^2 + Cn^3 = \frac{n}{\tau(n)} \tag{4.5.14}$$

Here, $\tau(n)$ is the carrier lifetime, the inverse of which is the sum of the inverse of radiative and non-radiative carrier lifetimes.

$$\frac{1}{\tau(n)} = A + Bn + Cn^2 \tag{4.5.15}$$

where A, B, and C are the SRH, spontaneous emission and Auger coefficients with units $1/s$, cm^3/s and cm^6/s respectively.

The total carrier lifetime in terms of radiative and non-radiative lifetimes can be written as:

$$\frac{1}{\tau(n)} = \frac{1}{\tau_r(n)} + \frac{1}{\tau_{nr}(n)} \tag{4.5.16}$$

where,

$$\frac{1}{\tau_r(n)} = Bn \tag{4.5.17}$$

and

$$\frac{1}{\tau_{nr}(n)} = A + Cn^2 \tag{4.5.18}$$

The continuity equation for electrons in the case of quantum well structures is described as:

$$\nabla . J_n - q\left(R^{SRH} + R^{Spon} + R^{Auger} + R_n^{net,cap}\right) = 0 \tag{4.5.19}$$

and for holes, the equation becomes:

$$\nabla . J_p + q\left(R^{SRH} + R^{Spon} + R^{Auger} + R_p^{net,cap}\right) = 0 \tag{4.5.20}$$

Here, q is the charge of an electron, J_n and J_p represent the current densities of electrons and holes, respectively. R represents the recombination rate per unit volume and the superscripts denote the different recombination mechanisms: R^{SRH} for the Shockley-Read-Hall recombination, R^{Spon} means spontaneous recombination, R^{Auger} is the Auger recombination, $R_n^{net,cap}$ and $R_p^{net,cap}$ for the net capture rate of electrons and holes per unit volume in the quantum wells[54].

The capture/escape equations for electrons and holes in quantum-well structure is given as:

$$\nabla . J_n^{QW} - q\left(R_{QW}^{SRH} + R_{QW}^{Spon} + R_{QW}^{Auger} + R^{Stim} - \frac{1}{d_{QW}}\int_{QW} R_n^{net,cap}\, dw\right) = 0 \tag{4.5.21}$$

$$\nabla . J_p^{QW} + q\left(R_{QW}^{SRH} + R_{QW}^{Spon} + R_{QW}^{Auger} + R^{Stim} - \frac{1}{d_{QW}}\int_{QW} R_p^{net,cap}\, dw\right) = 0 \tag{4.5.22}$$

where d_{QW} is the width of quantum well layer. The subscript QW denotes the recombination rates per unit volume in the quantum well regions.

4.6 Gain Model of Harold

In semiconductor physics, the electronic band structure of a material is essential in explaining various physical properties, such as electronic, optical, thermal, and material characteristics. The band structure depends on internal factors, like carrier concentrations, crystal structure, defects, and external factors such as the mechanical strain, temperature, doping, electric field, and injection currents. Changes introduced in these factors alter the electronic properties of the material, which in turn, affects its optical properties and modifies the density of states and corresponding wave functionality of states[55]. This information of density of states is crucial in determining the characteristics and performance of the device. Therefore, gain models provide valuable insights into how different compositions and structures influence overall gain of the device, allowing predictions of key parameters like threshold current, emission wavelength, output power and other performance characteristics of the device. This understanding enhances the potential for optimizing device designs and, operating parameters, such as temperature and current density.

In Harold, two gain models are available to describe the material gain spectrum as a function of carrier concentration for Quantum well devices:

4.6.1 Parabolic gain model

In this model, the gain due to carrier transitions from conduction band to valence band is given by the expression:

$$\boldsymbol{g_{\gamma=0}(E_{phot}) = C_g M_0^2 \frac{1}{E_{phot}} \sum_{j,i} |C_{ij}|^2 A_{i,j}^{pol}(E_{phot}) \rho_{ij} [f_j(E_{phot}) - f_i(E_{phot})]} \quad (4.6.1)$$

The expression in equation (4.6.1) does not account for dispersion. The subscripts i and j represents the density of states in valence and conduction band respectively.
f_i and f_j represents the Fermi occupation factors in energy bands.
ρ_{ij} denotes the reduced density of states in the active region.
$A_{i,j}^{pol}$ is the anisotropy factor for dipole moment.
M_0 is the momentum matrix element.
E_{phot} is the emitted photon energy.
C_{ij} is the overlap integral of the energy states i and j. C_g stands for-

$$C_g = \gamma_g \frac{\pi q^2 \hbar}{\mu c \varepsilon_0 m_0}$$

To consider the gain broadening due to intra-band scattering, the overall gain is described by the convolution of the optical gain (in equation (4.6.1)) with line shape function denoted by the notation L[54].

$$g(E_{phot}) = g_{\gamma=0}(E_{phot}) \otimes L(E_{phot})$$
$$g(E_{phot}) = \int g_{\gamma=0}(E) L(E_{phot} - E) dE$$

A Lorentzian function with constant width is used as the line shape function which is given as:

$$L(x) = \frac{1}{\pi} \frac{\gamma}{\gamma^2 + x^2}$$

where $\gamma = \frac{\hbar}{\tau_{in}}$, τ_{in} stands for the intra-band relaxation time.

An important aspect of parabolic gain model in Harold is its consideration of anisotropic effective hole masses for confined carriers in QWell and confinement layers. Anisotropic effective mass means that the effective mass of carriers varies in different directions in the crystal material, providing valuable insights about the carrier dynamics in semiconductor materials with complex band structures. The parabolic gain model takes into account two directions when modelling effective hole masses:

a) *Parallel effective hole mass*, which applies to both light and heavy holes parallel to the heterojunction interface, this is used in computing the 2D density of states for confined carriers.
b) *Perpendicular effective hole mass*, represents light holes and heavy holes perpendicular to the heterojunction interface, essential for solving Schrodinger equation to locate confined holes in QWell structures.

This can be better understood by the following set of equations:

The effective hole mass for light and heavy holes in case of bulk materials is given as:

$$m_p^{3/2} = m_{lh}^{3/2} + m_{hh}^{3/2}$$

In case of QWell materials, the effective hole masses are described as:

$$m'_{lh,||} = m_{lh,||} w_{lh,||} + m_{lh,||}(1 - w_{lh,||})$$
$$m'_{hh,||} = m_{hh,||} w_{hh,||} + m_{hh,||}(1 - w_{hh,||})$$

where $w_{lh,||}$, $w_{hh,||}$ are the weighting factors for light holes and heavy holes and depend upon the type of materials.

4.6.2 k.p Model

The k.p model is an envelope approximation function which computes the optical gain of the QWell structures by solving the Schrodinger and Poisson equations. These equations are essential in predicting the charge carrier dynamics in confined dimensions such as in the case of QWells. The k.p model effectively describes the complex electronic band structure of various materials and analyzes band-to-band transitions, taking into account the coupling effects between the VB and CB. Coupling between energy bands is particularly crucial in narrow bandgap materials, and the structures where carriers are spatially confined, as confinement of carriers can alter the energy levels and significantly affect carrier dynamics. Accurate modelling of carrier dynamics is crucial to obtain precise band structures.

Similar to the parabolic gain model, the k.p model accounts for the anisotropic distribution of effective masses of electrons and holes across the crystal. However, unlike parabolic model, the k.p method considers the non-parabolic nature of the energy bands at higher energy levels.

In Harold, the k.p model has certain limitations and considers a few assumptions. For instance, it neglects the coupling effects between energy bands and assumes a zinc-blende crystal structure for simplicity[54]. The conduction band, being simpler to model, is computed with the parabolic gain model in Harold, while the valence band and other strain-dependent sub-bands such as light-holes (LH), heavy-holes (HH) and split-off (SO)- are modelled using the k.p approach.

The broadened gain for k.p method is described as:

$$g\left(E_{phot}\right) = C_g M_0^2 \frac{1}{E_{phot}} \frac{1}{\pi d_{act}} \sum_{j,i} \int k_{\|} dk_{\|} I_{ij}^{pol}(k_{\|}) L\left(E_{phot} - E(k_{\|})\right) \left[f_j\left(E_j(k_{\|})\right) - f_i\left(E_i(k_{\|})\right)\right] \quad (4.6.2)$$

Here, I_{ij}^{pol} is the overlap integral which depends on polarisation of the transition states i and j.
d_{act} is the width of active region which is the sum of thicknesses of different QWell layers.
$k_{\parallel}$ refers to the in-plane wavenumber.
E stands for photon energy.
E_{phot} is the energy of emitted photon.

4.7 Thermal model

The thermal model in Harold uses the heat flow equation across different layers of the device, represented as:

$$\nabla . J_h = w \tag{4.7.1}$$

where, J_h is the heat-induced current density, which depends on the thermal conductivity κ and device temperature T. This relationship is described as:

$$J_h = -\kappa \nabla T$$

The term w represents sources of heat generation, which includes Joule heating, non-radiative recombination processes, photon absorption by free carriers, Thomson heating, and other heating mechanisms arising from scattering and absorption of photons across the device facets. w can be written as:

$$w = w_{Joule} + w_{nr} + w_{fca} + w_{exc} \tag{4.7.2}$$

The heat generation by Joule heating mechanism varies with layer types and materials. The term w_{Joule} is the sum of Joule heating in substrate, metal, bulk, confinement, quantum well as well as contact regions of the device. The details of the expressions for each layer can be found in [54].

The generation of heat due to non-radiative recombination processes is described as:

$$w_{nr} = \left(R_{SRH} + R_{Aug}\right)\left[\left(E_{Fn} - E_{Fp}\right) + T\left(P_n + P_p\right)\right] \tag{4.7.3}$$

where, R_{SRH} and R_{Aug} are the non-radiative recombination mechanisms due to SRH and Auger processes.

E_{Fn} and E_{Fp} denotes the fermi-levels in n-type and p-type materials.

T is the temperature.

P_n and P_p represents the thermoelectric power values for electrons and holes respectively.

The loss of energy due to absorption of photon by free carriers in bulk, quantum well and confinement layers of the device is described as:

$$w_{fca} = \alpha_{fca}(y) f_T(y) S v_g \hbar\omega \tag{4.7.4}$$

where, $\alpha_{fca}(y)$ is the absorption coefficient.

$f_T(y)$ is the transverse distribution of photons in each eigenmode.

S is the photon density inside cavity.

v_g is the group velocity.

$\hbar\omega$ is the photon energy.

4.8 Harold-PICWave Link

Once the device structure is defined in Harold, model files such as epitaxial data (.swg), gain (.gain), material data (.mat), and spontaneous emission spectrum (.spon) are generated and then exported to PICWave. This enables the modelling of various physical processes, complex geometrical structures, and time-domain analysis of the device. The model files specifying the device characteristics are generated in Harold by running a 1D isothermal simulation with PICWave model as the execution mode. this generates material gain data as a function of carrier densities and temperatures for different sets of bias currents.

After completing simulations in Harold, the material data is fitted to be compatible with PICWave, allowing it to interpret the data correctly. This step is necessary because PICWave has certain assumptions and limitations; for example, it cannot distinguish between electrons and holes beyond general n-type and p-type doping. Additionally, it interprets different QWell layers in multi-QWell structures as identical in terms of doping. Another distinction is that PICWave employs a different default mode solver configuration as compared to Harold. Once this fitting is complete, the structure can be imported into PICWave. In PICWave, the epitaxial structure is pasted into the gain section, and other parameters such as central wavelength for simulation i.e. *lambdaCentre*, device discretization along the cavity axis i.e. *zStep* are specified according to the recommended values from Harold. Not adhering to Harold's recommendations may cause simulation failures and generate errors.

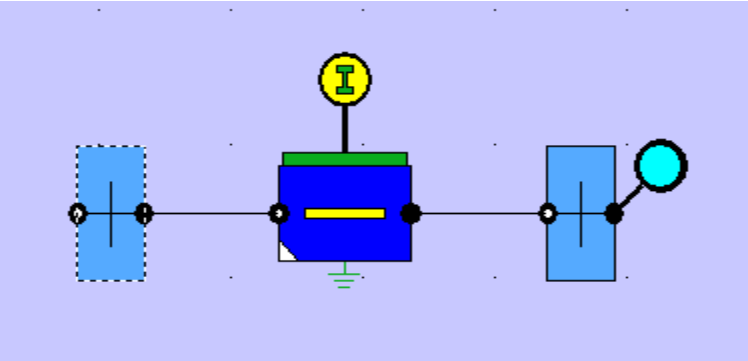

Figure 29: Gain section with two facets in PICWave

PICWave uses a Wide band gain fitter tool to fit the imported gain data from Harold. As a result, it produces a gain model as a function of wavelength for a wide range of carrier densities and temperatures. Additionally, it also contains the capabilities of modelling wide free-spectral ranges and spatial hole burning.

The gain spectrum can be also be defined with parabolic gain model in PICWave depending on the gain export method specified in Harold. The parabolic gain model uses the following expression to produce gain results:

$$g(N,\lambda,T) = g_0(N,T) - G_0 N_0 g_2(N,T).\left(\lambda - \lambda_{pk}(N,T)\right)^2 \qquad (4.8.1)$$

where g_0, G_0 and N_0 are the differential gain, carrier density at transparency values which are the functions of material. These parameters are defined in the material directory.

Parabolic gain model generates material gain closer to the gain peak. The gain spectrum for this model is characterized by three parameters:

1) The peak gain (g_0)
2) Gain peak wavelength (λ_{pk})
3) Curvature of the spectrum at the gain peak (defined by g_2 parameter)

4.9 GaAs-Based Multi-Quantum Well Laser Structure Simulations with Harold and PICWave

The GaAs substrate-based multi-QWell laser structure presented in this section was implemented in Harold. The model was then exported to PICWave, which converts the frequency-domain gain spectrum into discrete time-domain results. PICWave applies the travelling wave with a slowly varying envelope approximation model to generate time-domain results of the laser structure. Due

to the conversion of frequency domain gain spectrum into its time-domain equivalence, the gain spectrum results produced by PICWave are periodic and continuous, as demonstrated in the attached results in Figure 30. PICWave employs a wide-band active fitter model to compute the imported gain data from Harold, which is then subsequently compared with the gain spectrum imported from another simulation tool, Crosslight.

Crosslight is a simulation tool which can model complex structures such as QDots and QDashes in the active medium. However, for a fair comparison ("an apple-to-apple comparison"), the laser structure implemented in Harold and Crosslight was based on QWell designs. One of the key features in Crosslight is a QDot and QDash gain model, based on the k.p method. The software uses more detailed physics to describe the characteristics of the device. However, the software has some challenges such as it is tough to use, is riddled with bugs, is expensive, and is no longer accessible through CMC Microsystems.

In contrast, Harold, along with its built-in HaroldXY tool, and PICWave can simulate a broader range of lasers, including mode-locked lasers. These tools support bulk and QWell lasers and are expected to support QDot gain models using the k.p method in the future. Moreover, Harold and PICWave are far more user-friendly, well-supported, and affordable than Crosslight. A more detailed comparison about both tools is discussed in the 'Material gain section' mentioned below.

The epitaxial structure of the multi-quantum well structure simulated in Harold is presented in the Table 4:

Layers	**Material**	**Thickness (μm)**	**x-Mole fraction**	**Doping type**	**Concentrations (cm^{-3})**
Metal contact	Gold	2			
Capping	GaAs	0.15		p	$1e+20$
p- cladding	InGa(x)P	0.9	0.51	p	$3e+18$
p- barrier	InGa(x)P	0.1	0.51	p	$1e+18$
p-confinement	GaAs	0.65		p	$1e+17$
QWell-1	In(x)GaAs	0.008	0.4		
Confinement-1	GaAs	0.01			
QWell-2	In(x)GaAs	0.008	0.4		
Confinement-2	GaAs	0.01			
QWell-3	In(x)GaAs	0.008	0.4		
n-Confinement	GaAs	0.65		n	$1e+17$

n- Barrier	InGa(x)P	0.1	0.51	n	$1e+18$
n- cladding	InGa(x)P	0.9	0.51	n	$3e+18$
Substrate	GaAs	0.5		n	$4e+18$
Metal contact	Gold	2			

Table 4: Epitaxial structure description

The .gain data from Harold looks like the ones attached in Figure 32. The gain file contains the gain information in the format:

$m\lambda$	λ_{min}	λ_{max}	nT	$minT$	$maxT$	$poln$
$nN(T_1)$						
$N_1(T_1)$		$N_2(T_1)$		$N_n(T_1)$		
gain (N_1, T_1, λ_1)		gain (N_2, T_1, λ_1)	$\cdots$	gain (N_n, T_1, λ_1)		
gain (N_1, T_1, λ_2)		gain (N_2, T_1, λ_2)	$\cdots$	gain (N_n, T_1, λ_2)		
$\vdots$						
gain (N_1, T_1, λ_m)		gain (N_2, T_1, λ_m)	$\cdots$	gain (N_n, T_1, λ_m)		

The parameters λ_{min} and λ_{max} defines the minimum and maximum wavelength values for which the gain spectra are generated, nT signifies the number of temperatures and $minT$and $maxT$ specifies the temperature range. The parameter $poln$ signifies the polarization. If $poln = 1$, the spectra are provided for TE polarization and if $poln = 2$, the spectra are provided for TM.

Each element in the matrix contains the gain spectra corresponding to the carrier densities specified in the first row of the matrix for a given temperature T. The parameter $m\lambda$ decides the number of rows of the matrix, which specifies the gain obtained with each wavelength increment.

The number of columns in the matrix is decided by the current increment specified in Harold's settings. Each column corresponds to the gain values for a different carrier density, whereas each row represents the gain value for a different wavelength. When $nT > 1$ i.e., when multiple temperatures are specified, another set of gain values is generated in the same structure for each temperature value. Thus, the matrix data represents the gain spectra as a function of carrier densities, wavelengths, and temperatures.

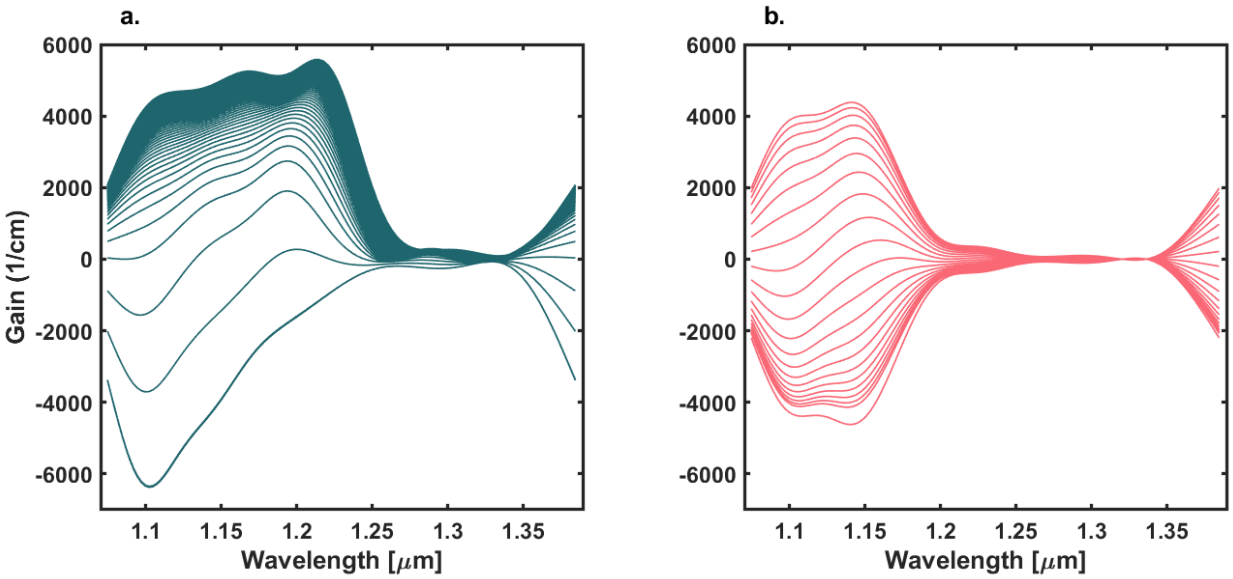

Figure 30: The 3-Quantum well gain spectra from: a) Harold in PICWave, and b) Crosslight in PICWave, for $I = 500\ mA$ and $T = 25℃$.

Figure 31: Image depicting the Layer editor interface in Harold v7.0.1.

```
<negainspectrum(1,1)>
301 0.9 1.39834 1 25 25 1  // nLambda lambdaMin[um] lambdaMax[um] nT minT[C] maxT[C] poln(1=TE,2=TM)

 //T=25 [C]
21 //nN
  4.026841e+15   4.947129e+17   2.135597e+18   2.623586e+18   3.395211e+18   3.960120e+18   4.431436e+18   4.838664e+18   5.199192e+18
 -1.220040e+04  -1.194504e+04  -1.133547e+04  -1.113443e+04  -1.076136e+04  -1.045202e+04  -1.016218e+04  -9.885159e+03  -9.614696e+03
 -1.221829e+04  -1.195966e+04  -1.133993e+04  -1.113326e+04  -1.074902e+04  -1.043169e+04  -1.013505e+04  -9.851567e+03  -9.574198e+03
 -1.223581e+04  -1.197471e+04  -1.134452e+04  -1.113299e+04  -1.073699e+04  -1.040982e+04  -1.010421e+04  -9.812397e+03  -9.526834e+03
 -1.225313e+04  -1.198997e+04  -1.134842e+04  -1.113252e+04  -1.072557e+04  -1.038810e+04  -1.007238e+04  -9.770784e+03  -9.475613e+03
 -1.227051e+04  -1.200512e+04  -1.135162e+04  -1.113115e+04  -1.071380e+04  -1.036640e+04  -1.004035e+04  -9.728339e+03  -9.422702e+03
 -1.228806e+04  -1.202009e+04  -1.135446e+04  -1.112893e+04  -1.070079e+04  -1.034368e+04  -1.000751e+04  -9.685000e+03  -9.368549e+03
 -1.230577e+04  -1.203474e+04  -1.135731e+04  -1.112620e+04  -1.068646e+04  -1.031927e+04  -9.972848e+03  -9.639820e+03  -9.312449e+03
 -1.232356e+04  -1.204877e+04  -1.136019e+04  -1.112332e+04  -1.067103e+04  -1.029313e+04  -9.935991e+03  -9.592086e+03  -9.253515e+03
 -1.234136e+04  -1.206233e+04  -1.136276e+04  -1.112022e+04  -1.065488e+04  -1.026554e+04  -9.897037e+03  -9.541708e+03  -9.191458e+03
 -1.235911e+04  -1.207585e+04  -1.136480e+04  -1.111655e+04  -1.063805e+04  -1.023678e+04  -9.856248e+03  -9.488848e+03  -9.126336e+03
 -1.237656e+04  -1.208976e+04  -1.136628e+04  -1.111215e+04  -1.062021e+04  -1.020678e+04  -9.813764e+03  -9.433710e+03  -9.058330e+03
 -1.239347e+04  -1.210416e+04  -1.136693e+04  -1.110693e+04  -1.060116e+04  -1.017518e+04  -9.769357e+03  -9.376228e+03  -8.987477e+03
 -1.240961e+04  -1.211870e+04  -1.136657e+04  -1.110062e+04  -1.058083e+04  -1.014174e+04  -9.722675e+03  -9.316064e+03  -8.913517e+03
 -1.242474e+04  -1.213301e+04  -1.136545e+04  -1.109302e+04  -1.055873e+04  -1.010645e+04  -9.673573e+03  -9.252975e+03  -8.836142e+03
 -1.243854e+04  -1.214693e+04  -1.136397e+04  -1.108446e+04  -1.053493e+04  -1.006904e+04  -9.622210e+03  -9.186848e+03  -8.755215e+03
 -1.245039e+04  -1.216038e+04  -1.136249e+04  -1.107533e+04  -1.050945e+04  -1.002918e+04  -9.567674e+03  -9.117489e+03  -8.670753e+03
 -1.245929e+04  -1.217319e+04  -1.136094e+04  -1.106593e+04  -1.048260e+04  -9.987108e+03  -9.510220e+03  -9.044673e+03  -8.582451e+03
 -1.246362e+04  -1.218512e+04  -1.135890e+04  -1.105613e+04  -1.045470e+04  -9.943118e+03  -9.450036e+03  -8.968422e+03  -8.490117e+03
 -1.246130e+04  -1.219590e+04  -1.135606e+04  -1.104551e+04  -1.042573e+04  -9.897397e+03  -9.387330e+03  -8.888899e+03  -8.393857e+03
 -1.245076e+04  -1.220525e+04  -1.135232e+04  -1.103379e+04  -1.039533e+04  -9.849844e+03  -9.322166e+03  -8.806210e+03  -8.293771e+03
 -1.243207e+04  -1.221270e+04  -1.134755e+04  -1.102085e+04  -1.036315e+04  -9.800074e+03  -9.254311e+03  -8.720265e+03  -8.189844e+03
 -1.240756e+04  -1.221739e+04  -1.134159e+04  -1.100658e+04  -1.032904e+04  -9.747795e+03  -9.183408e+03  -8.630755e+03  -8.081862e+03
 -1.238112e+04  -1.221782e+04  -1.133419e+04  -1.099080e+04  -1.029288e+04  -9.692871e+03  -9.109249e+03  -8.537415e+03  -7.969557e+03
 -1.235627e+04  -1.221158e+04  -1.132510e+04  -1.097327e+04  -1.025453e+04  -9.635177e+03  -9.031713e+03  -8.440109e+03  -7.852783e+03
 -1.233493e+04  -1.219590e+04  -1.131405e+04  -1.095376e+04  -1.021378e+04  -9.574562e+03  -8.950671e+03  -8.338730e+03  -7.731454e+03
 -1.231827e+04  -1.216941e+04  -1.130066e+04  -1.093202e+04  -1.017042e+04  -9.510840e+03  -8.865975e+03  -8.233162e+03  -7.605495e+03
 -1.230716e+04  -1.213383e+04  -1.128393e+04  -1.090752e+04  -1.012429e+04  -9.443821e+03  -8.777454e+03  -8.123277e+03  -7.474829e+03
 -1.230148e+04  -1.209463e+04  -1.126271e+04  -1.087974e+04  -1.007472e+04  -9.373334e+03  -8.684962e+03  -8.008953e+03  -7.339384e+03
 -1.230009e+04  -1.205904e+04  -1.123476e+04  -1.084726e+04  -1.002194e+04  -9.299253e+03  -8.588364e+03  -7.890096e+03  -7.199116e+03
 -1.230167e+04  -1.203182e+04  -1.119763e+04  -1.080813e+04  -9.964868e+03  -9.221012e+03  -8.487533e+03  -7.766588e+03  -7.053998e+03
 -1.230514e+04  -1.201338e+04  -1.115021e+04  -1.076018e+04  -9.902242e+03  -9.138075e+03  -8.381928e+03  -7.638286e+03  -6.903969e+03
```

Figure 32: Gain spectra information generated by Harold.

The material gain spectra depicted in Figure 30, demonstrate the variation in gain peaks for different injection currents. This variation in gain is influenced by various material properties, such as the carrier density, energy band structure, and the composition of the device.

In Figure 30, the material exhibits maximum gain within $1100 - 1200\ \mu m$ wavelength range, whereas the results from the Crosslight simulation tool depict the maximum material gain within the $1100 - 1150\ \mu m$ range. The reason for this discrepancy between the two simulation tools is primarily due to the different computational models used by the tools and some approximations considered in Harold. These will be discussed in detail in the following section.

4.10 Results and Discussions

In this chapter, two simulation platforms, Harold and PICWave, are discussed in detail, highlighting their capabilities, limitations and functionalities. The chapter explores the simulation process within the tools and discusses some crucial equations and models including the gain, and thermal models. By using the export and import functionalities of Harold and PICWave, gain data for the same laser structure from Harold and other simulation platform, Crosslight, were integrated in PICWave for comparison. The resulting gain spectra results for 3-Quantum wells GaAs based substrate are presented in Figure 30.

The gain spectra shown in Figure 30(a) represents the output from Harold, showing the maximum gain peak of 6000 cm^{-1} at the wavelength of 1210 μm. However, the results displayed in Figure 30(b) is based on the gain spectra from Crosslight where the maximum gain peak is observed at a wavelength of 1150 μm with a material gain of 4000 cm^{-1}. This discrepancy in results occurs due to the significant differences in the underlying physics and computational models used by each tool, as discussed below:

1) Harold employs the Schrodinger equation to calculate confined energy states, which are then used to compute the material gain of the device. It incorporates effects like bandgap narrowing effects and quantum well transitions in its computation. On the other hand, Crosslight uses k.p method to calculate the material gain, which takes into account many-body interactions, providing a more detailed representation of the gain spectra at higher carrier densities.

2) Harold uses some approximations to simplify higher-order many-body interactions whereas Crosslight provides more detailed and accurate, especially in high density scenarios gain spectra results by including strain and birefringence effects.

Although the device structure and other simulation conditions were kept constant in both Harold and Crosslight, the significant differences in their approaches in computing gain results in these varying spectra[54],[56].

It is also observed that for the carrier density of $N = 4.03 \times 10^{15}$ (cm^{-3}) in Figure 32, population inversion is not achieved, resulting in a negative gain peak $(g < 0)$ at lower injection currents, as seen in Figure 30. This depicts that there is more net absorption in the device than amplification at specific wavelengths, preventing the laser from operating in lasing mode. However, as the injection current increases, the carrier density increases i.e. $N > 2.62 \times 10^{18}$, and gain becomes positive $(g > 0)$. This transition signifies that there is more amplification than net absorption in the laser cavity, enabling the device to achieve lasing[40].

CHAPTER 5
Experimental Analysis of Quantum Dash Lasers

5.1 Introduction

While the numerical modelling and simulations discussed in the previous chapters provides a theoretical aspect of the mode-locking mechanism, the experimental analysis provides a practical perspective on the characteristics, properties, and performance of the laser device. This experimental approach is crucial for evaluating its quality and operational efficiency in real-world. By conducting a set of experiments and measurements, the behaviour of laser under various conditions is analyzed. The data obtained from these experiments and measurements provides valuable insights into the device's performance and parameters.

In this chapter, we discuss the experimental investigation of Quantum Dash laser structures, focussing on the impact of injection current (or bias current) and temperature on their performance. These experiments were conducted at the National Research Council of Canada (NRC) campus in Ottawa. The work was carried out collaboratively by myself and Narmada Rajaram, with Dr. Chun-ying Song, Dr. Jiaren Liu and Dr. Zhenguo Lu as our supervisors. The results were analyzed and thoroughly reviewed by the experts from NRC and the University of Ottawa.

The chapter is structured as follows: the first section presents the Light-Current characteristics, detailing the relationship between injection current and emitted power. The second section explores spectral measurements to understand the wavelength-dependent behaviour of the device. In the third section, we describe the RF testing to assess the mode-locking performance of lasers for different injection currents and temperatures. Although RF tests could not be completed for all the planned temperatures due to time constraints. However, an intriguing phenomenon was

observed during the measurements which will be discussed in detail in section 5.5. Finally, the last section covers dispersion measurements conducted on a different sample.

5.2 Objective and Workflow

The primary goal of the project was to investigate the influence of temperature and injection current on the mode-locking performance in Quantum Dash laser devices. A systematic workflow was followed to achieve this objective:

1) Light-Current (L-I) characteristics were recorded at different temperatures.
2) Optical comb spectra were recorded to understand the wavelength-dependent behaviour of the laser device.
3) RF measurements were conducted at various injection currents, keeping the temperature fixed at 25℃.
4) Dispersion measurements were performed on another QDash bar sample.

5.3 Light-Current (L-I) characteristics

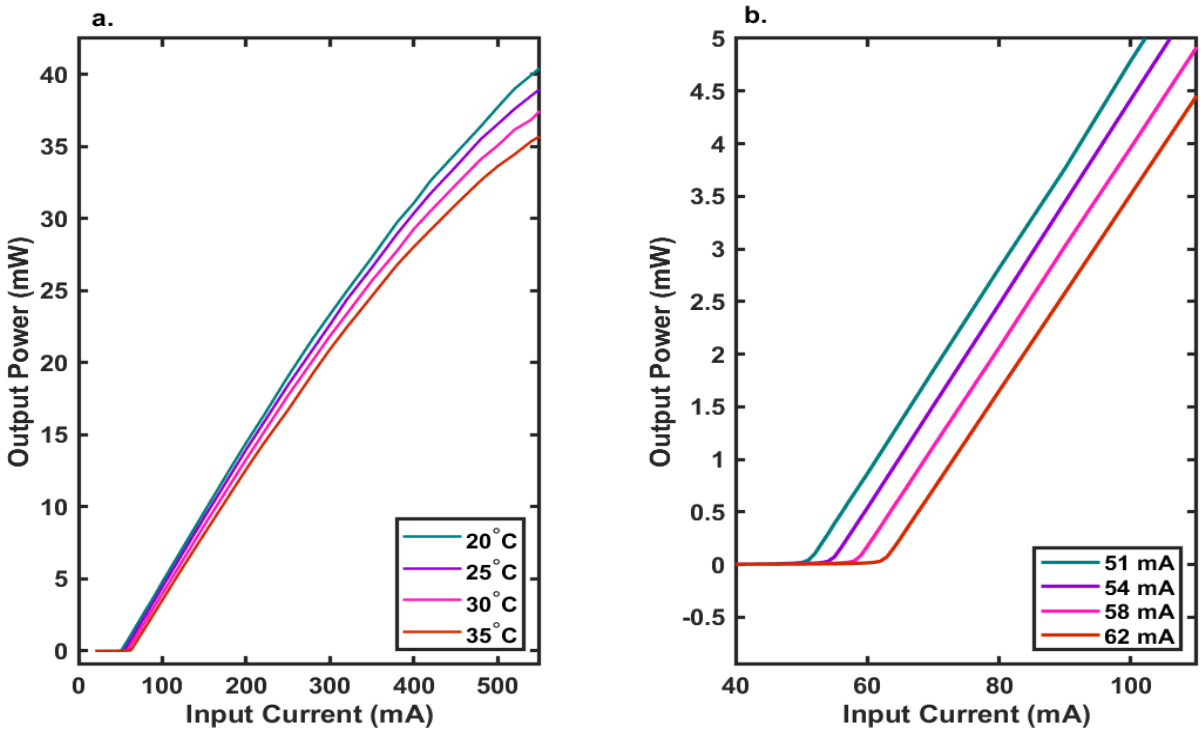

Figure 33: a) L-I curves recorded for different temperatures. Image b) highlights the threshold currents for various temperatures.

The Light-Intensity curves discussed in this section are based on the ridge waveguide structured 5-layer Quantum Dash laser sample with cavity length 1500 μm and strip width of 2.3 μm. The emission wavelength for the chip-on carrier packaged laser sample under test is 1550 nm. The laser sample discussed in this thesis is designed to cater to its application in data communication systems. Figure 34 represents the overall measurement setup while recording the L-I curves.

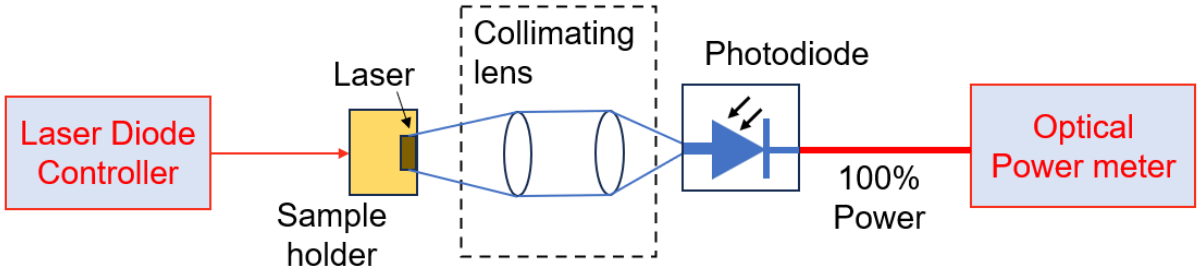

Figure 34: Measurement setup for L-I curves

Working Principle of TEC Controller instrument:

The acronym TEC stands for Thermo-Electric Cooler which operates based on the **Peltier effect**. This phenomenon creates a temperature difference by applying voltage across the two electrodes connected to the semiconductor sample. The resulting temperature gradient created in the material causes charge carriers to diffuse from the high-temperature region to the low-temperature region. This effect is utilized in various applications including electricity generation, temperature measurement, and maintaining or altering the temperature of objects.

In optical systems, TEC controller offers several advantages:

1) Lasers are highly sensitive devices to temperature which can significantly affect their performance. Parameters such as threshold current, wavelength stability, slope efficiency and output power can vary with slight temperature difference. Therefore, maintaining the operational conditions of laser such as temperature and input current to a precisely accurate value are necessary to ensure its optimal performance. Thus, TEC controller offers precise control over the parameters.
2) Lasers usually operate over specific wavelengths in various applications. With the temperature stability offered by TEC, the lasing wavelength of laser is maintained to a desirable value.

The temperature-sensing device in TEC is a thermistor. The thermistor senses the real-time temperature of the module, and the difference between the set temperature and actual temperature produces the temperature error. This error adjusts the temperatures by converting the temperature error to voltage. The thermistor is positioned close to the laser module to ensure the temperature

readings gives accurate readings of the laser's actual temperature. The detailed working principle of the instrument can be found in reference [57].

5.3.1 Measurement Setup

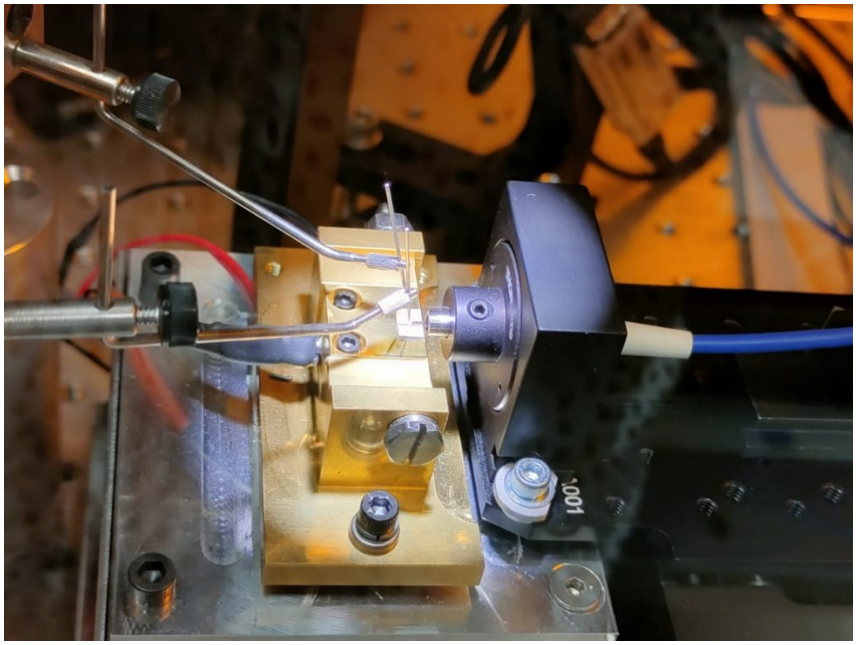

Figure 35: Image illustrating the laser sample placed on the sample holder and collimating lens

The laser module consists of the laser sample mounted on a gold sample holder. Two probes from above make contact with the device. The device is manually placed on the sample mount following which the manual positioning of probes on top of the sample. The injection current and the temperature for the measurements are set using the ILX Lightwave LDC 3744C Laser Diode Controller. This controller combines a precise laser diode current source with a TEC temperature controller. The injection current is adjusted via the current source, while the TEC temperature controller manages the temperature to ensure stable thermal conditions[58].

Once the operating conditions for the laser device are specified, the system is left undisturbed for a few minutes to stabilize. The light output is then collected by the collimating lens mounted on a NanoMax 300 flexure stage. Since the laser device under test is an edge-emitting light source, the emitted light diverges from the facet surface. The collimating lens collects this diverged light and converts it into a parallel beam. The curvature and material of the lens ensure that the light emerges in a consistent direction. The lens must be precisely aligned with the laser source to achieve optimal performance. The flexure stage is a three-axis stage that allows the lens position to be fine-tuned in all x,y, and z axes. This ensures precise alignment, maximizing the light captured from the source. The flexure stage's movement is controlled by piezoelectric actuators, which allow the travel of up to 20 μm and can be operated manually or through a LabVIEW-coded program[59].

These actuators stabilize the stage in a fixed piezo-position, maintaining alignment throughout the measurement process.

After collimation, the light is transferred to an InGaAs photodiode equipped with an S120 FC/PC fiber adapter cap. The photodiode, operating on the principle of the photoelectric effect, converts the incoming photons into electrical energy. This energy is then fed into the Thorlabs Optical Power and Energy meter which measures and displays the output power[60]. The bias current supplied to the laser sample under test is adjusted manually, and the power is recorded for each bias current setting. This method helps to minimize heating effects, ensuring accurate measurements.

Using the above arrangement, the L-I curves were recorded for four temperatures $(20 - 35℃)$. According to the results, the threshold current increases with an increase in temperature and the threshold current obtained at each temperature is displayed in Figure 33b.

5.3.2 Slope of L-I Curves

The information on the slope of L-I curves for the laser device is crucial in determining the external differential quantum efficiency of the device[61]. It is measured above the threshold current value I_{th} and is denoted as $\Delta P/\Delta I$.

$$\text{Slope for } T = 20℃, \frac{\Delta P}{\Delta I} = \frac{(19.06-14.44)mW}{(250-200)mA} = \frac{4.62}{50} = 0.0924\ W/A$$

$$\text{Slope for } T = 25℃, \frac{\Delta P}{\Delta I} = \frac{(18.46-13.97)mW}{(250-200)mA} = \frac{4.49}{50} = 0.0898\ W/A$$

$$\text{Slope for } T = 30℃, \frac{\Delta P}{\Delta I} = \frac{(17.73-13.3)mW}{(250-200)mA} = \frac{4.43}{50} = 0.0886\ W/A$$

$$\text{Slope for } T = 35℃, \frac{\Delta P}{\Delta I} = \frac{(16.72-12.6)mW}{(250-200)mA} = \frac{4.12}{50} = 0.0824\ W/A$$

5.3.3 External Differential Quantum Efficiency

It indicates the efficiency of converting the input electrical charges i.e. electron-hole pairs to the output light produced i.e. photons emitted from the laser device. This parameter is a function of geometrical parameters like the device's cavity length and strip width[61]. It is denoted as η_d.

The external differential quantum efficiency, η_d is expressed as:

$$\eta_d = \frac{\left(\frac{\Delta P}{\Delta I}\right)}{\left(\frac{hc}{q\lambda}\right)} \tag{5.3.1}$$

Here, $\frac{\Delta P}{\Delta I}$ is the slope of L-I curves.

h is the Planck's constant given as $6.6262 \times 10^{-34}\, J.sec$.

q is the electric charge, $1.6022 \times 10^{-19}\, C$.

c is the speed of light, $2.99 \times 10^{8}\, m/s$.

λ is the emitted wavelength from the device, $1550\, nm$.

$$\eta_d\ (T = 20°C) = \frac{0.0924\ \left(\frac{W}{A}\right) \times 1.6022 \times 10^{-19} \times 1550 \times 10^{-9} (C.m)}{6.6262 \times 10^{-34} \times 2.99 \times 10^{8}\ \left(Jsec.\frac{m}{s}\right)}$$

$$\boldsymbol{\eta_d\ (T = 20°C) = 0.1158 = 11.58\ \%}$$

Similarly for other temperatures, η_d is obtained as:

$$\boldsymbol{\eta_d\ (T = 25°C) = 0.1126 = 11.26\ \%}$$

$$\boldsymbol{\eta_d\ (T = 30°C) = 0.1111 = 11.11\ \%}$$

$$\boldsymbol{\eta_d\ (T = 35°C) = 0.1033 = 10.33\ \%}$$

Conclusion: The efficiency of converting injected charge carriers to output photons decreases with an increase in temperature when compared to the same injection currents.

5.4 Optical Spectral Measurements

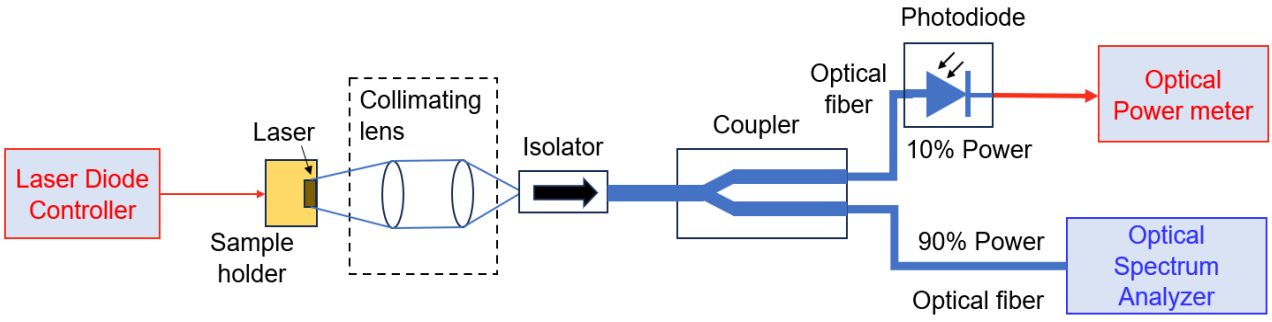

Figure 36: Block diagram representing measurement setup for RF test.
Red indicates the electrical signals, and blue indicates the optical signals.

Figure 36 describes the setup used to obtain the optical spectra for the device consists of an isolator following the collimating lens, to avoid any parasitic reflection to the device. However, some power loss is experienced by the light within the isolator. The isolation provided by the isolator is around $-52dB$. Following the isolator is a fiber coupler which couples 90% of light into the ANDO AQ6317B optical spectrum analyzer (OSA) via an optical fiber. The remaining 10% of light is fed into the power meter via a photodetector. The OSA provides power spectral density (dBm) as a function of wavelength (nm).

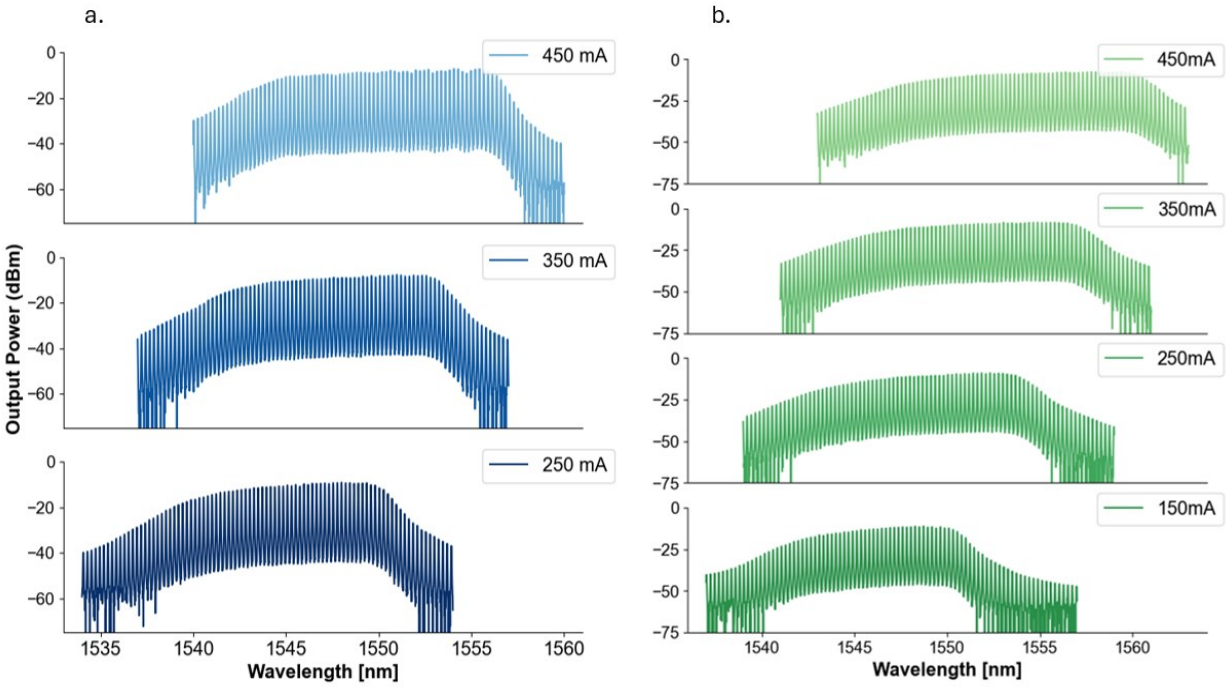

Figure 37: Optical Spectra for various injection currents recorded at a) 22℃ *and b)* 30℃

The optical spectra of the laser device were recorded for two temperatures ($22\ and\ 30℃$) for different injection currents. The results and observations recorded for the results are discussed in Table 5.

Two parameters are included in this set of measurements. First, the objective was to observe the change in the spectra with temperature change. Second, the aim was to observe the change in the spectrum by keeping the temperature fixed to one value and varying the injection currents. The changes introduced in the parameters are presented in the Table 5 following the conclusions observed.

From the results, with an increase in injection current, the optical spectrum shifts towards the longer wavelength. The temporal width i.e. $-3dB$ width of the envelope of spectral lines and peak power are discussed for each of the spectrum recorded at different injection currents.

a.

Injection Current (mA)	Peak Power (dBm)	Peak Power wavelength (nm)	Centre Wavelength (nm)	Temporal Width at $-3dB$ (nm)
250	−14.080	1550.498	1544	9.080
350	−7.727	1550.977	1547	10.2
450	−7.103	1554.057	1550	12.080

b.

Injection Current (mA)	Peak Power (dBm)	Peak Power wavelength (nm)	Centre Wavelength (nm)	Temporal Width at $-3dB$ (nm)
150	−11.114	1548.726	1547	7.040
250	−8.967	1552.317	1549	9.120
350	−8.357	1553.036	1551	10.080
450	−7.683	1557.780	1553	11.280

Table 5: a) Depicts the Parameter values for different injection currents at 22℃ *and b)* 30℃.

The results indicate that the peak power and temporal width of the device increase as the injection current increments. A more detailed discussion, exploring the potential explanations for this behaviour is presented in the Results and Discussions section (5.7) at the end of the chapter.

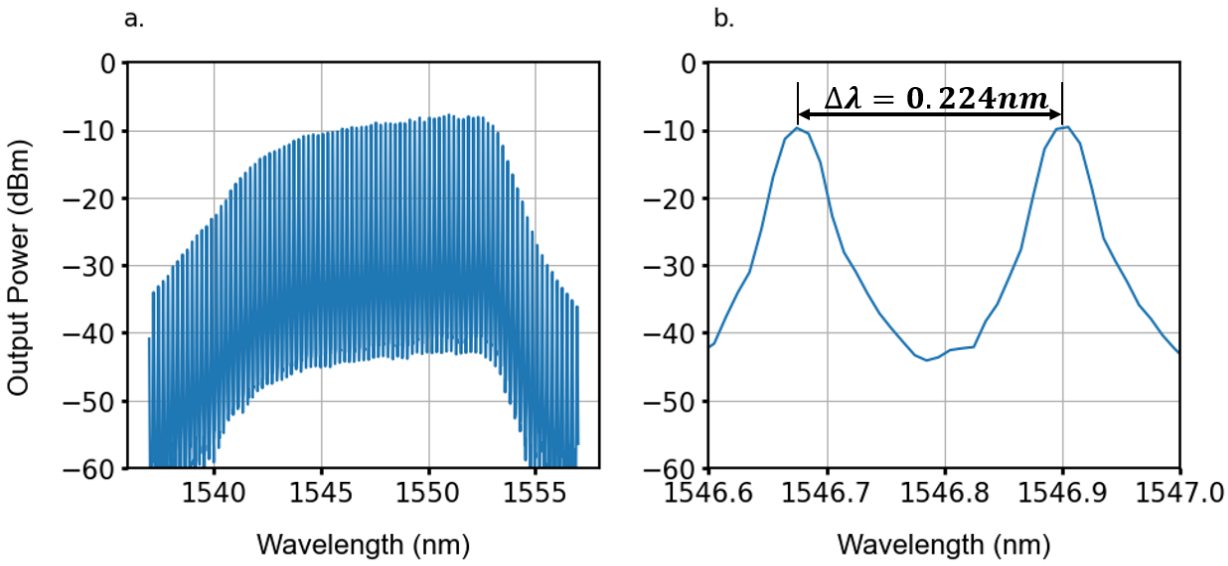

Figure 38: a) Optical comb spectrum at $T = 22^{o}C$ and $I = 350\ mA$. b) $\Delta\lambda$ denotes line spacing between two adjacent longitudinal modes. The optical spectrum is for the Quantum Dash active layer laser device.

$$\Delta\lambda = \frac{\lambda^2}{2n_g(\lambda)l} \tag{5.4.1}$$

where $\Delta\lambda$ is the line spacing (nm) between two successive modes.

λ is the central wavelength (nm) of the spectrum shown in Figure 38.

$n_g(\lambda)$ is the group index (dimensionless) which is a function of wavelength.

l denotes the cavity length of the device (μm).

Factor 2 represents the round-trip cavity length i.e. $L = 2l$.

Substituting the values in equation (1), we obtain the value of the group index as-

$$n_g(\lambda) = \frac{(1547)^2\ (nm)^2}{0.224(nm) \times 2 \times 1500(\mu m)}$$

$$\Rightarrow \quad \boxed{\boldsymbol{n_g(\lambda) = 3.561}}$$

Since the laser device under test is a mode-locked laser, the beating frequency of the individual mode or the pulse repetition rate of the device is obtained as:

$$f = \frac{c}{\lambda} = 193.92\ THz \tag{5.4.2}$$

$$\Delta f_{FSR} = \frac{\Delta\lambda}{\lambda} \times f \tag{5.4.3}$$

$$\Rightarrow \quad \Delta f_{FSR} = \frac{0.224(nm)}{1547(nm)} \times 193.92(THz) = 28.08$$

$$\Rightarrow \quad \boxed{\Delta \boldsymbol{f_{FSR}} \cong \mathbf{28\ GHz}} \tag{5.4.4}$$

The **beating frequency of the individual mode** is approximately $28\ GHz$.

The **cavity round-trip time $\boldsymbol{\tau}$** is given as:

$$\boxed{\boldsymbol{\tau} = \frac{\mathbf{1}}{\Delta \boldsymbol{f_{FSR}}} = \mathbf{35.7\ ps}} \tag{5.4.5}$$

The temporal width or the spectral width of the optical comb spectrum depicted in Figure 38 is $10.2\ nm$. It is defined as the band of frequencies that the resonant cavity of the laser device allows to oscillate within the cavity.

The expression in equation (5.4.2) can be written in terms of the frequency and wavelength of the envelope of comb spectrum as:

$$\Delta f_{envelope} = \frac{\Delta\lambda_{envelope}}{\lambda} \times f \tag{5.4.6}$$

where $\Delta f_{envelope}$ is the frequency of the envelope of the comb spectrum.

$\Delta\lambda_{envelope}$ is the spectral or temporal width of the comb spectrum.

λ is the central wavelength of the spectrum displayed in Figure 38b)

f is the frequency of the spectrum.

Substituting the values in equation (5.4.6),

$$\Delta f_{envelope} = \frac{10.2}{1547} \times 193.92 = 1.2786\, THz \tag{5.4.7}$$

The pulse width becomes:

$$\Delta t_{envelope} = \frac{1}{\Delta f_{envelope}} \tag{5.4.8}$$

$$\boldsymbol{\Delta t_{envelope} = 0.7821\, ps}$$

The inverse of the frequency of the comb spectrum envelope gives the pulse width of the device. Hence, the estimated **pulse width** is approximately $\boldsymbol{0.8\, ps}$**.**

Device Parameters	**Symbols**	**Units**	**Values**			
Operating Temperature	T	℃	20	25	30	35
Cavity Length	l	μm	1500			
Strip Width	w	μm	2.3			
Repetition Rate	Δf_{FSR}	GHz	≅ 28			
Cavity roundtrip time	τ	ps	35.7			
Pulse Width	$\Delta t_{envelope}$	ps	≅ 0.8			
Threshold current	I_{th}	mA	51	54	58	62
Slope of L-I curve	$\Delta P/\Delta I$	W/A	0.0924	0.0898	0.0886	0.0824
External Differential Quantum Efficiency	η_d	%	11.58	11.26	11.11	10.33

Table 6: Summary of device parameters

5.5 RF Measurements

Radio Frequency (RF) testing in semiconductor lasers is essential in determining characteristics such as the repetition rate and stability of the line spacing between consecutive longitudinal modes. These parameters are crucial for assessing the performance of the mode-locked laser. By conducting RF testing for various injection currents and thermal conditions, the laser's long-term performance can be analyzed.

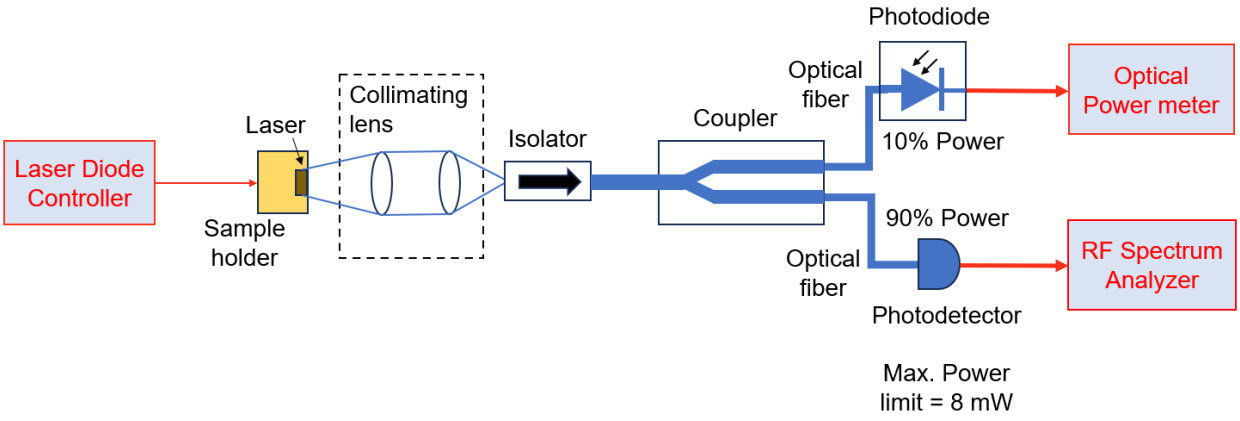

Figure 39: Block diagram representing measurement setup for RF test

For RF testing, measurements were taken at different injection currents while keeping the temperature constant at 25℃. The setup for measuring the RF spectrum consisted of a Keysight PXA N9030A Signal Analyzer with a maximum bandwidth of 50 GHz. Since the RF spectrum analyzer processes electrical signals in the frequency domain, the optical signals from the 90% split of the coupler was directed into a high-speed New Focus InGaAs photodetector. This photodetector has the maximum pulse power limit of 8 mW, requiring the optical power to remain below this threshold to prevent damage.

At lower bias currents, the optical power from the coupler remained within the safe limit for injection currents up to $200mA$. However, when the injection current exceeded 220 mA, the output power from the coupler surpassed the photodetector's power limit. In such cases, an attenuator was used to reduce the power level. After attenuation, the optical power was maintained at approximately 6.5 mW. The RF spectrum recorded at 25℃ is presented in Figure 40.

The test parameters for the Spectrum analyzers play a crucial role in determining the pulse linewidth values. These parameters include:

1) Span and Center
2) Reference level

3) Resolution Bandwidth (RBW)
4) Video Bandwidth (VBW)

The span and centre parameters determine the frequency range analyzed. In our measurements, the span was kept constant at $500 - 600\ MHz$, and the center frequency was set around $28\ GHz$ as the frequency displayed on the RF spectrum analyzer corresponds to the device's repetition rate explained in equation (5.4.4) of the previous section. The reference level is chosen such that the highest power peak of the device remains below the reference level set in the analyzer.

The RBW is one of the most critical parameters. It employs a Gaussian-shaped filter to distinguish closely spaced signals. Two narrowly spaced signals can be resolved only if the RBW value is smaller than the frequency separation between them. If the RBW is set too high, closely spaced signals will be mistaken as a single signal. Therefore, RBW values were adjusted for different injection currents to ensure accurate linewidth measurements. Notably, decreasing RBW also reduces the signal's noise floor.

In contrast, VBW influences only how the signal is displayed on the screen. Lowering VBW reduces the displayed noise on the trace. In our case, VBW was set to $100\ Hz$ to achieve clearer signal presentation.

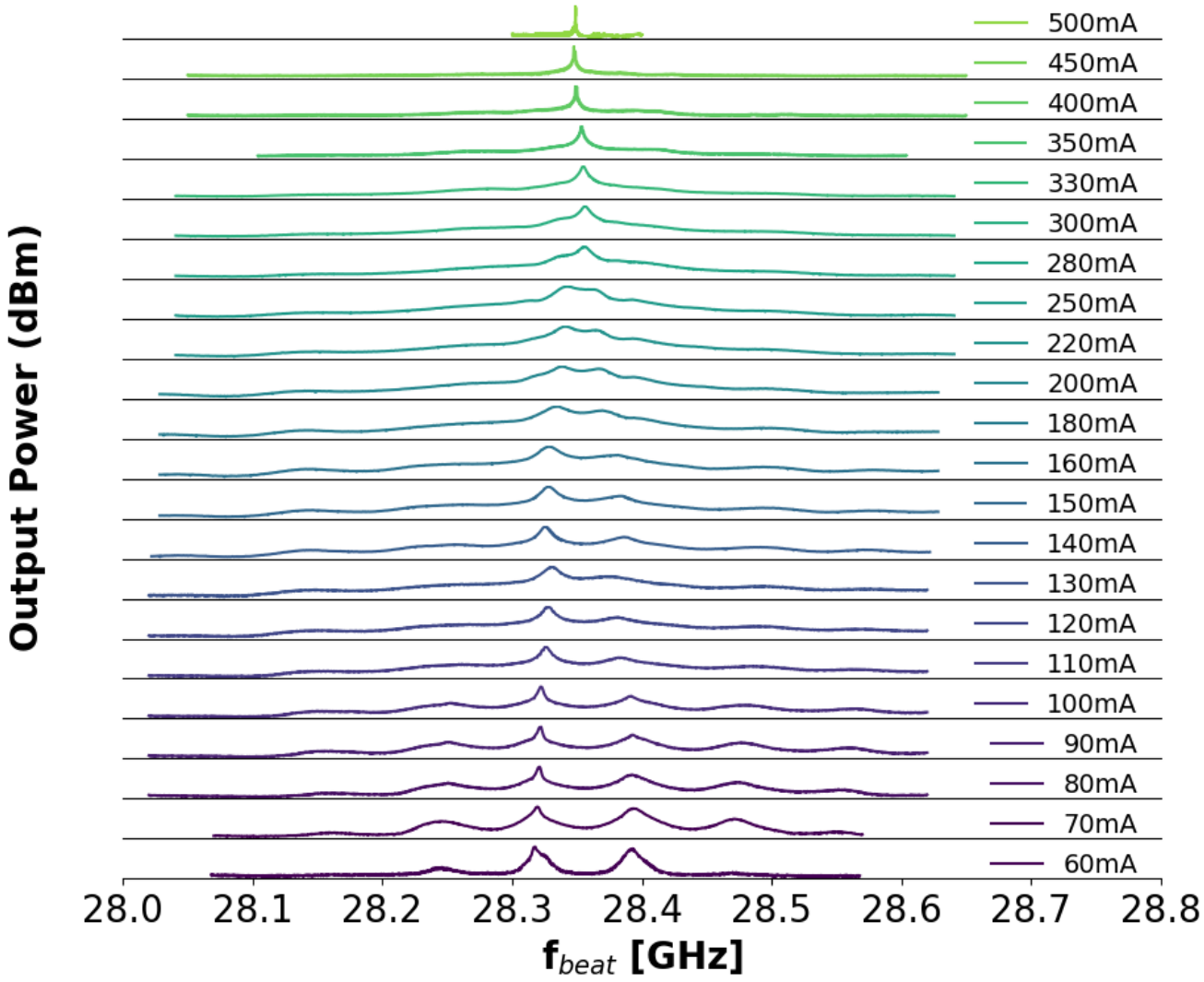

Figure 40: RF Spectrum at different injection currents at $T = 25$℃.

The results indicate that multiple side-modes appeared instead of a single, narrow linewidth. At lower injection currents, more side peaks are observed, progressively merging into a fundamental mode as the injection current increases. Additionally, the linewidth of the peak stabilizes at higher injection currents.

Interestingly, when the position of the collimating lens was slightly adjusted in the X, Y, and Z directions away from the laser device under test, the side modes or the multiple peaks disappeared at lower injection currents. This adjustment resulted in a smooth, narrow single linewidth, even at reduced injection currents. This phenomenon was further verified using other samples from the same wafer and a 3-layer Quantum Dash sample from a different wafer. One plausible explanation

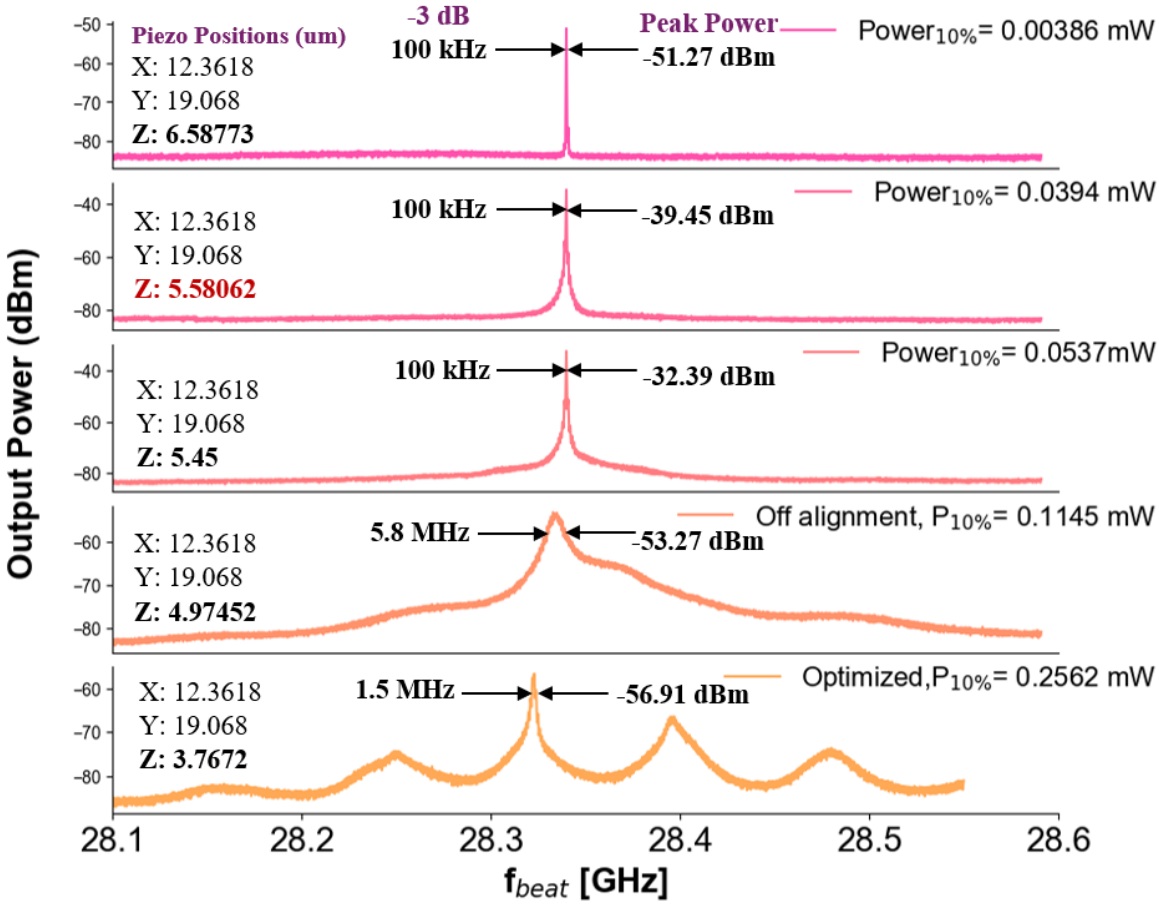

Figure 41: Results showing the changes observed in the mode-locking RF spectrum for I=90 mA and T=25°C as the lens position in the Z-direction is moved away from the sample.

for the existence of multiple peaks in the RF spectrum could be because 5-layer and 3-layer Quantum Dash laser devices are multimode lasers likely causing the side peaks in the RF spectrum.

Figure 41 illustrates the impact of the collimating lens on the mode-locked performance. The bottom-most RF spectrum represents the optimized lens position, where the lens collects the maximum number of photons. As the lens is gradually changed in the Z-position, the spectra from bottom to top depict the evolution of the RF spectrum. At a specific piezoelectric Z- position, a nearly ideal, narrow linewidth is achieved, even at a low injection current of 90 mA. Similar behaviour was observed at various injection currents and temperatures for different samples, reinforcing the reproducibility of this phenomenon.

Injection Currents (mA)	Resolution Bandwidth (kHz)	Video Bandwidth (Hz)	Centre Frequency (GHz)	Peak Power (dBm)	$-3\ dB$ Linewidth
60	820	510	28.318	−59.79	3.65 MHz
70	1000	300	28.32	−53.64	3 MHz
80	1000	510	28.32	−47.03	2 MHz
90	1000	510	28.3224	−43.8	1.5 MHz
100	1000	510	28.3218	−40.92	3 MHz
110	1000	510	28.3272	−42.78	5.9 MHz
120	1000	510	28.3272	−44.01	6 MHz
130	1000	510	28.3308	−43.54	8.4 MHz
140	300	100	28.3255	−46.93	5.8 MHz
150	300	100	28.3272	−47.59	9.2 MHz
160	300	100	28.3296	−48.93	13.2 MHz
180	300	100	28.3296	−50.46	24.5 MHz
200	300	100	28.3386	−51.38	17 MHz
220	300	100	28.3408	−48.48	13.5 MHz
250	300	100	28.3408	−48.31	29.2 MHz
280	300	100	28.3558	−47.15	8.1 MHz
300	300	100	28.3558	−43.98	4.9 MHz
330	300	100	28.3558	−40.77	3.6 MHz
350	300	100	28.3535	−36.96	700 kHz
400	51	100	28.3488	−34.7	300 kHz
450	51	100	28.3476	−31.77	100 kHz
500	51	51	28.3488	−22.25	20 kHz

Table 7: Summary of the linewidth values for various injection currents and spectrum analyzer settings.

The results presented in Table 7 highlight the different parameters of the OSA set to obtain the peak power values and corresponding linewidth values. From the results, it is evident that the linewidth values do not follow a specific trend. When the RF spectrum exhibits multiple peaks, i.e. at lower injection currents, the linewidth tends to become narrower. However, as the injection current increases and the multiple peaks begin to merge into a single peak, the linewidth broadens. At higher injection currents (above 250 mA), the linewidth becomes narrow again.

5.6 Dispersion Measurements

For the dispersion measurement, the experimental setup was identical to that used for OSA measurements, except for one change in equipment. Since the settings of the OSA play a crucial role in determining the dispersion values, the AQ6380 Yokogawa OSA was used for these measurements as it has a higher resolution of 0.005 nm, whereas the one used for OSA measurements has a maximum resolution of 0.05nm. A bar sample with the cavity length of 1693 μm and varying ridge widths (e.g., 2.0, 2.2, 2.4, 3.0, 3.2, 3.4 µm etc.) was analyzed. To ensure single transverse mode operation, the device with the smallest ridge width i.e. 2 μm, was selected. As a preliminary step, the L-I curves for the device were recorded to determine its threshold currents at various temperatures. The L-I curve data is presented in Figure 42.

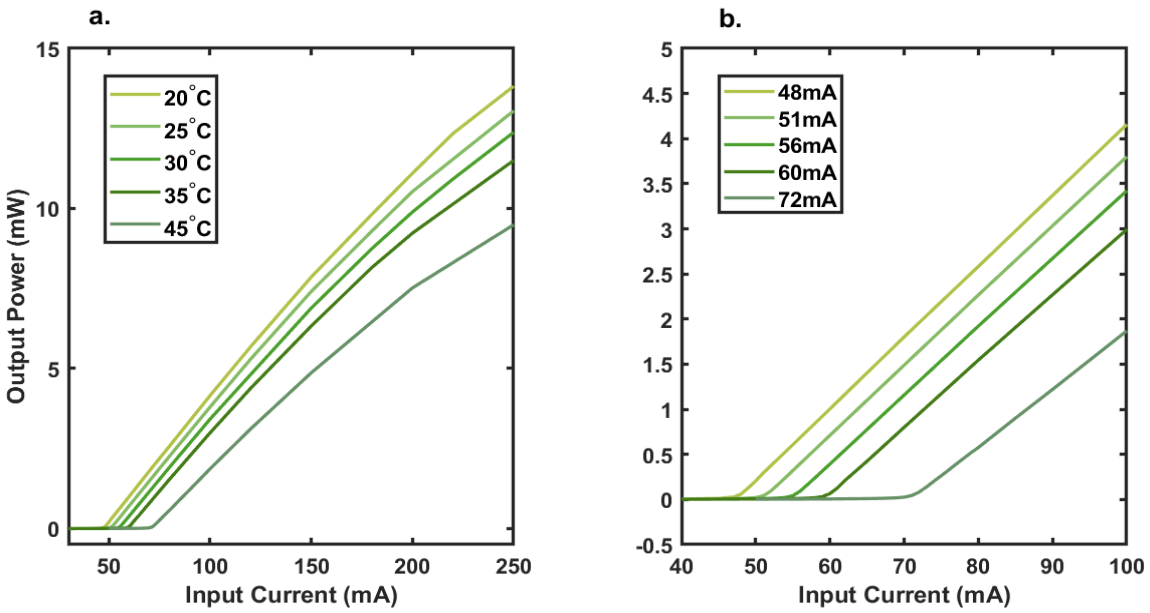

Figure 42: a) L-I curves measured for the bar sample at five temperatures.
b) The results highlight the threshold currents extracted for each temperature.

After recording the L-I curves, the dispersion tests involved recording the full spontaneous emission spectra. These spectra were obtained at different temperatures by setting the injection

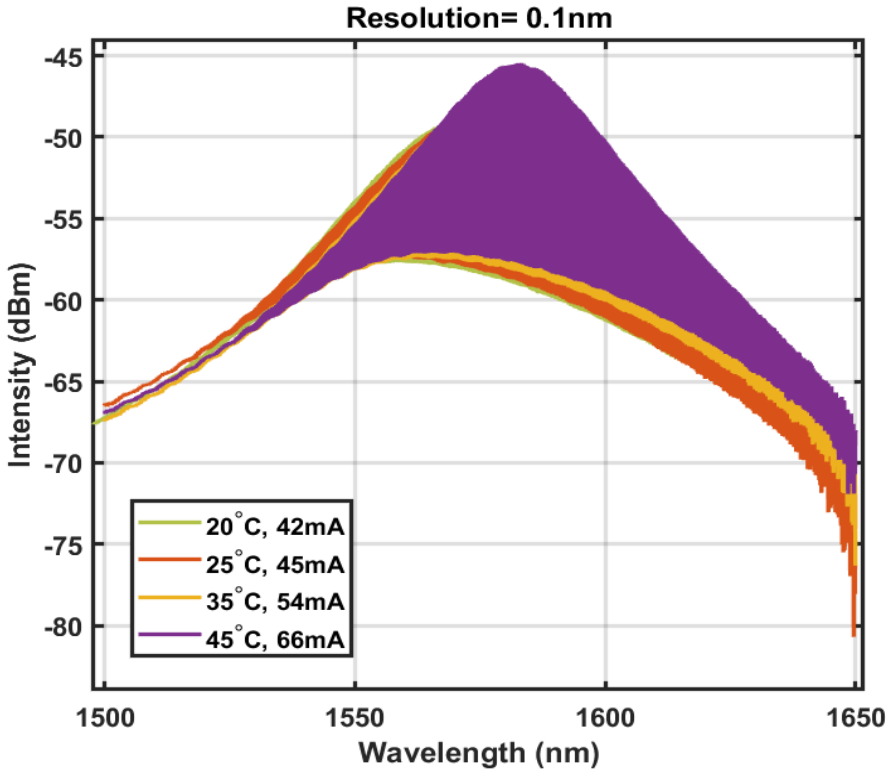

Figure 43: The resulting spectra illustrate the spontaneous emission spectra recorded at four temperatures (20–45℃) for injection currents set 5 mA below the threshold for each temperature.

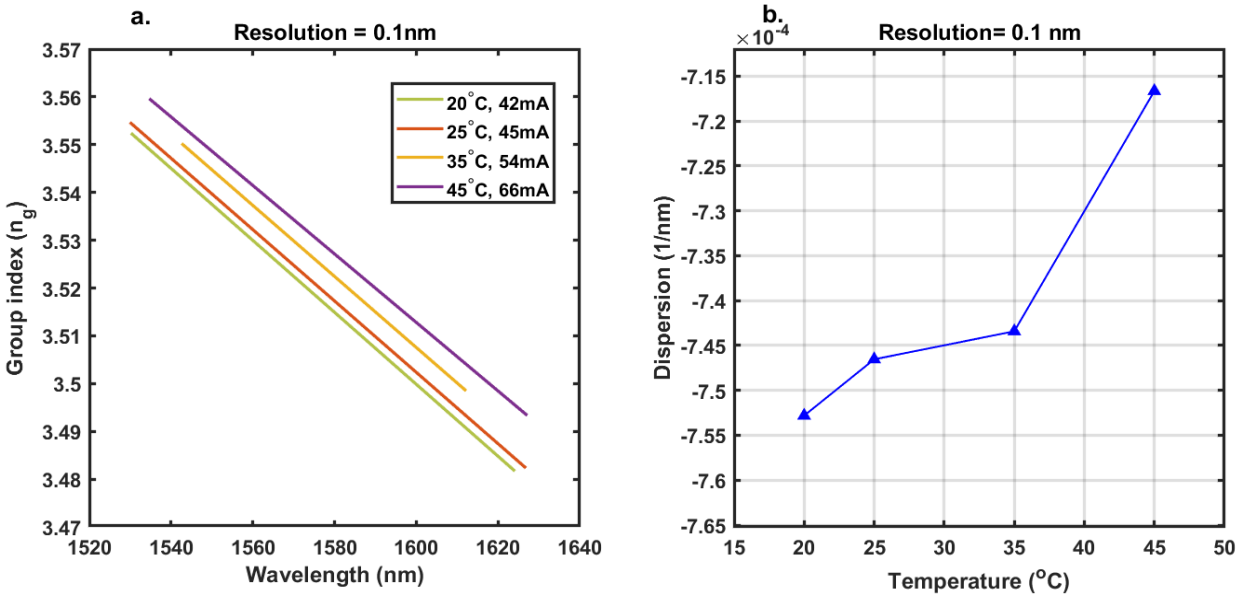

Figure 44: a) The variation of the group index with wavelength for different temperatures.
b) *The corresponding dispersion values for the same temperature range.*

current to 5 mA below the threshold current for each specified temperature. Lower injection currents were deliberately chosen to capture the spontaneous emission region, as the device has not yet begun producing mode-locked pulses. To avoid mode-locking within the laser, the dispersion was calculated from the spontaneous emission region of the laser device.

To calculate the dispersion within the cavity, the full spontaneous emission spectra recorded at various temperatures were fed into NRC's curve-fitting tool. This tool provided a linear relationship between the group index and wavelength. The slope of this fitted linear relationship was used to calculate dispersion values for each temperature.

The dispersion results, presented in Figure 44(b) and Table 8(b), demonstrate that dispersion inside the cavity increases with an increase in temperature.

a.

OSA Parameters	**Values**
Resolution	$0.1\ nm$
Sampling Points	1667.5 samples/ nm
Sensitivity	MID
Average	10

b.

Temperature (℃)	**Dispersion $(1/nm)$**
20	-7.5281×10^{-4}
25	-7.4654×10^{-4}
35	-7.4342×10^{-4}
45	-7.1667×10^{-4}

Table 8: a) Lists the OSA parameters settings used to record spontaneous emission spectra at different temperatures.
b) Summarizes the calculated dispersion values for each temperature based on the slope of the group index versus wavelength relationship. These numerical values correspond to the trends depicted in Figure 44 (b).

5.7 Results and Discussions

This chapter discussed the testing results of the QDash laser device. The key performance characteristics such as the threshold currents, optical spectra at various injection currents, RF test and dispersion results were investigated throughout the chapter and the results are summarised here:

L-I Characteristics:

The results for the L-I curves, depicted in Figure 33, highlights the threshold currents at different temperatures. The data depicts that with increase in temperature, the value of threshold current rises. It was observed that with every 5℃ increment in the temperature, the threshold current increases by approximately 4 mA. The maximum peak output power of the laser decreases with increasing temperature. Additionally, the output power as a function of injection current declines more rapidly at higher temperatures due to heating effects.

Optical Spectra:

The optical spectra recorded at 22℃ and 30℃ for various injection currents are summarized in the Table 5. The results indicate that both the peak power and the $-3dB$ spectral width increases with rise in injection current.

Another significant observation is the red shift (shift towards longer wavelength) in the spectrum with changes in operating conditions, such as the increase in injection current and temperature. For example, at $T = 30$℃, with the increase in injection current from 150 mA to 450 mA , the peak power wavelength shifts from 1549 nm to 1558 nm, accompanied by an increment of approximately 4 nm in the temporal or spectral width.

The red-shift observed in the spectra occurs due to changes in the refractive index of the material. As the injection current increases, the refractive index changes according to the Kramers-Kronig relation, leading to a shift in the emission wavelength towards longer wavelengths[62]. Another reason for this shift is the increase in temperature. Higher injection currents result in elevated temperatures, which, in turn, causes band-gap narrowing[63].

The summary of device parameters retrieved from the measurements is presented in Table 6, providing an overview of the key characteristic parameters of the laser device under test.

RF Results:

The results of the RF measurements, presented in Figure 40 and Table 7, highlight the RF spectrum for various injection currents at a fixed temperature of 25℃. The data reveals that for injection currents ranging from $60 - 100\ mA$, the RF spectrum shows multiple peaks. The $-3\ dB$ linewidth for these currents decreasing gradually from $3.65\ MHz$ to $3\ MHz$.

As the injection current increases beyond $100\ mA$ i.e., from $110 - 280\ mA$, the side-peaks begin to merge, forming a single dominant peak. During this transition, it was observed that the side-peaks disappear progressively, and the linewidth broadens as the multiple peaks consolidate into a single peak. For injection currents higher than $300\ mA$, the RF spectrum shows a single dominant mode with significantly enhanced stability. At these higher injection currents, the linewidth narrows further, reaching a minimum of $20\ kHz$ at $500\ mA$.

An intriguing phenomenon was observed when the collimating lens was adjusted in different directions. Specifically, the multiple peaks observed at the lower injection currents disappear upon lens adjustments. For instance, Figure 41 shows the changes in the RF spectrum recorded at an injection current of $90\ mA$. The bottom-most spectrum corresponds to the lens position capturing the maximum emitted power from the device. As the lens position was changed, a single, narrow and stable peak was achieved.

One possible explanation for this phenomenon is that with the adjustments in the lens position, the side-modes are suppressed due to alterations in the optical field distribution. Another reason could be that not all modes are captured when the lens is shifted. The third possibility could be the formation of external cavities within the setup.

However, none of these explanations could be conclusively confirmed due to time constraints and the lack of existing literature discussing this phenomenon. Far-field measurement tests could potentially confirm the first hypothesis, but as discussed, further exploration of this aspect was not feasible within the project timeline.

Dispersion Measurements:

Dispersion measurements were performed on a different sample than the previous device- a bar sample with a ridge width of $2\ \mu m$. The narrower ridge device was chosen to ensure that only a single mode could be sustained within the cavity. Initially, the L-I curves for five temperatures were recorded, as illustrated in Figure 42. Using the threshold current data from these measurements, the injection current was set to $5\ mA$ below the threshold for each temperature, and the spontaneous emission spectra were recorded as presented in Figure 43.

The line-spacing results retrieved from further analysis are summarized in Table 8. Part b) of Table 8, highlights the dispersion values for varying temperatures. The results indicate that dispersion

increases with an increase in temperature. For instance, the dispersion value at 20℃ is -7.53×10^{-4} (nm^{-1}), which increases to the value of -7.16×10^{-4} (nm^{-1}) at 45℃. This demonstrates the temperature dependence of dispersion in the laser cavity.

These findings enhance our understanding of the influence of temperature and injection current on the overall performance of the Quantum Dash devices and provide significant insights into the mode-locking mechanism. In the next chapter, the main findings, and the limitations of the current work, along with the potential areas for future explorations will be discussed.

CHAPTER 6
Conclusions and Future Scope

6.1 Limitations and Future Scope

There are numerous opportunities to extend the work presented in this thesis.

Simulation Work:

In the simulation part, the current work on Harold, PICWave, and Simulink platforms is limited to quantum well structures. This limitation arises from the inability of Harold and PICWave to model quantum dot and dash structures. As a result, we had fewer opportunities to compare the experimental results obtained from Quantum Dash samples with the simulation results. However, Photon Design is actively working on integrating more advanced structures, such as quantum dot structures, into their tools. Once these features become commercially available, a comparison between the experimental results and simulation outputs can be conducted.

The DDE model for quantum dots, discussed in Section 3.4 could also be extended to Simulink. Simulink offers a powerful time-domain analysis platform, enabling the exploration of various architectures and the simulation of complex dynamical processes in the time domain for a deeper understanding. The Simulink models currently implemented in this thesis use a Gaussian or bell-shaped passband filter. Future work could involve replacing this filter with alternative types, such as a sinc function or other filter functions, to investigate the changes in the laser dynamics.

Experimental Work:

For the experimental aspect, the RF measurements can be performed at higher temperatures to observe if the side modes at lower injection currents persist. During our study, we observed more side peaks at higher temperatures for the same value of injection currents. Additionally, a similar phenomenon—a smooth, narrow single peak—was observed when the position of the collimating lens was adjusted. A detailed investigation into this phenomenon could help determine whether the change in lens position alters the optical fields collected by the lens or an external cavity created within the setup causes this phenomenon. Far-field tests and other similar experiments can be conducted to explain these observations.

In the dispersion tests, there were some limitations. For instance, the injection current at which the spontaneous emission spectra were recorded was set $5\ mA$ below the threshold current. To ensure more accurate results, the injection currents should remain constant during dispersion measurements. However, this approach was not feasible as the spectral lines became weaker and noisier with increasing temperature when using the same injection current. We attempted to use an EDFA to boost the power of the modes or lines, but the amplification could not be achieved because the minimum required power for the EDFA to operate is $-25\ dBm$. In our case, the power of the peaks within the same spectral range and injection current was approximately $-70\ dBm$, which is too low for the optical amplifier to function. Furthermore, the amplifier caused the clamping of the lines, making them indistinguishable.

6.2 Conclusions

As the title of the thesis suggests, the work presented focuses on the study and analysis of numerical models which includes the Time-Domain Oscillator (TDO) model, Time-Domain Traveling Wave (TDTW) model, and Delay Differential Equation (DDE) model, implemented in Simulink. The numerical modelling section is specifically limited to passive mode-locked Quantum Well structures. The mathematical analysis of these models was performed on the foundational works by Trevor Hall et al. [32] for the TDO model, G. Agrawal et al. [27] for the TDTW model, and Vladimirov et al. [5], [27] for the DDE modelling of quantum well and quantum dot-based laser structures. Chapters 2 and 3 focus on the implementation of these models within Simulink.

Chapter 4 transitions into the simulation analysis of lasers. This section provides a detailed discussion of two simulation tools: Harold and PICWave, including their underlying physics and functionalities. A comparative analysis of gain models extracted from Harold and Crosslight and simulated into PICWave, was conducted by maintaining consistent simulation parameters across both tools. The results revealed some discrepancies in the material gain outputs. These

discrepancies were attributed to differences in the approaches used by the tools. Crosslight models more complex physical processes in greater detail, while Harold employs approximations to simplify these processes, offering a broader understanding of device characteristics. Both simulations were again limited to quantum well-based lasers due to the inability of Harold and PICWave to model QDot and QDash structures.

In the final segment, Chapter 5 presents the experimental results derived from various tests performed on Quantum Dash laser devices. These tests included the measurement of L-I curves and the observation of optical spectra changes under varying injection currents at different temperatures. The study led to several conclusions regarding the influence of these factors on device behaviour. Additionally, RF spectrum measurements were conducted at various injection currents while keeping the temperature fixed. These experiments revealed the impact of injection current and temperature on the mode-locking performance of quantum dash lasers. The phenomenon observed in Figure 41 was also confirmed in other 5-layer and 3-layer quantum dash laser samples, validating the presence of an intriguing phenomenon that requires further investigation. All the above-mentioned tests were performed on a 5-layer quantum dash laser device, and various characteristic parameters of the laser device were obtained during these experiments.

Finally, the dispersion measurements were carried out on a separate bar sample, in which a device with a minimum ridge width of 2 μm was selected to ensure the oscillation of a single transverse mode within the cavity. The dispersion tests revealed that dispersion increases with the temperature rise.

APPENDIX

I) Baseband equivalent transfer function of Bandpass filter

The convolution of a filter can be described as-

$$y = f \otimes x \tag{1}$$

Where f is the impulse response of the filter.

$$x(t) = u(t)e^{-i\omega_0 t} \tag{2}$$

$$y(t) = v(t)e^{-i\omega_0 t} \tag{3}$$

u, v are complex envelopes of x and y signals. ω_0 is the nominal carrier frequency.

All the information lies within the complex envelopes of the input and the output.

Taking the Fourier transforms of equations (1), (2) and (3)

$$Y(\omega) = F(\omega)\, X(\omega) \tag{4}$$

$$X(\omega + \omega_0) = U(\omega) \tag{5}$$

$$Y(\omega + \omega_0) = V(\omega) \tag{6}$$

$$V(\omega) = Y(\omega + \omega_0) = F(\omega + \omega_0)\, X(\omega + \omega_0) \tag{7}$$

$$V(\omega) = H(\omega)\, U(\omega) \tag{8}$$

where

$$H(\omega) = F(\omega + \omega_0) \tag{9}$$

The transfer function of two pole bandpass filter is given as:

$$F(\bar{\omega}) = \frac{1}{1 + jQ\left[\frac{\bar{\omega}}{\omega_0} - \frac{\omega_0}{\bar{\omega}}\right]} \tag{10}$$

Where $Q = \omega_0/\Delta\omega$ is the Quality factor, $\Delta\omega$ is the $-3\ dB$ bandwidth, and ω is the offset frequency from the nominal carrier frequency ω_0 which is the natural frequency of the resonator.

Substituting $\bar{\omega} = \omega + \omega_0$ in equation (10)

$$F(\omega + \omega_0) = \frac{1}{1 + jQ\left[\frac{\omega + \omega_0}{\omega_0} - \frac{\omega_0}{\omega + \omega_0}\right]}$$

$$H(\omega) = F(\omega + \omega_0) = \frac{1}{1 + jQ\left[1 + \frac{\omega}{\omega_0} - \frac{1}{\frac{\omega}{\omega_0} + 1}\right]} \tag{11}$$

The offset frequencies are of small magnitude $\left|\frac{\omega}{\omega_0}\right| \sim 10^{-6} - 10^{-4}$, by applying the binomial expansion to first order and ignoring the higher-order terms:

$$\frac{1}{1 + \frac{\omega}{\omega_0}} = 1 - \frac{\omega}{\omega_0} + \cdots \tag{12}$$

Equation (11) can be modified as:

$$H(\omega) = \frac{1}{1 + jQ\left[1 + \frac{\omega}{\omega_0} - 1 + \frac{\omega}{\omega_0}\right]}$$

$$H(\omega) = \frac{1}{1 + jQ\frac{2\omega}{\omega_0}} \tag{13}$$

The final expression becomes:

$$\boxed{H(\omega) = \frac{1}{1 + j\omega\tau_R}} \tag{14}$$

where $\tau_R = \frac{2Q}{\omega_0}$

The expression in equation (14) is the baseband equivalent transfer function of bandpass filter.

The transfer function can also be written as:

$$\frac{V(\omega)}{U(\omega)} = \frac{1}{1 + j\omega\tau_R}$$

$$V(\omega)(1 + j\omega\tau_R) = U(\omega)$$

$$j\omega\tau_R V(\omega) + V(\omega) = U(\omega) \tag{15}$$

In time domain, the above equation can be written as:

$$\tau_R \frac{\partial v(t)}{\partial t} + v(t) = u(t) \tag{16}$$

II) Dynamical Equation in case of flat-top passband for Band Pass Filter

The impulse response for a flat-top passband filter is given as:

$$H(\omega) = \frac{Y(\omega)}{X(\omega)} = 1 \tag{17}$$

In the time domain,

$$h(t) = \delta(t) \tag{18}$$

The dynamical equation for free-oscillating OEO is given as:

$$v = e^{i\phi} K(h \otimes (D_{\tau_D} v))$$

which for the impulse response for flat passband filter becomes:

$$v = e^{i\phi} K(\delta(t) \otimes (D_{\tau_D} v))$$

$$v = e^{i\phi} K(\delta(t - \tau_D) \otimes v) \tag{19}$$

By using the impulse property:

$$\delta(t - t_0) \otimes f(t) = f(t - t_0) \tag{20}$$

Applying the property in equation (19), the expression becomes:

$$v = e^{i\phi} K\, v(t - \tau_D) \tag{21}$$

This makes the expression reduced-phase model to look like:

$$\theta_v(t) = \phi + \theta_v(t - \tau_D); modulo\ 2\pi \tag{22}$$

$$\theta_v(t) - \theta_v(t - \tau_D) = \phi + 2\pi \tag{23}$$

It is assumed that the oscillator is in a single-mode oscillation state of frequency ω_p

$$\theta_v(t) = \omega_p t \tag{24}$$

$$\omega_p \tau = \phi + 2p\pi$$

BIBLIOGRAPHY

[1] F. Prati, A. M. Perego, S. Barland, and G. J. De Valcárcel, "Mode-locking of lasers," *Photoniques*, no. 122, pp. 70–75, 2023, doi: 10.1051/photon/202312270.

[2] S. V. Kartalopoulos, "ch-2 Optical Components," in *DWDM: Networks, Devices, and Technology*, New Jersey: Wiley-Interscience, 2003, pp. 93–234.

[3] A. Yadav, N. B. Chichkov, E. A. Avrutin, A. Gorodetsky, and E. U. Rafailov, "Edge emitting mode-locked quantum dot lasers," *Prog. Quantum Electron.*, vol. 87, p. 100451, Jan. 2023, doi: 10.1016/j.pquantelec.2022.100451.

[4] E. U. Rafailov, M. A. Cataluna, and W. Sibbett, "Mode-locked quantum-dot lasers," *Nat. Photonics*, vol. 1, no. 7, pp. 395–401, Jul. 2007, doi: 10.1038/nphoton.2007.120.

[5] E. A. Viktorov, P. Mandel, A. G. Vladimirov, and U. Bandelow, "Model for mode locking in quantum dot lasers," *Appl. Phys. Lett.*, vol. 88, no. 20, p. 201102, May 2006, doi: 10.1063/1.2203937.

[6] D. H. Hartman and Z. Ahmad, "Optical Clock Distribution Using a Mode-Locked Semiconductor Laser Diode System," *Light. Technol.*, vol. 9, no. 12, pp. 1646–1649, Dec. 1991, doi: 10.1109/50.108709.

[7] L. J. Mawst and N. Tansu, "5.15 Quantum-Well Lasers and Their Applications," in *Comprehensive Semiconductor Science and Technology*, vol. 5, USA: Elsevier, 2011, pp. 626–682.

[8] B. Shi *et al.*, "Comparison of static and dynamic characteristics of 1550 nm quantum dash and quantum well lasers," *Opt. Express*, vol. 28, no. 18, p. 26823, Aug. 2020, doi: 10.1364/OE.399188.

[9] P. M. Stolarz *et al.*, "Spectral Dynamical Behavior in Passively Mode-Locked Semiconductor Lasers," *IEEE Photonics J.*, vol. 3, no. 6, pp. 1067–1082, Dec. 2011, doi: 10.1109/JPHOT.2011.2172403.

[10] J. Xu *et al.*, “Passively Mode-Locked Quantum-Well Laser With a Saturable Absorber Having Gradually Varied Bandgap,” *IEEE Photonics Technol. Lett.*, vol. 29, no. 11, pp. 889–892, Jun. 2017, doi: 10.1109/LPT.2017.2693408.

[11] P. J. Poole, Z. Lu, J. Liu, P. Barrios, Y. Mao, and G. Liu, “A Performance Comparison Between Quantum Dash and Quantum Well Fabry-Pérot Lasers,” *IEEE J. Quantum Electron.*, vol. 57, no. 6, pp. 1–7, Dec. 2021, doi: 10.1109/JQE.2021.3107850.

[12] D. Bimberg, N. Kirstaedter, N. N. Ledentsov, Z. I. Alferov, P. S. Kop’ev, and V. M. Ustinov, “InGaAs–GaAs Quantum-Dot Lasers,” *IEEE J. Sel. Top. Quantum Electron.*, vol. 3, no. 2, pp. 196–205, Apr. 1997, doi: 10.1109/2944.605656.

[13] Victor M. Ustinov et al., “ch 2: Fabrication techniques and methods for semiconductor quantum dots,” in *Quantum Dot Lasers*, vol. 11, in Series on Semiconductor Science and Technology, vol. 11, Oxford University Press, 2003, pp. 45–61. [Online]. Available: 10.1093/acprof:oso/9780198526797.001.0001

[14] P. M. Petroff, “ch-1 Epitaxial Growth and Electronic Structure of Self-Assembled Quantum Dots,” in *Single Quantum Dots Fundamentals, Applications and New Concepts*, vol. 90, in Topics in Applied Physics, vol. 90, 2003, pp. 1–24. [Online]. Available: https://link.springer.com/book/10.1007/b13751

[15] A. Stintz, G. T. Liu, H. Li, L. F. Lester, and K. J. Malloy, “Low-threshold current density 1.3-μm InAs quantum-dot lasers with the dots-in-a-well (DWELL) structure,” *IEEE Photonics Technol. Lett.*, vol. 12, no. 6, pp. 591–593, Jun. 2000, doi: 10.1109/68.849053.

[16] K. H. Schmidt, G. Medeiros-Ribeiro, M. Oestreich, P. M. Petroff, and G. H. Döhler, “Carrier relaxation and electronic structure in InAs self-assembled quantum dots,” *Phys. Rev. B*, vol. 54, no. 16, pp. 11346–11353, Oct. 1996, doi: 10.1103/PhysRevB.54.11346.

[17] J. Siegert, “Carrier dynamics in semiconductor quantum dots,” Doctoral Thesis, Royal Institute of Technology, Stockholm, Sweden, 2006. [Online]. Available: https://www.diva-portal.org/smash/get/diva2:10412/FULLTEXT01.pdf

[18] Z. Qiao *et al.*, “Modal gain characteristics of a two-section InGaAs/GaAs double quantum well passively mode-locked laser with asymmetric waveguide,” *Sci. Rep.*, vol. 12, no. 1, p. 5010, Mar. 2022, doi: 10.1038/s41598-022-09136-6.

[19] J. Qin *et al.*, “10 GHz regeneratively mode-locked thulium fiber laser with a stabilized repetition rate,” *Opt. Express*, vol. 29, no. 23, p. 37695, Nov. 2021, doi: 10.1364/OE.435537.

[20] J. Qin *et al.*, “20 GHz actively mode-locked thulium fiber laser,” *Opt. Express*, vol. 26, no. 20, pp. 25769–25777, 2018, doi: 10.1364/OE.26.025769.

[21] W. Li, “Different methods to achieve hybrid mode locking,” *Cogent Phys.*, vol. 6, no. 1, p. 1707624, Jan. 2019, doi: 10.1080/23311940.2019.1707624.

[22] A. G. Vladimirov and D. V. Turaev, “A new model for a mode-locked semiconductor laser,” *Radiophys. Quantum Electron.*, vol. 47, no. 10–11, pp. 769–776, Oct. 2004, doi: 10.1007/s11141-005-0015-8.

[23] Herman A. Haus, “Mode-locking of Lasers,” *IEEE J. Quantum Electron.*, vol. 6, no. 6, pp. 1173–1185, Dec. 2000, doi: 10.1109/2944.902165.

[24] G. New, “Pulse evolution in mode-locked quasi-continuous lasers,” *IEEE J. Quantum Electron.*, vol. 10, no. 2, pp. 115–124, Feb. 1974, doi: 10.1109/JQE.1974.1145781.

[25] H. A. Haus, “Theory of mode locking with a fast saturable absorber,” *J. Appl. Phys.*, vol. 46, no. 7, pp. 3049–3058, Jul. 1975, doi: 10.1063/1.321997.

[26] H. Haus, “Theory of mode locking with a slow saturable absorber,” *IEEE J. Quantum Electron.*, vol. 11, no. 9, pp. 736–746, Sep. 1975, doi: 10.1109/JQE.1975.1068922.

[27] G. P. Agrawal and N. A. Olsson, “Self-phase modulation and spectral broadening of optical pulses in semiconductor laser amplifiers,” *IEEE J. Quantum Electron.*, vol. 25, no. 11, pp. 2297–2306, Nov. 1989, doi: 10.1109/3.42059.

[28] G. P. Agrawal, “Effect of gain dispersion on ultrashort pulse amplification in semiconductor laser amplifiers,” *IEEE J. Quantum Electron.*, vol. 27, no. 6, pp. 1843–1849, Jun. 1991, doi: 10.1109/3.90014.

[29] R. G. M. P. Koumans and R. Van Roijen, “Theory for passive mode-locking in semiconductor laser structures including the effects of self-phase modulation, dispersion, and pulse collisions,” *IEEE J. Quantum Electron.*, vol. 32, no. 3, pp. 478–492, Mar. 1996, doi: 10.1109/3.485400.

[30] M. Rossetti, P. Bardella, and I. Montrosset, “Time-Domain Travelling-Wave Model for Quantum Dot Passively Mode-Locked Lasers,” *IEEE J. Quantum Electron.*, vol. 47, no. 2, pp. 139–150, Feb. 2011, doi: 10.1109/JQE.2010.2055550.

[31] M. Hasan, A. Banerjee, and T. J. Hall, “Injection Locking of Optoelectronic Oscillators With Large Delay,” *J. Light. Technol.*, vol. 40, no. 9, pp. 2754–2762, May 2022, doi: 10.1109/JLT.2022.3148480.

[32] A. Banerjee and T. J. Hall, “Simulation of optoelectronic oscillator injection locking, pulling & spiking phenomena,” *Sci. Rep.*, vol. 14, no. 1, p. 4332, Feb. 2024, doi: 10.1038/s41598-024-54777-4.

[33] Z. Liu and R. Slavik, “Optical Injection Locking: From Principle to Applications,” *J. Light. Technol.*, vol. 38, no. 1, pp. 43–59, Jan. 2020, doi: 10.1109/JLT.2019.2945718.

[34] E. Rubiola, “ch-3 Heuristic Approach to the Leeson Effect,” in *Phase Noise and Frequency Stability in Oscillators*, 1st ed., in The Cambridge RF and Microwave Engineering Series, Cambridge University Press, 2008, pp. 67–87. doi: 10.1017/CBO9780511812798.

[35] E. Rubiola, “ch-1 Phase noise and frequency stability,” in *Phase Noise and Frequency Stability in Oscillators*, 1st ed., Cambridge University Press, 2008, pp. 1–34. doi: 10.1017/CBO9780511812798.

[36] N. J. Kasdin, “Discrete Simulation of Colored Noise and Stochastic Processes and llf' Power Law Noise Generation,” *Proc. IEEE*, vol. 83, no. 5, pp. 802–827, May 1995, doi: 10.1109/5.381848.

[37] E. A. Avrutin and E. U. Rafailov, “Advances in Mode-Locked Semiconductor Lasers,” in *Semiconductors and Semimetals*, vol. 86, Elsevier, 2012, pp. 93–147. doi: 10.1016/B978-0-12-391066-0.00003-4.

[38] G. P. Agrawal and N. K. Dutta, “ch-2 Basic Concepts,” in *Semiconductor Lasers*, Second Edition., Boston, MA: Springer US, 1993, pp. 26–73. doi: 10.1007/978-1-4613-0481-4.

[39] C. Henry, “Theory of the linewidth of semiconductor lasers,” *IEEE J. Quantum Electron.*, vol. 18, no. 2, pp. 259–264, Feb. 1982, doi: 10.1109/JQE.1982.1071522.

[40] G. P. Agrawal, “ch 3: Optical Transmitters,” in *Fiber-optic communication systems*, 3. ed., in Wiley series in microwave and optical engineering. , New York, NY: Wiley-Interscience, 2002, pp. 77–132.

[41] J. Piprek, Ed., “Mode-Locked Semiconductor Lasers,” in *Handbook of optoelectronic device modeling & simulation. Volume one: Fundamentals, materials, nanostructures, LEDs, and amplifiers*, First issued in paperback., vol. II, 2 vols., in Series in optics and optoelectronics, vol. II., Boca Raton London New York: CRC Press, Taylor & Francis Group, 2019, pp. 183–233.

[42] L. Jaurigue, “Passively Mode-Locked Semiconductor Lasers,” Springer International Publishing, Cham, 2017. doi: 10.1007/978-3-319-58874-2.

[43] M. L. Davenport, M. A. Tran, T. Komljenovic, and J. E. Bowers, “ch-3 Mode-Locking Lasers,” in *Semiconductors and Semimetals*, vol. 99, Elsevier, 2018, pp. 171–184. doi: 10.1016/bs.semsem.2018.07.001.

[44] S. Droste, G. Ycas, B. R. Washburn, I. Coddington, and N. R. Newbury, “Optical Frequency Comb Generation based on Erbium Fiber Lasers,” *Nanophotonics*, vol. 5, no. 2, pp. 196–213, Jun. 2016, doi: 10.1515/nanoph-2016-0019.

[45] Y. Su *et al.*, “A novel generation scheme of ultra-short pulse trains with multiple wavelengths,” *Opt. Commun.*, vol. 389, pp. 176–180, Apr. 2017, doi: 10.1016/j.optcom.2016.12.044.

[46] S. Boscolo, C. Finot, and S. K. Turitsyn, “Bandwidth Programmable Optical Nyquist Pulse Generation in Passively Mode-Locked Fiber Laser,” *IEEE Photonics J.*, vol. 7, no. 5, pp. 1–9, Oct. 2015, doi: 10.1109/JPHOT.2015.2475177.

[47] V. Vujicic *et al.*, “Quantum Dash Mode-Locked Lasers for Data Centre Applications,” *IEEE J. Sel. Top. Quantum Electron.*, vol. 21, no. 6, pp. 53–60, Nov. 2015, doi: 10.1109/JSTQE.2015.2487884.

[48] L. St, “PICWave v6.1 Manual.” Photon Design.

[49] L. Jaurigue, *Passively Mode-Locked Semiconductor Lasers*. in Springer Theses. Cham: Springer International Publishing, 2017. doi: 10.1007/978-3-319-58874-2.

[50] E. A. Viktorov, P. Mandel, and G. Huyet, “Long-cavity quantum dot laser,” *Opt. Lett.*, vol. 32, no. 10, p. 1268, May 2007, doi: 10.1364/OL.32.001268.

[51] A. Fiore, A. Markus, and M. Rossetti, “Carrier dynamics in quantum dot lasers (Invited Paper),” presented at the Microtechnologies for the New Millennium 2005, G. Badenes, D. Abbott, and A. Serpenguzel, Eds., Sevilla, Spain, Jul. 2005, p. 464. doi: 10.1117/12.608478.

[52] J. Piprek, J. K. White, and A. J. SpringThorpe, “What limits the maximum output power of long-wavelength AlGaInAs/InP laser diodes?,” *IEEE J. Quantum Electron.*, vol. 38, no. 9, pp. 1253–1259, Sep. 2002, doi: 10.1109/JQE.2002.802441.

[53] Shun Lien Chuang, “ch 2: Basic Semiconductor Electronics,” in *Physics of Photonic Devices*, Second., USA: Wiley, 2012, pp. 27–76.

[54] L. St, “Harold v7.0 user manual.” Photon Design.

[55] Shun Lien Chuang, “ch 4: Theory of Electronic Band Structures in Semiconductors,” in *Physics of Photonic Devices*, Second., USA: Wiley, 2012, pp. 113–178.

[56] “Crosslight Device Simulation Software Manual.” Crosslight.

[57] Shoumin Liu, “Thermoelectric Cooler Control Using the DS4830 Optical Microcontroller.” Maxim Integrated, Aug. 17, 2012. [Online]. Available: https://www.analog.com/media/en/technical-documentation/app-notes/thermoelectric-cooler-control-using-the-ds4830-optical-microcontroller.pdf

[58] “User’s Guide: Laser Diode Controller LDC-3700C Series.” ILX Lightwave, Apr. 2009. [Online].Available: https://www.newport.com/medias/sys_master/images/images/h0b/hfa/8797190848542/LDC-37x4C-User-Manual.pdf

[59] “Brochure- NanoMax300-TS x-y-z parallel flexure stage.” Melles Griot, 2002. [Online]. Available: https://kik.creol.ucf.edu/documents/17max300specs.pdf

[60] “Operation Manual: Optical Energy and Power Meter.” Thorlabs, Germany, Mar. 2023. [Online]. Available: https://www.thorlabs.com/drawings/ae26ff0332edefd7-290F764F-9F1F-D912-83E8E2CF18471F4B/PM100D-Manual.pdf

[61] K. S. Mobarhan, “Test and Characterization of Laser Diodes: Determination of Principal Parameters.” Newport Corporation.

[62] C. Wang, K. Schires, M. Osiński, P. J. Poole, and F. Grillot, “Thermally insensitive determination of the linewidth broadening factor in nanostructured semiconductor lasers using optical injection locking,” *Sci. Rep.*, vol. 6, no. 1, p. 27825, Jun. 2016, doi: 10.1038/srep27825.

[63] J. E. Nkanta, “Modelling and Characterization of Laterally-Coupled Distributed Feedback Laser and Semiconductor Optical Amplifier,” University of Ottawa, Canada, 2016.